TOWARDS PREVENTION AND EARLY DIAGNOSIS OF SKIN CANCER:

COMPUTER-AIDED ANALYSIS OF DERMOSCOPY IMAGES

by

Maryam Sadeghi

B.Sc, Iran University of Science and Technology, Iran, 2006

A THESIS SUBMITTED IN PARTIAL FULFILLMENT
OF THE REQUIREMENTS FOR THE DEGREE OF

Doctor of Philosophy

in the
School of Computing Science
Faculty of Applied Sciences

SIMON FRASER UNIVERSITY
Summer 2012

APPROVAL

Name: Maryam Sadeghi

Degree: Doctor of Philosophy

Title of Thesis: Towards Prevention and Early Diagnosis of Skin Cancer: Computer-aided Analysis of Dermoscopy Images

Examining Committee:

Dr. Ze-Nian Li
Chair

Dr. M. Stella Atkins,Senior Supervisor, SFU

Dr. Tim K. Lee, Co-Supervisor,
Adjunct Professor, Computing Science, SFU,
Assistant Professor, Derm. and Skin Science, UBC

Dr. David McLean, Supervisor, Derm. and Skin Sci., UBC

Dr. Harvey Lui, Supervisor, Derm. and Skin Sci., UBC

Dr. Mark S. Drew, Internal Examiner

Dr. Emre Celebi, External Examiner,
Associate Professor, Computer Science,
Louisiana State University

Date Approved: July 3, 2012

Partial Copyright Licence

Abstract

Melanoma, the deadliest form of skin cancer, must be diagnosed early for effective treatment. Irregular pigment network and streaks are important clues for melanoma diagnosis using dermoscopy images. This thesis describes novel image processing approaches for computer-aided pigment network and streaks detection on dermoscopy images. Our methods provide meaningful visualization of these structures, and extract features for irregularity detection. Additionally we present our efforts towards prevention of melanoma, by developing a smartphone app, UV-Canada, to raise awareness of the importance of using sunscreen to prevent melanoma.

To locate pigment networks, after preprocessing steps, which include segmenting the lesion from the normal skin in the dermoscopy image, we use a graph-based approach to extract the holes and meshes of the pigment network, where cyclic subgraphs correspond to skin texture structures. Each correctly extracted subgraph has a node corresponding to a hole in the pigment network, and the image is classified according to the density ratio of the graph. Our results over a set of 500 dermoscopy images show an accuracy of 94.3% on classification of the images as pigment network Present or Absent. For analyzing the irregularity of the structure, we locate the network lines and define features inspired by the clinical definition to classify the network with an accuracy of 82% discriminating between Absent, Typical or Atypical, which is important for melanoma diagnosis.

To find streaks in dermoscopy images, filters are applied, and in a similar fashion to fingerprint analysis, orientation estimation and correction is performed to detect low contrast and fuzzy streak lines. A graph representation is used to analyze the geometric pattern of valid streaks, to model their distribution and coverage. We achieved an accuracy of 77% for classifying dermoscopy images into streaks Absent, Regular, or Irregular on 945 images; the largest validation dataset published to date.

Our contributions will improve automated diagnosis of melanoma using dermoscopy images.

Keywords: Computer Aided Diagnosis (CAD); Dermoscopy; Melanoma; Pigment Network; Streaks; Skin Cancer Prevention.

To my adorable husband, Majid
for all his love, support, patience, and encouragement!

Acknowledgments

I would like to express my deepest gratitude to my senior supervisor Stella Atkins. She patiently guided me through the course of my study program. Without her help, encouragement and enthusiasm, this thesis and research would not been possible. I also thank my supervisors Dr. Tim K. Lee, Dr. Harvey Lui, and Dr. David McLean for guiding me, sharing their knowledge and giving me valuable feedback. I will never forget your encouragements and continuous support during my skin cancer research and training.

Also my appreciation and my sincere thanks go to my parents, sisters, and brother, for being all the way with me. I owe them everything.

I would also like to thank all the fellow members of the Medical Imaging Analysis Lab at SFU, and my friends in Computing Science program at SFU, Skin Care Center and UBC Dermatology. Their friendship made my work and study environment enjoyable.

I also acknowledge the Skin Research and Training Center for providing funding and support for my training in the past two years.

Finally, special thanks are reserved for Majid Razmara, my husband, for his infinite love, support, kindness and help. His mental support made this journey possible and his technical help and support built a strong foundation for my research program. I could have never done this without him.

Contents

List of Tables

List of Figures

Chapter 1

Introduction

Skin cancer is the most common form of human cancer if melanoma, basal and squamous cell skin cancers are included. The annual rates of all forms of skin cancer are increasing each year, representing a growing public concern. Based on the *Cancer Trends Progress Report* by National Institute of Health of United States (NIH) [80], it is estimated that nearly half of all Americans who live to age 65 will develop skin cancer at least once [58]. Malignant melanoma, the most deadly form of skin cancer, is one of the most rapidly increasing cancers in the world. Melanoma is now the 7th most frequent cancer in Canada [58, 1] affecting 5,300 people in 2010 and causing 920 deaths [1] and the 5th most common malignancy in the United States [58]. 10710 deaths out of 21,700 incidences are estimated numbers in the United States during 2012 [99]. Metastatic melanoma is very difficult to treat, so the best treatment is still early diagnosis and prompt surgical excision of the primary cancer so that it can be completely excised while it is still localized. Therefore, advances in computer-aided diagnostic methods can aid self-examining approaches based on digital images, and may significantly reduce the mortality. This thesis investigates and reviews important aspects of automated analysis of skin lesions using digital dermoscopy images and proposes a novel approach for automated detection of the two important dermoscopy structures: pigment network and streaks.

1.1 Problem Definition and Motivation

As mentioned in the previous section, melanoma is now the 7th most frequent cancer in Canada. Over the past 31 years, more people have had skin cancer than all other cancers combined [1]. In addition, unlike many cancers, melanoma is clearly visible on the skin and up to 70% of all melanomas are first identified by the patients themselves (53%) or close family members (17%) [63].

Therefore, advances in computer-aided diagnostic methods can aid self-examination approaches and reduce the mortality significantly.

Dermoscopy, a non-invasive skin imaging techniques, has become a principal tool in the diagnosis of melanoma and other pigmented skin lesions. It involves optical magnification of the region-of-interest, which makes subsurface structures more visible than conventional macroscopic images. However, it has also been demonstrated that dermoscopy may actually lower the diagnostic accuracy in the hands of inexperienced dermatologists [103]. Therefore, computerized image understanding tools are needed to minimize the diagnostic errors. These errors are generally caused by the complexity of the subsurface structures and the subjectivity of visual interpretations [22, 36].

In almost all of the clinical dermoscopy methods, dermatologists look for the presence of specific visual features for making a diagnosis. Then, these features are analyzed for irregularities and malignancy [85, 105, 74, 61, 11].

To simulate an expert's diagnostic approach, an automated analysis of dermoscopy images requires several steps. Delineation of the region of interest, which has been widely addressed in the literature, is always the first essential step in a computerized analysis of skin lesion images [22, 110]. The border characteristics provide essential information for an accurate diagnosis [23]. For instance, asymmetry, border irregularity, and abrupt border cutoff are some of the critical features calculated based on the lesion border [66]. Furthermore, the extraction of other critical clinical indicators and dermoscopy structures such as atypical pigment networks, globules, and blue-white areas depend on the border detection. The next essential step is the detection and analysis of the key diagnostic features of the dermoscopic structures. Automatic detection and analysis of the key diagnostic features of the some of these dermoscopic structures has been recently addressed in the literature [96, 106, 36, 34, 8, 17, 31, 98] and will be reviewed in the following chapters.

The problem addressed in this thesis is how to analyze a given digital dermoscopic image for detecting pigment networks and streaks, and quantifying the irregularity of these structures, for use in diagnosing cancerous lesions especially melanoma. Images discussed in this thesis are a combination of images by oil immersion (non-polarised) dermoscopy and cross-polarized imaging.

1.2 Organization of the thesis

The rest of this thesis is organized as follows: Chapter 2 begins with a brief overview of the biology of skin and pigmented skin lesions, and formally introduces the dermoscopy technique and the common clinical skin cancer diagnostic methods. This chapter also investigates the important features

and characteristics of the deadliest skin cancer (melanoma), that can be detected by dermoscopy. This chapter also briefly reviews the current commercial systems available for the computer-aided diagnosis of melanoma. Chapter 3 reviews the previous work in automated melanoma diagnosis, and surveys the common steps used in an automatic skin lesion analysis system. These steps include image acquisition, pre-processing (image enhancement and skin lesion segmentation), and detection of dermoscopy structures, with a special focus on pigment networks and streaks, which are crucial for diagnosing melanoma.

My contributions to the field of computer-aided diagnosis of skin cancer start in Chapter 4, which briefly describes our approach to segment lesions from the normal skin. Then Chapters 5 and 6 describe my methods to detect and analyze two important dermoscopy features: pigment networks and streaks respectively. My work towards skin cancer prevention by public education is described in Chapter 7, and Chapter 8 concludes the thesis and summarizes my contribution.

Chapter 2

Background

2.1 Skin Biology and Pigmented Skin Lesions

2.1.1 Human Skin Biology

The skin is the human body's largest organ. It covers the entire body and its thickness varies from 0.5mm on eyelids to 4mm or more on the palms of hands and the soles of feet [42]. The skin is our first line of defense. Its primary roles are to protect the body and to maintain the integrity of internal systems. Its other functions are insulation, temperature regulation, sensation, and the production of vitamin D [42]. Technically, the skin consists of the three layers shown in Figure 2.1: the epidermis or top layer, the dermis or middle layer and the hypodermis or bottom layer [42].

Epidermis

The outer surface of the skin is called epidermis. The outer layer of the epidermis is comprised of hard, flattened dead cells. The epidermis mainly consists of keratinocytes. The epidermis also contains melanocytes, cells which are responsible for the skin's pigmentation, that provides natural protection against the sun's rays and Langerhans cells which are part of the immune system. The epidermis is composed of 4 or 5 layers depending on the region of skin being considered: the outermost layer being stratum corneum and then follows stratum lucidum, stratum granulosum, stratum spinosum and stratum basal illustrated in Figure 2.2. It is the most visible region under both dermoscopy and naked-eye examination and it is the origin of melanoma [42].

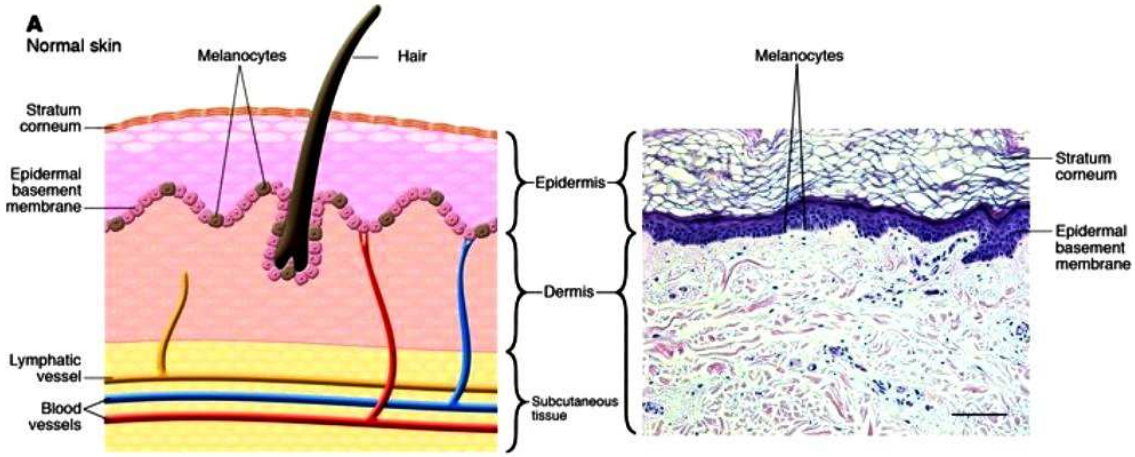

(a)

Figure 2.1: Skin structure: epidermis, dermis and hypodermis layers are shown [26].

Dermis

Below the epidermis is the dermis which is a thick, supple and sturdy layer of connective tissue. The dermis a dense meshwork of collagen and elastin fibers, two connecting proteins which supports tiny lymph and blood vessels. It allows the skin as well as the nerves, muscle cells, sweat and sebaceous glands, and hair follicles to breathe and be nourished. This layer contains the special cells that repair the skin, such as the fibroblasts that synthesize the skin proteins like collagen and elastin. The dermis is divided into the papillary dermis, and the reticular dermis [42].

Hypodermis

The hypodermis is the deepest layer of the skin, composed primarily of fat. It manages the skin's functions of feeding, excreting and heat exchange. The key cells are fat cells that provide energy, serve as a heat insulator for the body, and act as a shock absorber to protect underlying tissue against mechanical trauma and helps give our skin its resilience. Sweat glands originate in this layer and control the body's temperature by evaporating and cooling the skin surface [42].

Melanocytes

Melanocytes are the pigment producing cells in the skin. They are evenly distributed in the skin along the basal layer at the dermo-epidermal junction. Melanocytes produce melanosomes which

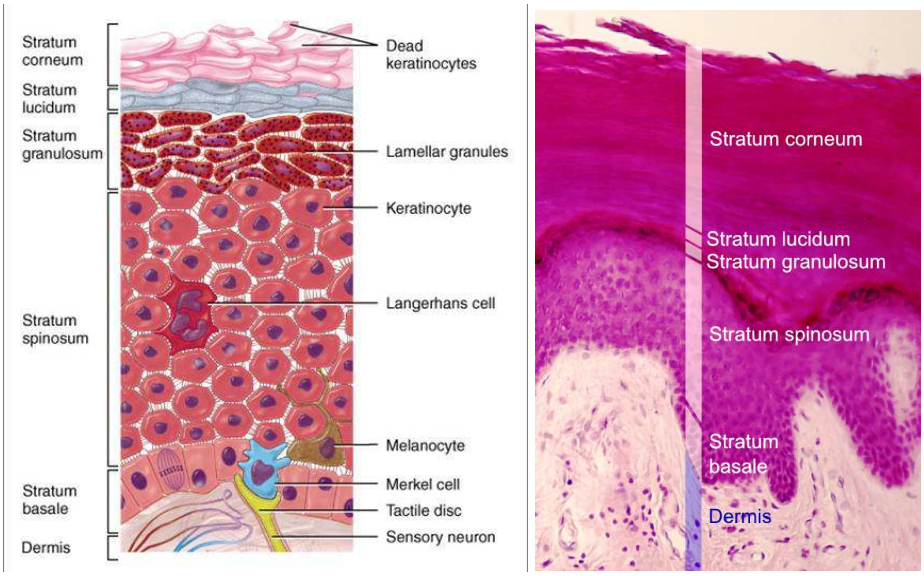

(a) (b)

Figure 2.2: Structures of the epidermis layer are shown on the schematic (a) and histology (b) images: the outermost layer is stratum corneum and then follows stratum lucidum, stratum granulosum, stratum spinosum and stratum basal [3].

can be transferred to the surrounding keratinocytes. Melanin is the major pigmentation factor for our skin colour due to the variation in number, size and distribution of melanosomes which will be increased if stimulated by UV-radiation or hormones [42].

2.1.2 Benign Pigmented Skin Lesions

The purpose of this section is not to give a complete overview of all types of pigmented skin lesions, but to provide a short presentation of the most common lesions. The following sub-sections will briefly review the benign and cancerous skin lesions.

Benign melanocytic lesions

Freckles and lentigo Freckles and lentigines are two benign pigmented lesions that can arise in the skin. In freckles, there is a temporary overproduction of melanin in skin due to exposure to

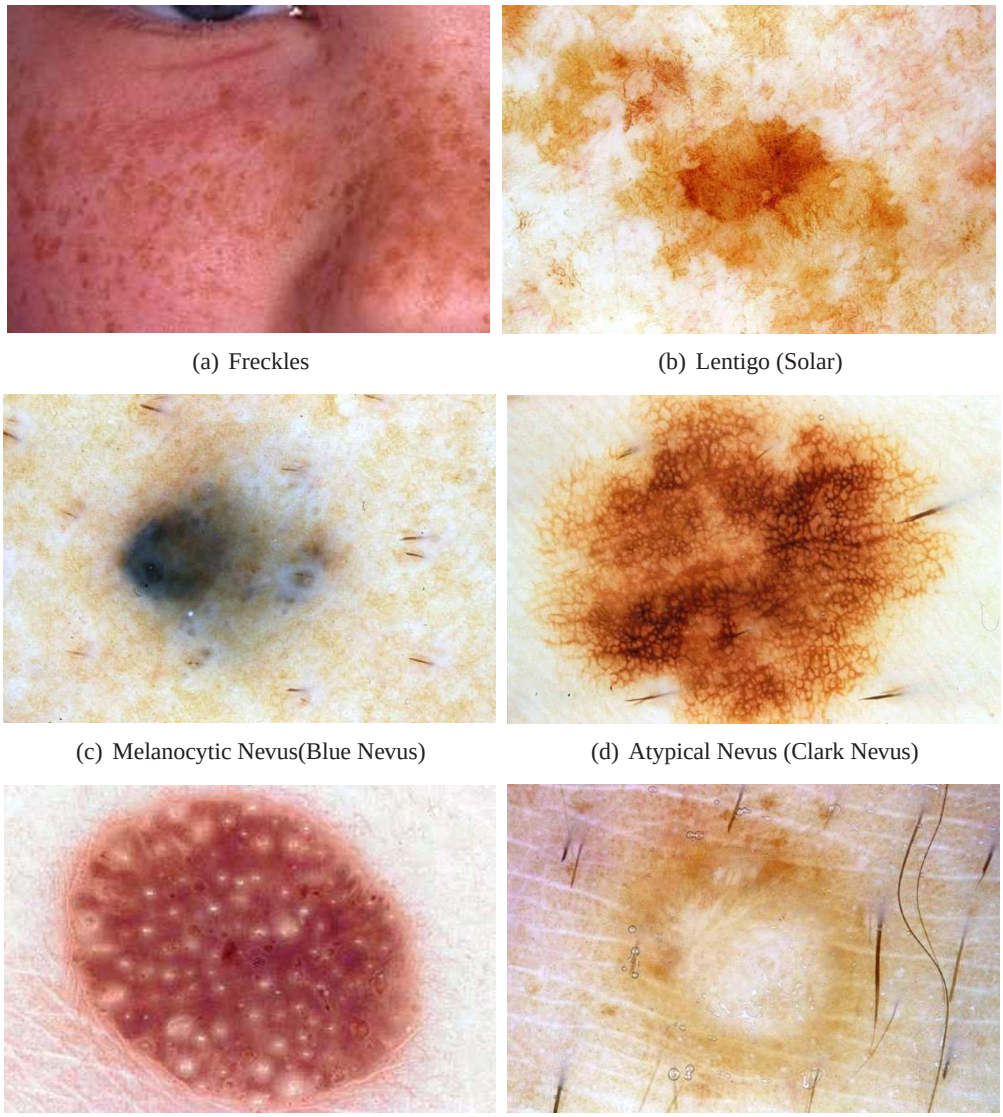

(a) Freckles (b) Lentigo (Solar)

(c) Melanocytic Nevus(Blue Nevus) (d) Atypical Nevus (Clark Nevus)

(e) Seborrhoeic Keratosis (f) Dermatofibroma

Figure 2.3: Examples of benign melanocytic and non-melanocytic lesions. *a*, *b*, *c* and *d* show examples of benign melanocytic lesions. *e* and *f* illustrate two types of benign non-melanocytic lesions. Images are taken with permission from [10, 82] (*a* is a digital RGB image while *b*-*f* are dermoscopic images).

UV-radiation, while in lentigo maligna there are an increased number of melanocytes in the dermo-epidermal junction. Figures 2.3-a and 2.3-b show examples of freckles and a lentigo lesion respectively [82].

Melanocytic nevi Nevi are lesions which are the result of proliferation of melanocytes at the dermo-epidermal junction. These clusters of melanocytes can either stay at this position or migrate into the dermis where they will be destroyed and disappear. There are variants of nevi with different growth patterns; junctional, compound, dermal, Spitz, Reed, blue nevi and more. The melanocytic nevi are categorized by their location in the skin (junctional nevi locate at the dermo-epidermal junction, compound nevi locate at both the dermo-epidermal junction and the dermis, and dermal nevi located at the dermis), histological patterns and clinical patterns. The majority are totally benign with no, or very limited, malignant potential, although it has been shown that multiple common nevi is a strong risk factor for melanoma. [49, 40]. For example all Spitz nevi lesions in adults should be excised for histopathologic evaluation [88]. Figure 2.3-c shows an example of a melanocytic Nevus (Blue Nevus).

Atypical or dysplastic nevi Some nevi lesions have architectural and cytological atypia, and they are called dysplastic nevi, also known as: atypical mole, atypical nevus, Clark's nevus, dysplastic melanocytic nevus. Atypical nevi are defined based on abnormal clinical features (by naked-eyes usually) and dysplastic nevi are defined by abnormal histological features (by biopsies). Atypical nevi are generally larger than ordinary moles ($> 6mm$ in diameter) and have irregular and indistinct borders. They are often asymmetrical and their color frequently is not uniform and ranges from pink to dark brown; they usually are flat, but parts may be raised above the skin surface [82, 21]. Dysplastic nevi can be found anywhere, but are most common on the trunk in men, and on the calves in women. The clinical importance of atypical nevi lies in their association with increased melanoma risk [21, 33, 29]. An individual with multiple atypical nevi or a family history of multiple atypical nevi or melanoma has an increased risk of developing superficial spreading melanoma. Figure 2.3-d shows an example of an atypical nevus (Clark's nevus).

Benign non-melanocytic lesions

Seborrhoeic keratosis Seborrhoeic keratosis is a benign, often pigmented, tumour composed of epidermal keratinocytes. These lesions are very common, especially among the elderly, which can

be flat but are more commonly verrucous in their appearance. Seborrhoeic keratosis can also resemble melanoma skin cancer in terms of the clinical ABCD features, though they are unrelated to melanoma because these are benign non-melanocytic lesions [82]. Figure 2.3-e shows an example of a seborrhoeic keratosis lesion.

Dermatofibroma A dermatofibroma is a common benign fibrous skin lesion. It is due to a non-cancerous growth of dermal dendritic cells. Dermatofibromas most often occur on the legs and arms. Once developed, they usually persist for years. They appear as firm-feeling nodules, often yellow-brown in colour, sometimes pink and sometimes quite dark, especially in dark coloured skin [82]. Figure 2.3-f shows an examples of a dermatofibroma lesion.

2.1.3 Skin Cancer

Skin cancer is by far the most common of all cancers. As discussed in the previous section, skin lesions can have melanocytic and non-melanocytic origins. So, skin cancers can be divided into two major categories as well: melanocytic and non-melanocytic.

Malignant non-melanocytic lesions

The most common non-melanocytic skin cancers are basal cell carcinoma (BCC) and squamous cell carcinoma (SCC), which are briefly explained in the following sections.

Basal cell carcinoma Basal cell carcinoma (BCC) is the most common type of skin cancer. BCC arises in cells called basal keratinocytes in the deepest layer of the epidermis. It rarely metastasizes or kills [111]. However, because it can cause significant destruction and disfigurement, it is still considered malignant by invading surrounding tissues. Statistically, approximately 3 out of 10 Caucasians may develop a basal cell cancer within their lifetime [111]. BCC grows by direct extension and appears to rely on the surrounding supportive tissue to grow. Therefore, it does not metastasize through blood vessels or lymphatics [42, 111]. Pigmented basal cell carcinoma is a cutaneous condition, a subtype of BCC, that exhibits increased melanization. In some cases, it may be difficult to distinguish deeply pigmented or even non-pigmented basal cell carcinoma from melanoma [11]. The skin changes caused by this skin cancer depend on the type of BCC involved. The most common appearance is of a raised pink or pearly white bump that may have a translucent, rolled, pearly edge and small visible blood vessels [11]. Pigmented BCC may look like a mole with a pearly border.

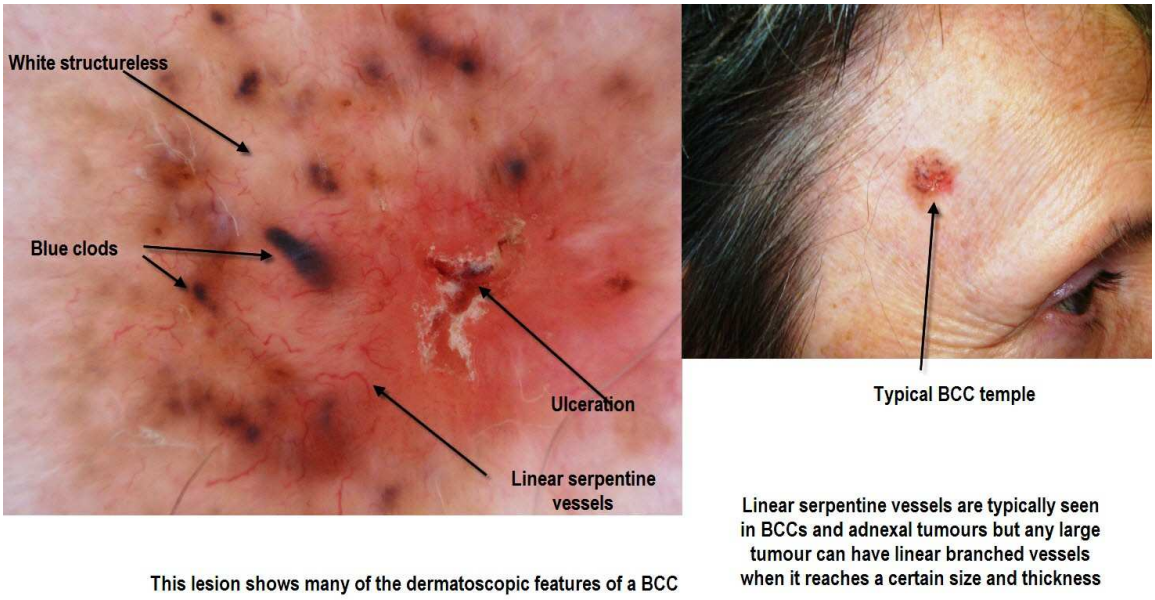

Figure 2.4: An example of basal cell carcinoma. The dermoscopy structures are annotated by experts. Images are taken with permission from [70].

Another type of BCC is flat and scaly with a waxy appearance and an indistinct border [11]. Figure 2.4 shows an example of BCC in which the dermoscopy structures used for diagnosis are annotated by experts [70].

Squamous cell carcinoma Squamous cell carcinomas (SCC) arise from the keratinocytes of the epidermis. SCCs begin when the atypical keratinocytes grow through the basement membrane and invade the dermis. When growing only in the epidermis they are considered precancerous, and this condition is called actinic keratosis. More advanced changes with full epidermal thickness dysplasia but no dermal invasion is called squamous cell carcinoma in-situ, or Bowen's disease. Once an invasive SCC has developed it has metastatic potential and can be fatal [95]. Figure 2.5 shows an example of SCC along with the dermoscopy structures annotated by experts [70].

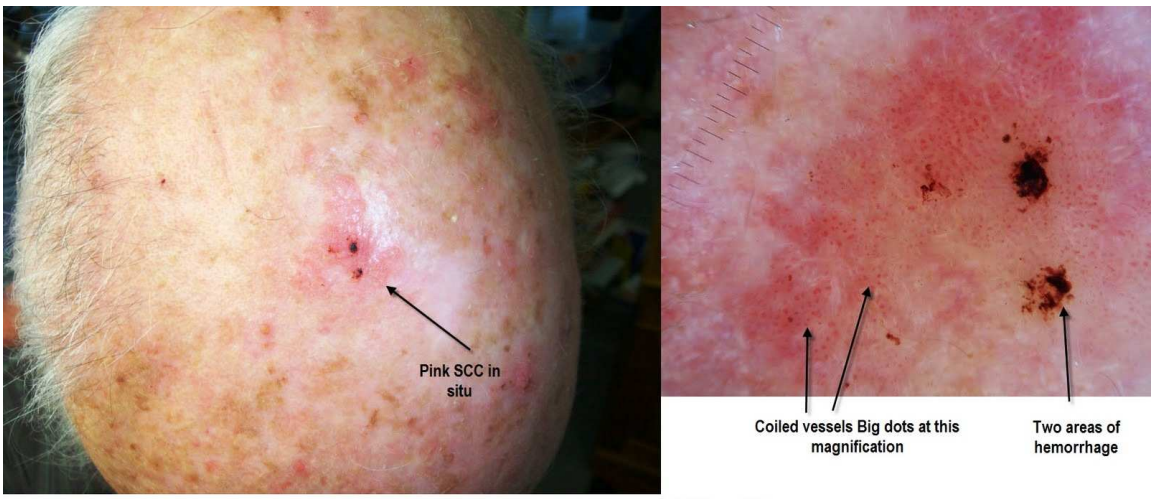

Figure 2.5: An example of squamous cell carcinoma. The dermoscopy structures are annotated by experts [70].

Melanoma: Malignant melanocytic lesion

Melanoma is a malignant tumor of melanocytes. Melanocytes are cells that produce the melanin, dark pigments responsible for the color of skin. They predominantly occur in skin, but are also found in other parts of the body including the bowel and the eye. Melanoma is less common than other skin cancers. However, it is much more dangerous and causes a large majority of skin cancer deaths since it can spread in the body [42]. As long as the malignant clone is only growing in the epidermis, the lesion is called a melanoma in-situ. When the malignant melanocytes invade the dermis, the lesion has become an invasive melanoma (they may have metastatic potential). The level of invasion in the dermis, through to the subcutaneous fat, is measured during histopathologic examination of the tumour after excision. Two measurements are made; the invasion depth according to Breslow is the thickness, in millimetres, from the stratum granulosum in the epidermis to the deepest invasive melanoma cell [20]. Another measurement system, called Clark, describes the thickness of a melanoma in relation to its penetration into the skin layers where level I represents intraepidermal growth, i.e. in-situ, level II a few cells in the papillary dermis, level III occupation and expansion of the papillary dermis, level IV invasion of the reticular dermis and level V invasion into subcutaneous fat [27].

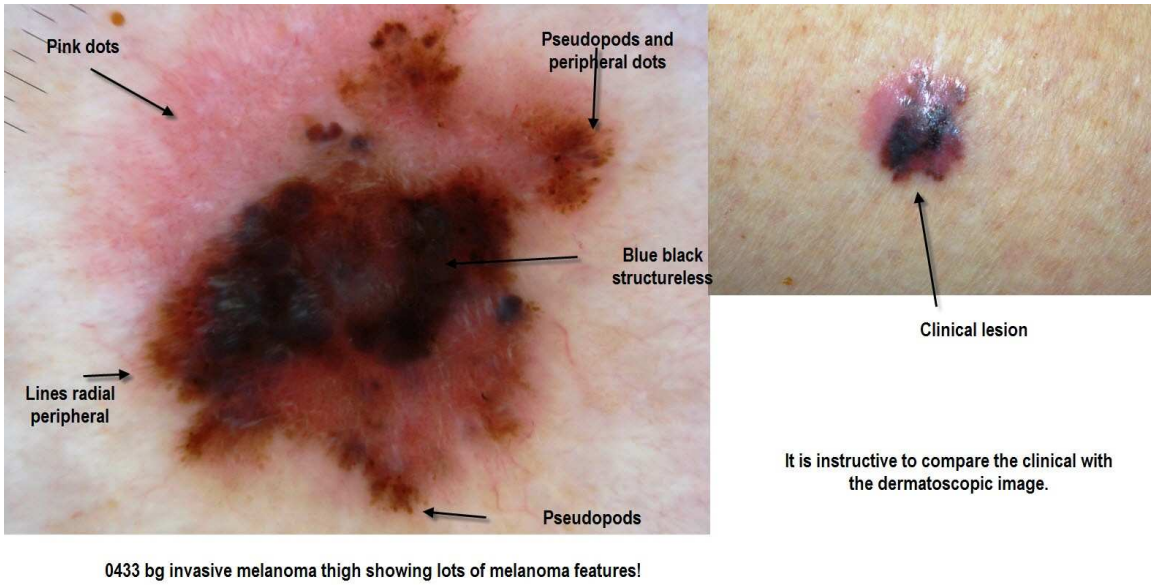

Figure 2.6: A melanoma lesion with indicative features. Images are taken with permission from [70].

Melanomas are divided into subsets due to clinical and pathological features; superficial spreading melanoma (SSM), nodular melanoma (NM), lentigo malignant melanoma (LMM) and acral lentigious melanoma. Figure 2.6 shows an example of melanoma (SSM) in which the dermoscopy structures are annotated by experts [70].

Superficial spreading melanoma is the most common type of melanoma. About 70% to 80% of all melanomas are this type. They are most common in middle aged people. To start with, they tend to grow outwards rather than downwards into the skin in the radial growth phase. It is not usually at risk of spreading to other parts of the body until it begins to grow downwards into the deeper layers of skin [82].

Nodular melanoma tends to develop quite quickly. It is found most often in middle aged people found on the chest or back. It begins to grow downwards, deeper into the skin, quite quickly if it is not removed. There is often a raised area on the skin surface with this type of melanoma. Nodular melanomas are often very dark brownish black, or black, in colour. They may not necessarily develop from a mole which was already there, however a rapidly-growing nodular melanoma can arise within superficial spreading melanoma and start to proliferate more deeply within the skin [82].

Lentigo maligna is an early form of melanoma often reported as in situ melanoma in which

the malignant cells are confined to the epidermis. It occurs in sun damaged skin so is generally found on the face or neck, particularly the nose and cheek. It grows slowly over 5 to 20 years or longer. It is diagnosed when the malignant melanoma cells have invaded into the dermis and deeper layers of skin. Lentigo maligna has a lower rate of transformation to invasive melanoma than the other forms of melanoma in situ. Thus, these flat lesions sometimes grow to enormous size without being dangerous. The risk of lentigo maligna relates to sun damage. Thus lentigo maligna is more common in outdoor workers and in older people with sun damaged skin and it is more common in males than females [82].

Acral lentiginous melanoma is type of melanoma arising on the palms or soles. It is characterized by its site: palm, sole, or beneath the nail. It is more common on feet than on hands. It can arise de novo in normal-appearing skin, or it can develop within an existing melanocytic naevus (mole). Acral melanoma starts as a slowly-enlarging flat patch of discolored skin. At first, the malignant cells remain within the epidermis. This is the in-situ phase of melanoma, which can persist for months or years and it becomes invasive when the melanoma cells cross the basement membrane of the epidermis and malignant cells enter the dermis. A rapidly-growing nodular melanoma can also arise within acral melanoma and proliferate more deeply within the skin [82].

2.2 Dermoscopy and Clinical Diagnosis

In the 1990s, light-based visual technologies were adopted to augment the clinical diagnosis of melanoma. Dermoscopy is a noninvasive method that allows in vivo evaluation of colors and microstructures of the epidermis, the dermo-epidermal junction, and the papillary dermis not visible to the naked eye. During a dermoscopy assessment, the pigmented skin lesion is covered with liquid (usually oil or alcohol) and examined under a specific optical system. Applying oil reduces the reflectivity of the skin and enhances the transparency of the stratum corneum. This allows visualization of specific structures related to the epidermis, the dermo-epidermal junction, and the papillary dermis, and it also suggests the location and distribution of melanin.

In the last few years dermoscopes with LED light with polarization have been introduced and by using polarized light, immersion liquid is no longer necessary, and some of these instruments do not need direct skin contact. Non-polarized versus polarized light and contact versus non-contact dermoscopy gives somewhat different appearance of the examined lesions in regards to colour and visualization of vessels. In a study by Benvenuto-Andrade et al. they report excellent agreement for most dermoscopic colours, with the exception of blue-white veil and pink (red) colour when

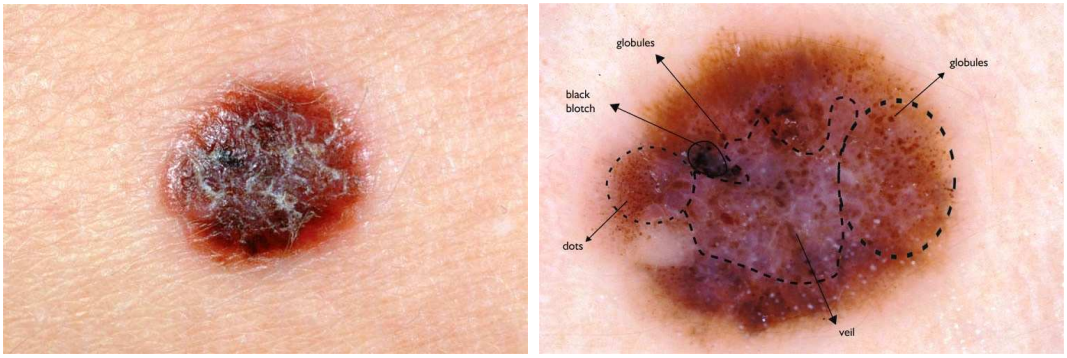

(a) (b)

Figure 2.7: a) An image of a lesion under clinical view (naked eye). b)shows the same lesion under a dermoscope with oil immersion. Images are taken from [100] with permission.

comparing non-polarized and polarized light [15]. They also conclude that most dermoscopic structures had fair to perfect agreement, with the exception of milia-like cysts and comedo-like openings, which seem to be better visualized with non-polarized light [15] and the polarized light improves the visualization of red areas and vessels, especially the latter with non-contact dermoscopy [15].

Figure 2.7-a shows an image of a lesion under the clinical (naked eye) view and 2.7-b shows the same lesion under a dermoscope with oil immersion. Significant features are marked in the image. These structures are specifically correlated to histologic features. The identification of specific diagnostic patterns related to the distribution of colors and dermoscopy structures can better suggest a malignant or benign pigmented skin lesion [11]. The use of this technique provides a valuable aid in diagnosing pigmented skin lesions. Because of the complexity involved, this methodology is reserved for experienced clinicians.

2.2.1 Image Acquisition - Digital Dermoscopes

There are different kinds of dermoscope and they are roughly divided into analogue and digital types. Digital types are easier to take and store dermoscopy images, however analogue types are more widely used. Figure 2.8 *a-e* show Heine Delta 10Ⓡ, Heine Delta 20Ⓡ, DermLite III DL3Ⓡ, DermogeniusⓇ, and DermLite II ProⓇwhichⓇare analogue dermoscopes. All of them except *a* can be attached to a digital camera to provide advantages of digital dermoscopy. DinoLite, Handyscope and DermScope are examples of digital dermoscopes shown in Figure 2.8 *f-h* respectively.

There is a study in the literature that compares images of a dysplastic compound melanocytic

nevus and a thin malignant melanoma under five different handheld dermoscopes (Heine Delta 10®, Heine Delta 20®, Dermogenius and DermLite Foto 37®with and without glass plate). The magnification was identical in all dermoscopes. The authors show that in the newer dermoscopes, the image quality with regard to color and visible differential structures is distinctly improved compared to the dermoscope (Heine Delta 10®) with only one light source [18]. Three advanced dermoscopes will be reviewed briefly here.

DermLite II Pro

With new advances in technology, dermoscopes have also evolved. DermLite from 3Gen Co. is a dermoscope consisting of a magnifying lens encircled by light-emitting diodes that can be adjusted for polarization. This multi-spectral dermoscope provides color visualization; ranging from white light epiluminescence, surface pigmentation using blue light, superficial vascularity under yellow light, and deeper pigmentation and vascularity with the deeper-penetrating red light frequency. A new version of the DermLite can be used for the evaluation of pigmented lesions and non-pigmented skin cancers, scalp disease, and vascular patterns. The DermLite can be attached to a camera to record images and has a retractable faceplate for use with immersion oil. DermLite Pro, shown in the figure 2.8-*d*, is one of the most widely used dermoscopes. Recently, the company has provided an iPhone kit that users can snap the DermLite onto their iPhone cameras.

Dino-Lite Pro USB Dermoscope with Polarizer

The DinoLite is a compact digital microscope with USB - PC connectivity. Magnification ranges from 10X to 200X (adjustable single lens) to 500X with white polarized LED lights. The LED's light is around the 400 nm spectrum. The polarization feature allows the user to reduce the effect of reflections and glare when looking at highly reflective surfaces. Adjustment of the polarization feature is performed by way of a rotating collar, allowing the user to examine objects with varying levels of polarization. Figure 2.8-*f* shows an image of the DinoLite dermoscope.

Handyscope by FotoFinder Systems, Inc.

Handyscope from FotoFinder is a new mobile dermoscope, shown in the figure 2.8-*g*, that allows one to take polarized mole pictures of up to 20X magnification and to save them in the iPhone application [4]. Handyscope can be used for tele-dermatology, combining latest communication

(a) Heine10®

(b) Heine20®

(c) DermLite III DL3®

(d) DermLite(TM) DL100®

(e) DermLite II Pro®

(f) DinoLite

(g) Handyscope

(h) DermScopeCanfield

Figure 2.8: Figures *a*, *b*, *c*, *d*, and *e* show analogue dermoscopes. All of them, except *a*, are attachable to digital cameras to function as digital dermoscopes. DinoLite, Handyscope, and DermScope are modern digital dermoscopes shown in *f*, *g*, and *h* respectively.

technology of iPhone with a tool for skin cancer screening. Dermoscopy images taken with iPhone camera and the dermoscope attachment can be e-mailed to other specialists for a second opinion. Mobile dermoscopes can provide a good mobility for experts while they are connected to servers through wifi connections to provide an integrated dermoscopy station.

DermScope by Canfield Scientific, Inc.

The new DermScope from Canfield, shown in Figure 2.8-*h*, is another intelligent dermoscope made for iPhone that addresses all of the important modes of skin visualization including contact and non-contact images with the dual-lighting modes for white light and the cross-polarized light. The DermScope's design has been optimized for iPhone 4 and It has optical zoom of 20x and the viewing field is 15 mm [2].

2.2.2 Dermoscopy - Clinical Diagnostic Methods

In this section, the four diagnostic algorithms, which have gained the largest interest among dermoscopy users, will be briefly reviewed. In the first step, the algorithm identifies whether a lesion is melanocytic or non-melanocytic. If yes, various algorithms may be used to distinguish benign melanocytic lesions from malignant melanoma.

Pattern analysis was the first dermoscopic method presented for diagnostics of pigmented skin lesions [85]. This method has further been modified and refined by the International Dermoscopy Society (IDS). The other three algorithms with the largest impacts are ABCD rule, Menzies method and the 7-point checklist which will be described in the current chapter. All of these methods were evaluated in the 2000 consensus net meeting [100], showing similar results on sensitivity for melanoma, but specificity differed slightly in favor of pattern analysis [100]. In fact, the ABCD rule, Menzies method and the 7-point checklist attempt to simplify the pattern analysis method by analyzing only a small sub-set of dermoscopic structures and create a scoring system. As a result, the accuracy of these simplified systems are somewhat lower than the full system, pattern analysis. For more details on the dermoscopy of pigmented skin lesions please refer to [102].

Pattern Analysis

Diagnosis based on pattern analysis demands a critical assessment of the dermoscopic features seen in a pigmented skin lesion. It provides the initial definitions of many patterns, called dermoscopic structures, which have proven to be critical in the clinical diagnosis of skin lesions.

	Low	Medium	High
Colours: few vs many brown, black, red, white, blue Score 1 point for each colour	1-2 colours (1-2 points)	3-4 colours (3-4 points)	5-6 colours (5-6 points)
Architecture: order vs disorder Score 0-2 points	None or mild (no points)	Moderate (1 point)	Marked (2 points)
Symmetry vs asymmetry border, colours and structures Score 0-2 points	Symmetry in 2 axes (no points)	Symmetry in 1 axis (1 point)	No symmetry (2 points)
Homogeneity vs Heterogeneity Pigment network, dots/globules blotches, regression, streaks blue-white veil, polymorphous vessels Score 1 point for each structure	one structure (1 point)	2 of structure (2 points)	$3 \geq$ structures (3-7 points)

Table 2.1: CASH is used for the dermoscopic differentiation between benign melanocytic lesions and melanoma using pattern analysis [53]. Add up the scores for a total CASH score (2 to 17). The score of 7 or less is likely benign and the CASH score of 8 or more is suspicious of melanoma

The first step is to decide whether the lesion is melanocytic or non-melanocytic by searching for the presence of pigmented structures or the specific features of non-melanocytic lesions. The main goal for the second step is to make an accurate differential diagnosis between benign melanocytic lesions and melanomas. The important features in distinguishing these two groups are the overall general appearance of color, architectural order, symmetry of pattern, and homogeneity, also known by the acronym CASH coined by Kopf et al. [53]. Melanocytic nevi have few colors, a regular design, and symmetrical patterns. In contrast, malignant melanoma often has several colors, architectural disorder, asymmetrical patterns, and heterogeneity. Table 2.1 shows the details of this approach. It adds up the CASH scores for a total score of 2 to 17. The score of 7 or less is likely benign and the CASH score of 8 or more is suspicious of melanoma.

Semi quantitative/quantitative dermoscopic algorithms have been presented as more simplified diagnostic methods for differential diagnosis between malignant and benign melanocytic lesions.

ABCD

There are two ABCD rules: clinical and dermoscopic. The ABCD rule, promoted by the America Cancer Society and the Canadian Cancer Society, describes the clinical features of melanomas using

mnemonics: A for Asymmetry varies 0-2, B for Border irregularity varies 0-8, C for Colour variegation varies 1-6 and D for Diameter $>= 6mm$. There is no scoring system for the clinical rule [79]. For the dermoscopic ABCD rule [105], D is used for Differential structural components or Dermoscopic structures (pigment network, structureless areas, dots, aggregated globules, branched streaks). There is a formula to score and differentiate between benign melanocytic lesions and melanoma. The formula for calculating total score is:

$$\textit{Total Score} = (A_{\text{score}} * 1.3) + (B_{\text{score}} * 0.1) + (C_{\text{score}} * 0.5) + (D_{\text{score}} * 0.5)$$

The interpretation of the total score says if the score is < 4.75, the lesion is a benign melanocytic lesion; A total score between 4.75 and 5.45 is considered a suspicious lesion and a close follow-up or excision is recommended); and the score > 5.45 indicates that the lesion is highly suspicious for melanoma. ABCDE is also a modified ABCD that adds E for Elevation or Evolution for melanoma diagnosis.

7-Point Checklist

The dermoscopic seven point checklist is another attempt to formalize/simplify pattern analysis by assigning points to specific dermoscopic structures. This checklist consists of 3 major features: atypical pigment network, gray-blue areas and atypical vascular pattern as well as 4 minor criteria: streaks, blotches, irregular dots and globules and regression patterns. When any of the major features is detected in a melanocytic lesion, immediate help from health professionals is recommended. The presence of any minor features is advised to be monitored regularly. The minor criteria are worth 1 point each whereas the major are worth two. A final score is calculated by summing the point value of each criteria that is present. If the score is ≥ 3, then the lesion is classified as melanoma [59, 100].

Recently, a further simplified algorithm has been developed for non-experts to screen for skin cancers. This method considers only 3 criteria and is called 3-point. Asymmetry, atypical network and blue-white structures are the three indicative criteria of this method [101].

Menzies Method

Menzies method is another simplified version of pattern analysis method [43] that distinguishes the dermoscopic features of benign melanocytic lesions from melanoma by two negative and positive

feature sets. The negative set includes symmetry of pigmentation pattern and presence of only a single color and the positive set contains 9 positive features which are blue-white veil, multiple brown dots, pseudopods, radial streaming, scarlike depigmentation, peripheral black dots/globules, multiple colors (5 or 6), multiple blue/gray dots and broad pigment network. All of the features are defined in [72]. For melanoma to be diagnosed a lesion must have neither of both negative features and 1 or more of the 9 positive features.

2.2.3 Dermoscopy Colors

Accurate evaluations of the color of a pigmented skin lesion, the degree of pigmentation, and the distribution of the colors within the lesion are the most important elements of a dermoscopy examination. The epidermis usually appears as white, but acanthosis results in a grayish-brown or brownish-yellow color [102]. Melanin is the most important pigment in determining different structural and chromatic patterns. The pigmented skin lesion can have a different degree and distribution of pigmentation depending on the location of melanin in different layers of the skin [102]:

- Upper epidermis (stratum corneum, stratum spinosum) - Black
- Dermo-epidermal junction - Light-to-dark brown
- Papillary dermis - Slate blue
- Reticular dermis - Steel blue

Other possible colors include various shades of white and red. White shades are related to regression and may be seen with melanomas, benign melanocytic nevi (halo nevus), and non-melanocytic lesions (lichenoid keratosis, scars, vitiligo). Red shades are related to increased vascularization in tumors, an increased number of capillary vessels, and bleeding within the lesion. If bleeding persists and crust develops, the color ranges from red-black to blue-black. Figure 2.9 shows the correlation of the dermoscopy colors with histology. A good evaluation of colors and their relative distribution is essential for achieving the correct clinical diagnosis of a pigmented skin lesion [102].

2.2.4 Pigment Network

The most important feature of melanocytic lesions is the pigment network, which consists of pigmented network lines and hypo-pigmented holes [11]. The presence of an atypical pigment network

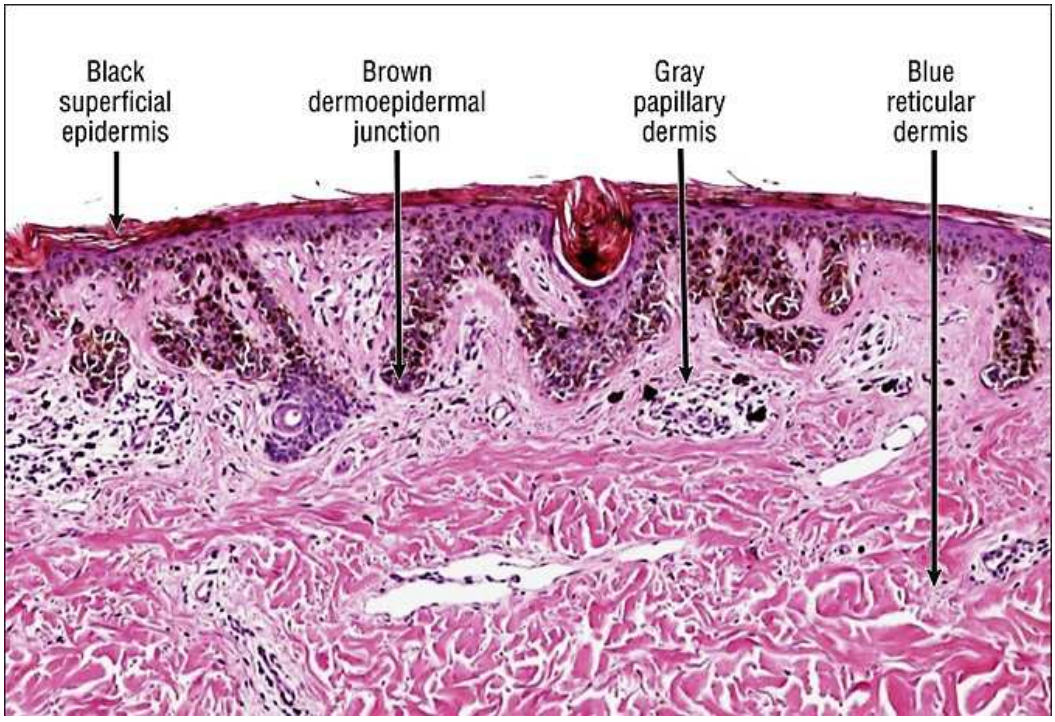

(a)

Figure 2.9: a) Colors allow the physician, to some extent, to draw conclusions about the localization of pigmented cells within the skin. Black and brown indicate pigmentation in the epidermis, while gray and blue correspond to pigmented cells within the superficial and deep dermis, respectively [115].

is indicated by a black, brown, or gray network with irregular meshes and thick lines. A typical pigment network is defined as a light- to-dark-brown network with small, uniformly spaced network holes and thin network lines distributed more or less regularly throughout the lesion and usually thinning out at the periphery [100]. These structures show prominent lines, homogeneous or inhomogeneous meshes. The anatomic basis of the pigment network is either melanin pigment in keratinocytes, or in melanocytes along the dermoepidermal junction. The reticulation (network) represents the rete ridge pattern of the epidermis. The holes in the network correspond to tips of the dermal papillae and the overlying suprapapillary plates of the epidermis [10, 100].

Figure 2.10-a and 2.10-c show examples of *Present* and *Absent* lesions and 2.10-b and 2.10-d show both images enlarged. In melanocytic nevi, the pigment network is slightly pigmented. Light-brown network lines are thin and fade gradually at the periphery. Holes are regular and narrow.

In melanoma, the pigment network usually ends abruptly at the periphery and has irregular holes, thickened and darkened network lines, and treelike branching at the periphery where pigment network features change between bordering regions [102]. Some areas of malignant lesions manifest as a broad and prominent pigment network, while others have a discrete irregular pigment network. The pigment network also may be absent in some areas or the entire lesion.

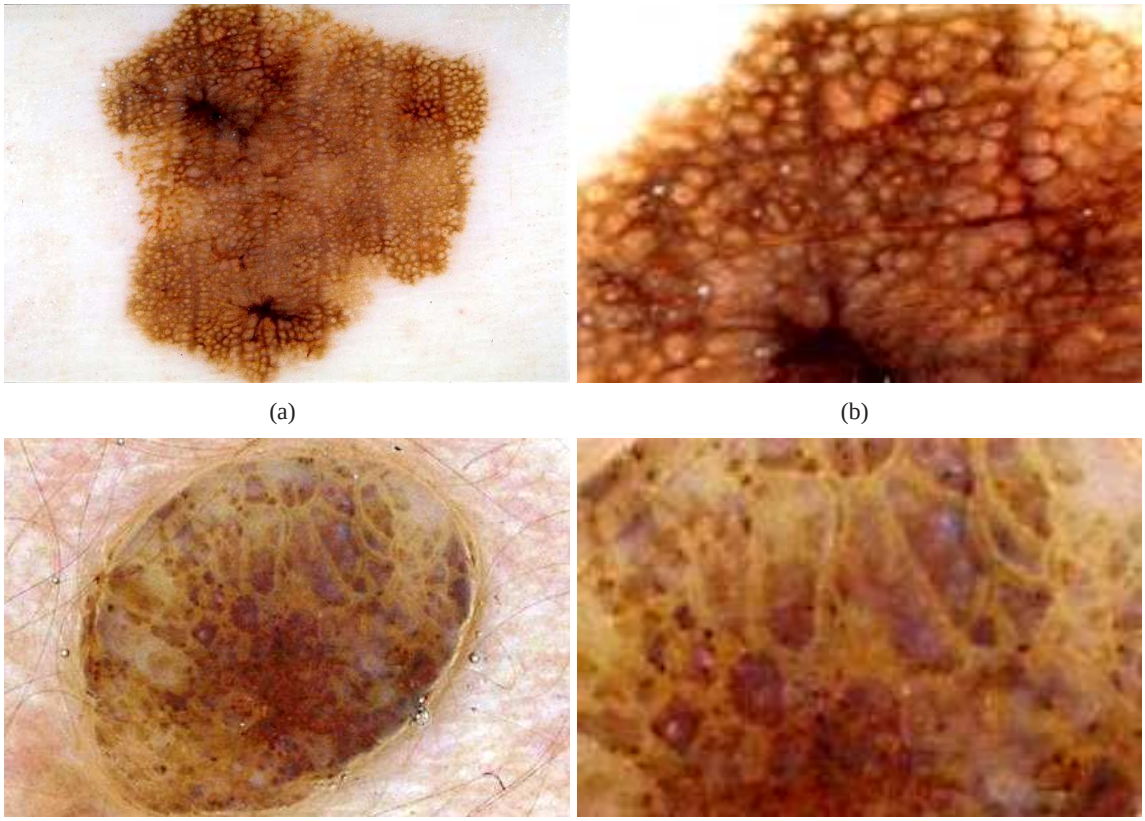

(a) (b)

(c) (d)

Figure 2.10: a) *Present*: A lesion containing a pigment network. b) Enlarged pigment network. c) *Absent*: An image of a lesion without pigment network. d)Enlarged *Absent* image.

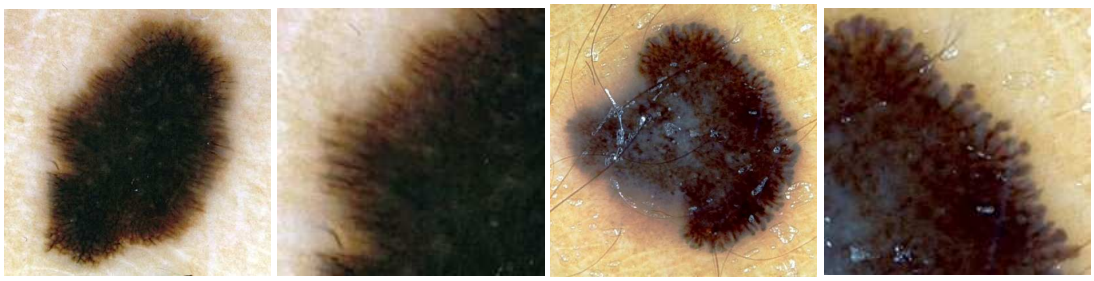

(a) (b) (c) (d)

Figure 2.11: Examples of streaks.(a)and (c) are lesions containing *radial streaming* and *pseudopods* pattern respectively. (b) and (d) are magnified images to show the linear structures. Images are taken with permission from [100].

2.2.5 Streaks

Clinical Definition

Streaks is a term used interchangeably with radial streaming or pseudopods because of the same histopathological correlation [19]. We use the term streaks to include both radial streaming and pseudopods, shown in Figure 2.11-a and Figure 2.11-c respectively . Radial streaming is a linear extension of pigment at the periphery of a lesion as radially arranged linear structures in the growth direction, and pseudopods represent finger-like projections of dark pigment (brown to black) at the periphery of the lesion [19]. Figure 2.11-a shows an example of a lesion with the radial streaming pattern, enlarged in Figure 2.11-b. Figure 2.11-c shows an example of a lesion with the pseudopods pattern. The enlarged image is shown in Figure2.11-d. in order to ensure accurate recognition, streaks are numerated only when at least 3 near linear and parallel structures are clearly visible [100]. Streaks are *local* dermoscopy features of skin lesions, however they can correlate with a *global* pattern of skin lesions called a starburst pattern if symmetrically arranged over the entire lesion.

The Menzie's scoring method states that irregular streaks are never distributed regularly or symmetrically around the lesion [75, 100]. Also, based on the 7-Point checklist [85, 9, 100] irregular streaks should not be clearly combined with pigment network lines. These definitions are used later in Chapter 6 to define discriminative models towards automated *Regular*/*Irregular* classifications of streaks.

(a) (b) (c)

Figure 2.12: Examples of *Absent*, *Regular* and *Irregular* streak images. (a) shows a lesion without streaks (*Absent*). (b) illustrates a lesion with a complete symmetric regular streak pattern called *starburst*, and in (c) a melanoma with irregular streaks which are partially distributed. (b) and (c) are called *Present* images. (a) is taken from [100], (b) and (c) are from [10] with permission.

Mathematical definition

The above clinical definition is translated to mathematical concepts with justified parameters to be captured by image processing techniques: 1) Streaks are three or more linear structures co-radially oriented in the boundary which is a contour with the thickness equal to $1/3$ of the minor axis of the lesion. 2) Streaks are darker than their neighborhood. 3) Streaks are shorter than the $1/3$ of the minor axis of the lesion and they should be longer than one percent of the major axis. 4) Streaks do not branch and their curvature is less than one. 5) A symmetric and regular distribution of streaks all over the lesion forms a starburst pattern. These specific mathematical definitions are based on the author's distillation of salient features, and not from the literature.

Figure 2.12 shows examples of lesions with no streaks (*Absent*), *Regular* (*Present*), and *Irregular* (*Present*) streaks. Figure 2.12-a shows *Absent*, 2.12-b shows a starburst or complete pattern with *Regular* streaks, and Figure 2.12-c shows a melanoma lesion with irregular streaks and a partial pattern.

Diagnostic importance

Streaks are important morphologic expressions of malignant melanoma, specifically melanoma in the radial growth phase [75, 103]. Irregular streaks are one of the most critical features (included in almost all of dermoscopy procedures) that shows the highest association with melanoma. Also Menzies et al. [75] found pseudopods to be one of the most specific features of superficial spreading melanoma which is a subset of malignant melanoma. In addition, symmetric streaks (starburst pattern) are one of the specific dermoscopic criteria to differentiate usually benign Spitz nevi (a dark

nevus common in children) from melanoma, thus increasing diagnostic accuracy for pigmented Spitz nevus from 56% to 93% [104]. However, all lesions in adults exhibiting a starburst pattern should be excised for histopathologic evaluations [75]. Therefore detection and analysis of streaks and starburst pattern can be a significant step towards computer-aided diagnosis of skin lesions and melanoma detection.

2.3 Commercial Computer-aided Diagnostic Systems

Advances in computer science and applied mathematics are now allowing the basic technology of dermoscopy to be extended to a more complex application: predicting whether observed spots are cancerous. Several teams are working toward computer-assisted diagnosis of melanoma using different mathematical and analytical strategies. Computer software can be used to archive skin images and allow remote diagnosis and reporting by a dermatologist (digital epiluminescence microscopy, teledermoscopy, mole mapping). MoleMap NZ is such a system which is used for archiving and patient management.

Some systems such as SIAscope, SolarScan (also called MoleTrac) and MelaFind offer smart programs to aid in diagnosis by comparing the new image with stored cases with typical features of benign and malignant pigmented skin lesions. Given good images of the appropriate lesion, they may be as accurate as an expert dermatologist. However, they are not particularly useful for non-pigmented lesions and they can't make the decision which lesions should be imaged [108, 82, 39, 87, 71]. Table 2.2 compares some of these systems.

To the best of our knowledge, none of the above systems is based on the detection and analysis of specific dermoscopic patterns which is the main stream in clinical diagnosis of lesions. They are built based on the general image processing approaches (such as color, texture and other image statistics of the entire lesion) and image retrieval methods that cannot find the dermoscopy structures and their irregularities which are crucial features for the melanoma diagnosis. If we want to develop computer-aided diagnosis systems, we should address the important step of the pattern analysis approach which is the segmentation and analysis of the dermoscopy structures.

2.3.1 SolarScan Melanoma Monitoring

SolarScan is a device priced for use by individual practitioners and developed by Australian startup Polartechnics, with assistance from Australia's Commonwealth Scientific and Industrial Research Organization (CSIRO) and the Sydney Melanoma Unit [71]. SolarScan uses image analysis, which

has turned diagnostic criteria used by doctors into defined decision trees that lead toward or away from a decision to help general physicians (GPs) diagnose melanoma [73]. The device works by capturing an image of a patient's skin spot using an object shaped like a hairdryer with a built-in surface microscope. Image analysis software removes extraneous things from the image like hairs and oil bubbles and analyses the spot's features such as its shape and colour. SolarScan then compares the features against images of melanomas and non-melanomas in a database, returning an advice to a GP. A record of the spot's status can be stored in Polartechnics' Body Map software so that it can be rechecked another time if necessary [73].

2.3.2 MoleMax

MoleMax (Derma Medical Systems, Vienna, Austria) is a computer-based polarized-light dermoscope [69]. The polarized-light source is used with the hand-held video dermoscope for close-up imaging and does not require any oil immersion or contact fluids between the skin and the video head. The MoleMax software is convenient for follow-up examinations, as the transparent overlay feature performs a standardized comparison of images with previous data. Apart from live-video dermoscopy, MoleMax also allows total-body photography and creates a digital map of the skin of patients with high-risk factors and numerous pigmented lesions. These images can be used as a baseline for comparison when suspicious changes are found and for follow up melanoma screening visits [87]. Molemax automatically analyses captured dermoscopy images giving a score that helps to determine if a pigmented skin lesion is benign or malignant. The automatic algorithm analyses the lesion based on the ABCD factors. Although it is not a final diagnosis the risk score is based on a large and proven database.

2.3.3 SIAscope

The SIAscope (SIA: Spectrophotometric Intracutaneous Analysis) is an automated dermoscopy device that uses 12 wavebands to evaluate the skin, rather than conventional broadband white light. It is a handheld medical device used in conjunction with the MoleMate and MoleView range of software [44, 78]. Patterns of collagen, vascular and melanin distribution are identified within the lesion from the spectrophotometric analysis of a skin lesion.

- MoleMate is a non-invasive melanoma screening device that has been designed for General Practitioners and skin specialists.
- MoleView assists in the management of patients for skin cancer screening.

SYSTEM	SEN.	SPEC.	ADVANTAGES	DISADVANTAGES
MoleMax	N/A	N/A	Two camera system no oil immersion transparent overlay follow up total body photography	No computer analysis
MelaFind	95_100%	70_85%	multispectral image sequence Handheld scanner	
SolarScan	91%	68%	database for comparison; accurate calibration graphic map of body	Requires oil immersion

Table 2.2: Comparison of emerging technologies in melanoma diagnosis. This table originally appeared in the European Journal of Dermatology [84] and it is cited from [87].

- MoleView+ provides the mole mapping functionality for the long term management of patients.

2.3.4 MelaFind

MelaFind is a multispectral digital dermoscope with a specialized imaging probe and software to assist with differentiation between early melanoma and other skin lesions [32, 71]. A hand-held imaging device that shines light of 10 different, specific, wavelength bands is used to collect data. Proprietary processing software is used to extract specific features from the images [50, 64]. The software determines the edge of the lesion and generates a 10 digital image sequence. The images are then analyzed for wavelet maxima, asymmetry, color variation, perimeter changes, and texture changes, and the output is a binary recommendation of whether or not to perform a biopsy [87]. The results of a clinical trial were published in April 2008, leading to submission of the MelaFind to the FDA and recently it has been approved for use in the United States.

Many of the available systems either were discontinued or have not been able to pass the FDA evaluation process yet. There is a big question why these systems are not successful enough to be used in clinics. To answer such a fundamental question, after taking dermoscopy courses, talking to experts in this field and reviewing the current systems, we came up with the idea that there is a big missing step in the available system designs that may be the main source of shortcomings. Dermoscopic structures (or texture, in image processing parlance) are the most prominent features for the clinical diagnosis of skin lesions and in almost all of the clinical approaches, decisions are made based on the presence and irregularities of critical dermoscopic structures. Therefore, to simulate

and develop an accurate computer program, segmentation and analysis of the dermoscopic features (such as pigment network, blood vessels, and etc.) are essential, otherwise the main strength of dermoscopes which is providing visual features is useless. In fact, dermoscopic structures were developed based on the observation of thousands of images and they have been shown to improve diagnostic accuracy. Therefore, failing to incorporate this wealth of information would be unfortunate.

To the best of our knowledge, none of the available commercial programs and systems can extract and analyze the dermoscopy structures comprehensively. In these systems, the vast majority of features which are used are based on general image processing methods of color or common texture analysis. Where texture features are employed, they are often used blindly, and an image processing method is applied directly without consideration for what exactly is being quantified or how it relates to clinical concepts. At very most, texture features use some aspects of the much simpler and less accurate ABCD rule that only considers general lesion characteristics instead of shape, color and geometric features of dermoscopy structures. Asking a computer to make a diagnosis without finding any dermoscopy structure is similar to asking a general physician without dermoscopy knowledge to make a diagnosis. Therefore, to have a comprehensive computer-aided diagnostic system, extraction and analysis of dermoscopy structures is an essential step.

We believe that with new advances in dermoscopy, the texture analysis problem should be changed to an object recognition problem that involves identification, segmentation and recognition of individual shapes and structures in skin lesions and this will be employed to identify and classify specific dermoscopic structures. It is hoped that this will lead to the development of many new approaches that can be included to increase the diagnostic accuracy of automated systems.

2.4 Summary

In this chapter, basics of human skin biology are described and different types of common skin lesions are briefly reviewed, and the new imaging system which is called digital dermoscopy and different clinical diagnostic method are introduced. We also defined and explained the two important dermoscopy structures, pigment network and streaks. Finally, we reviewed and evaluated the current computer-aided diagnostic systems.

Chapter 3

Previous Work

Computer-aided diagnosis of dermoscopy images has shown a great promise in developing a quantitative and objective way of classifying skin lesions. A non-invasive computer-aided diagnostic system typically consists of several components: image acquisition, image processing, and a classifier with a knowledge database. When a melanocytic lesion is captured in vivo as a digital image using a dermoscope, the characteristics of the lesion can be extracted from the digital image by image processing techniques. The image processing steps consist of a preprocessing step which includes calibration, image enhancement and removal of artifacts such as hairs and oil bubbles. Then a border detection should be applied to segment the lesion from normal skin and the lesion area should be investigated to find dermoscopic structures and irregularities. Feeding the features to a classifier which is connected to a medical knowledge database can generate a computerized diagnosis, suggesting whether the lesion is benign or malignant.

In this chapter, the previous work on the main stages of a computer-aided diagnosis system are discussed. First, we review the preprocessing phase that includes the lesion segmentation task, and then consider previous work on the automated detection of pigment networks and streaks, which are the important dermoscopic structures.

3.1 Pre-precessing

3.1.1 Removal of Artifacts

Dermoscopic images often contain artifacts such as illumination, dermoscopic gel, hair, skin lines, and ruler markings. As a result, there is a need for robust methods to remove artifacts and detect

(a) (b) (c)

Figure 3.1: Three examples of dermoscopy images with hair (a), oil bubbles (b) and low-contrast (c).

lesion borders in dermoscopy images. As shown in figure 3.1, hair pixels and oil bubbles, usually present in dermoscopic images, occlude some of the information of the lesion such as its boundary and texture. With new dermoscopes and using polarized light, oil or air bubbles are less common. However removing hairs from dermoscopy images remains a serious challenge and in a real-time computer-aided diagnosis systems, an automatic hair removal method that preserves all the lesion features is needed.

There are a few methods described in the literature to remove light, dark, thin and thick hairs. These studies mainly focused on measuring the hair detection error, ignoring the effect on the lesion's patterns. As a result, these hair removal methods often leave behind undesirable blurring, they disturb the texture of the tumor, and often result in color bleeding. Moreover, these methods required high computational cost. Abbas et al. in [5] have a comparative study on hair removal methods on dermoscopy images. They have classified the hair-removal methods into the following categories: linear interpolation techniques [67, 81, 94, 36], inpainting by non-linear-PDE based diffusion algorithms [14, 113] and exemplar-based methods [5, 6, 30, 109, 116]. A detailed description and comparison of each hair removal method is presented in [5].

3.2 Skin Lesion Segmentation

The segmentation of skin lesions is a crucial early step in the process of automatically diagnosing melanoma. Inaccurate segmentations will affect all downstream processes such as feature extraction, feature selection and the final diagnosis. Accurate segmentations are especially crucial for features that measure properties of the lesion border [66].

In recent years, many studies have focused on lesion segmentation in skin images [114, 68, 22,

24, 23, 57, 117, 119, 41, 76, 118]. First, Xu et al. [114] developed an automatic segmentation method for segmenting pigmented skin lesions in clinical images. Further, Li et al. [68] showed that adding 3D depth information to RGB color images improved segmentation in clinical images. For dermoscopy images, Celebi et al. [24, 23] recommended a fast and unsupervised approach based on the statistical region merging algorithm (SRM). A multi-direction gradient vector flow snake-based scheme is advised by Tang [107].

Celebi et al. in [22] reduce a dermoscopic image to 20 distinct colour groups, and assign labels to pixels based on the colour groups to which they belong. They then define a metric, the *J-value*, which measures the spatial separation, or isolation of each group. The *J-value* is derived from the separability criterion used by Fisher in Linear Discriminant Analysis [35]. Next, they define a localized *J-value* for a specific pixel by computing the metric over a neighborhood around the pixel. By varying the neighborhood size, they create several of these *J-images*. Multiscale methods are used to combine the images into a final segmentation. By creating a class map using color reduction, and employing various neighborhood sizes they are incorporating, on some levels, textural information into their segmentation.

In another attempt, Iyatomi et al. presented a dermatologist-like tumor area extraction algorithm (DTEA) [57]. The DTEA segmentation algorithm first obtains an initial segmentation by finding high-frequency components and then thresholding using the Otsu method [83]. Now the image is divided into many small regions which are merged until they are of sufficient size (at least 5% of the image). Then the subset of regions which is considered to belong to the lesion is selected via elaborate rules. Finally, to mimic dermatologists' tendency to conservatively segment the lesion, the border is slightly expanded.

3.3 Automatic Detection of Dermoscopy Structures

As a fundamental step towards computer-aided diagnosis of skin cancers, automatic detection and analysis of many local dermoscopic structures such as pigment networks and blood vessels, have been frequently addressed in the literature [47, 98, 91, 92, 34, 36, 8, 31, 17, 90]. Also, global pattern detection on dermoscopy images has been addressed by Serrano et al. [96] and Tanaka et al. [106].

In this section we review two of the most indicative dermoscopic features which are crucial towards computer aided diagnosis of melanoma. These structures include the pigment network, and streaks.

3.3.1 Pigment Network Detection

The automated detection of pigment network has received some recent attention [36, 48, 34, 8, 17, 31, 98, 96, 13]. Fleming et al. [36] report techniques for extracting and visualizing pigment networks via morphological operators. They investigated the thickness and the variability of thickness of network lines; the size and variability of network holes; and the presence or absence of radial streaming and pseudopods near the network periphery. They use morphological techniques in their method and their results are purely qualitative. Fischer et al. [34] use local histogram equalization and gray level morphological operations to enhance the pigment network. Anantha et al. [8] propose two algorithms for detecting pigment networks in skin lesions: one involving statistics over neighboring gray-level dependence matrices, and one involving filtering with Laws energy masks. Various Laws masks are applied and the responses are squared. Improved results are obtained by a weighted average of two Laws masks whose weights are determined empirically. Classification of these tiles is done with approximately 80% accuracy. Betta et al. [17] begin by taking the difference of an image and its response to a median filter. This difference image is thresholded to create a binary mask which undergoes a morphological closing operation to remove any local discontinuities. This mask is then combined with a mask created from a high-pass filter applied in the Fourier domain to exclude any slowly modulating frequencies. Results are reported visually, but appear to achieve a sensitivity of 50% with a specificity of 100%. Di Leo et. al. [31] extend this method and compute features over the 'holes' of the pigment network. A decision tree is learned in order to classify future images and an accuracy of 71.9% is achieved. Shrestha et. al. [98] begin with a set of 106 images where the location of the atypical pigment network (APN) has been manually segmented. If no APN is present, then the location of the most 'irregular texture' is manually selected. They then compute several texture metrics over these areas (energy, entropy, etc.) and employ various classifiers to label unseen images. They report accuracies of approximately 95%.

Although these studies have certainly made significant contributions, there has yet to be a comprehensive analysis of pigment network detection on a large number of dermoscopic images under 'real-world' conditions. All work to date has either: 1) not reported quantitative validation [36, 34]; 2) validated against a small ($n < 100$) number of images[17]; 3) only considered or reported results for the 2-class problem (e.g. *Absent*/*Present* rather than *Absent*/*Typical*/*Atypical*)[8, 17, 31, 98]; 4) not explicitly identified the location of the network [8]; or 5) has made use of unrealistic exclusion criteria and other manual interventions [98].

3.3.2 Automated Detection of Streaks

Even though the presence of irregular streaks is highly suggestive for malignancy of a lesion, the modeling, detection and analysis of streak lines and starburst patterns are largely omitted from literature, and it has very rarely been used for automated skin lesion diagnosis. Streaks on dermoscopy images usually are difficult to detect since they are not perfect linear structures, but often fuzzy and low-contrast oriented intensities. Furthermore, streaks may have unpredictable spatial distribution (partial pattern) with just a few streak lines in a small region of a lesion. Therefore, it is not easy to detect them using general oriented pattern analysis. The automatic detection of streaks has only recently been investigated [16, 36, 77].

Betta et al. [16] developed a method in which streaks were detected by simultaneously looking for occurrence of finger-like tracks along the contour of a lesion, and brown pigmentation for the corresponding region. They divide an image into 16 sub-images. For each sub-image they compute the irregularity of the lesion border and also the hue component of the original color image in the HSV color space. The final diagnostic decision is made by a simple threshold on these computed values.

Also in a recent work, Mirzaalian et al. [77] have used a machine-learning approach for classifying streaks in dermoscopic images. Although the methodology is interesting, it has been tested on only a small number (99) of dermoscopic images with wide exclusion criteria. It is not clear how the method would generalize to all conditions of dermoscopic images captured in a dermatologist clinic.

Fleming et al. [36] also considered the streak detection problem, however they did not provide a concrete solution. They argued that the presence and absence of radial streaming and pseudopods and their characteristics could be tested from a skeleton of the pigment network. However, details of the method were not reported. It is not clear how to find streaks from a lesion without a pigment network nor how to separate streaks from other dermoscopic structure.

3.4 Summary

In this chapter, we performed a literature review on the published approaches for pre-processing for enhancement and removal of artifacts on dermoscopy images, segmenting the lesion from the normal skin and finding dermoscopy structures such as the pigment network and streaks.

Chapter 4

Skin Lesion Segmentation Using Automated Random Walker

The Random Walker (RW) algorithm[45] is a general purpose interactive multi-label segmentation technique where a user labels the image with 'seed points' which denote the ground truth label for that pixel. Then, for an arbitrary pixel, the probability of a random walker reaching a seed of a specific label (before reaching seeds of any other label) is computed. However, the RW algorithm is sensitive to the exact placement of seeds and to the number of seeds placed [46]. While the RW algorithm is fast, intuitive and robust, it has been determined that a large number of seed points (up to 50% of the image) is required to reproduce a segmentation with only minor differences[46].

We have adopted the RW method described above into a novel framework, to automatically segment skin lesions from dermoscopic images.

4.1 Method

In this chapter we present an approach to leverage the advantages of RW for automatic skin lesion segmentation. We initialize the RW algorithm automatically with seed points generated by 'learning' (by means of a training set) the difference between the properties of 'skin lesion pixels' and 'healthy skin pixels'.

4.1.1 Supervised Probabilistic Segmentation

We begin with a set of 120 expertly segmented dermoscopic images taken from an atlas [10][100]. Each pixel is assigned either the label 'inside' (l_1) or 'outside' (l_2) based on the ground truth segmentation. In this stage we aim to learn the difference between these two groups. Images are converted to L*a*b* space, and each channel is filtered with a set of Gaussian and Laplacian of Gaussian filters. Let m denote the number of filters employed. Pixels are then represented as a $1 \times 3m$ vector since each filter is applied to each of the 3 image channels. Linear Discriminant Analysis (LDA)[35] is then used to determine the linear combination of filters that best discriminate 'inside' and 'outside' pixels. LDA is similar to Principal Component Analysis (PCA), but where PCA is an *unsupervised* technique that reduces dimensionality while maintaining variance, LDA is a *supervised* technique that reduces dimensionality while maintaining class separability. This is achieved through an eigenvalue decomposition of an $3m \times 3m$ scatter matrix, which represents the separability of the classes with respect to each filter. Since this is a 2-class problem, we consider only the principle eigenvector. This eigenvector results in a linear combination of the filtersets for each image channel. Since the filterset employed is a series of low-pass (Gaussian) and high-pass (Laplacian of Gaussian) filters, the resulting 'eigenfilters' can be interpreted as either a high, low, or multiple-band-pass filters. This filter bank includes five Gaussian and five Laplacian of Gaussian filters applied to the three channels of the L*a*b* space, that results 30 filter responses in total. We are therefore not only learning the colour difference between these two groups of pixels, but also the difference in the spatial variation of colors. This process is illustrated in Figure 4.1.

Next, the response of the pixel groups ('inside' and 'outside') along this eigenvector are modeled as Gaussian distributions

$$P(p|l_i) = \frac{1}{\sigma\sqrt{2\pi}} \exp\left(-\frac{(x-\mu)^2}{2\sigma^2}\right) \tag{4.1}$$

We create probability maps for unseen images by filtering the image with the resulting eigenfilters from LDA, and for each pixel p, assigning it a normalized probability that the pixel is inside the lesion

$$P = \frac{P(p|l_1)}{P(p|l_1) + P(p|l_2)} \tag{4.2}$$

The creation of a probability map is illustrated in Figure 4.2

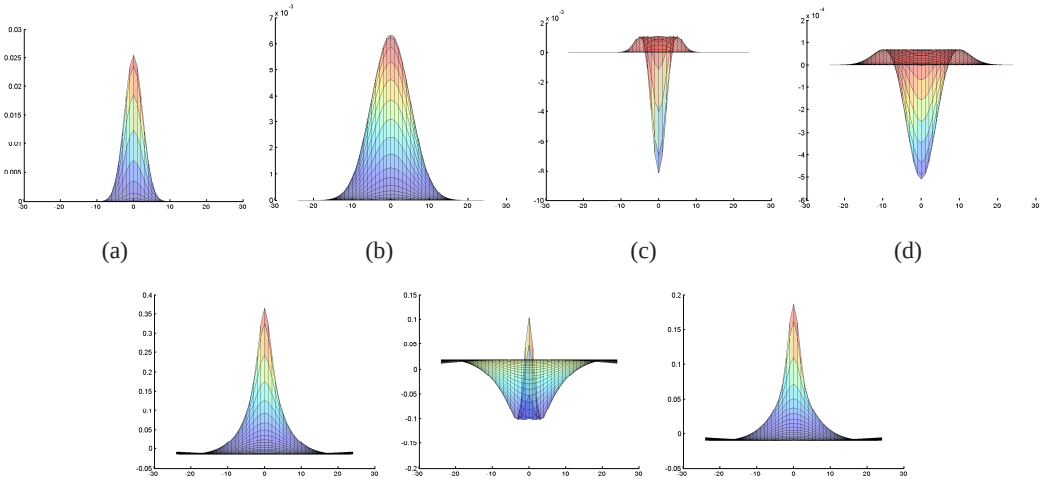

(a) (b) (c) (d)

(e) (f) (g)

Figure 4.1: Learning the difference between pixels inside and outside the segmentation. a)-d): Some filters from the filterset applied to each channel of each image. The filterset consists of Gaussian filters (a,b) and Laplacian of Gaussian filters (c,d) and the 'eigenfilters' as a result of LDA for the L*, a* and b* channels respectively (e,f,g).

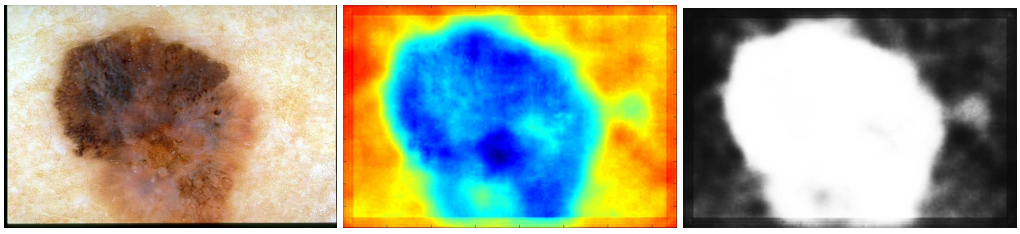

(a) (b) (c)

Figure 4.2: The creation of a supervised probabilistic segmentation. a) The original dermoscopic image b) The image's response to the 'eigenfilter' from Figure 4.1(c) The resulting probability map by applying equation 2. Note the high response to the photodamaged skin to the right of the lesion. This is due to the fact that this pattern (known as a *pigment network*) usually occurs within lesions.

4.1.2 Initializing the Random Walker Algorithm

The original RW algorithm is an interactive segmentation which requires the user to place seed points. In our proposed automatic RW approach, there is no user interaction and the object and the background seeds are automatically determined from the probability map generated in section 4.1.1. To generate seed points, two thresholds must be determined. Let T_S represent the skin threshold and T_L represent the lesion threshold. Once these thresholds are determined, an arbitrary number of seeds can be automatically generated as long as the thresholding constraints are satisfied. Let $P(p)$ represent the probability a pixel p is a part of the lesion, as determined by the probability map. A pixel is a candidate for a background seed if $P(p) < T_S$. Similarly, a pixel is a candidate for an object seed if $P(p) > T_L$.

To determine T_S and T_L, we analyze the histogram of the probability map (shown in Figure 4.3(b),(f)). We fit a Gaussian Mixture Model to the histogram and extract the dominant Gaussians that represent the skin and lesion [56]. Let μ_S and μ_L represent the means of the 'skin' and 'lesion' Gaussians respectively. Similarly, let σ_S and σ_L represent the variances. Thresholds are then determined by:

$$T_S = \mu_S + 3\sigma_S \tag{4.3}$$

$$T_L = \mu_L - 3\sigma_L \tag{4.4}$$

Now, let $F(x)$ represent the cumulative histogram of the probability map. We then define two metrics α_H and β_H, using the subscript H ('histogram') to differentiate from the β parameter of the RW algorithm:

$$\alpha_H = \frac{F(T_L) - F(T_S)}{F(T_S)} \tag{4.5}$$

$$\beta_H = \frac{F(T_L) - F(T_S)}{F(1) - F(T_L)} \tag{4.6}$$

Low values for both α_H and β_H imply an easy to segment, high contrast image, as shown in Figure 4.3(a)-(d). The area shaded red in Figure 4.3(b) denotes the amount of pixels which a label cannot be determined with certainty.

If however, either α_H, β_H or both are above a certain threshold, then the contrast between the lesion and skin is poor, and the segmentation is more difficult. Empirically, this threshold has been defined as 2.0. If α is above 2.0 then we define a new skin threshold T'_S as the median of the

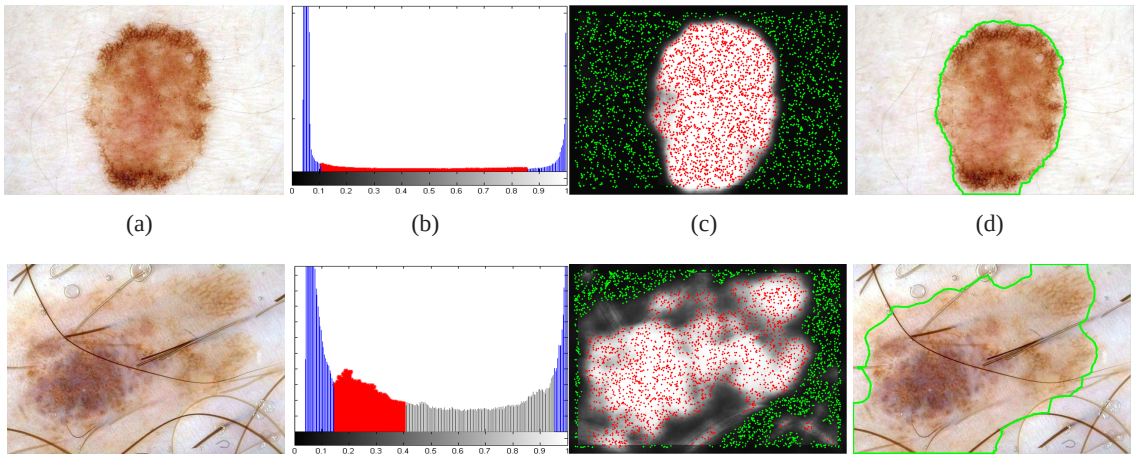

(a) (b) (c) (d)

(e) (f) (g) (h)

Figure 4.3: Automatically initializing the RW algorithm. First row: A high contrast, easy to segment image. a) The initial image. b) The histogram of the image's probability map as generated by section 4.1.1. The blue area denotes candidate seed pixels ($\alpha_H = 1.27, \beta_H = 1.74, T_S = 0.10, T_L = 0.85$). c) Seed pixels randomly selected. d) The resulting segmentation. Second row: A difficult low-contrast lesion with occluding hair. The original parameters ($\alpha_H = 0.77, \beta_H = 7.88, T_S = 0.18, T_L = 0.97$) indicate its difficulty since, $\beta_H > 2.0$. T'_L is therefore set to 0.42 (reducing the uncertainty area to the red shaded region)

uncertainty range (the range between T_S and T_L). Similarly, if β is above 2.0 we define T'_L as the median of the uncertainty range. If both α and β are above 2.0, we take the larger value to determine which threshold to shift. This threshold adaptation is illustrated in Figure 4.3(e)-(h). Initially α_H and β_H are computed in Figure 4.3(e). The amount of uncertain pixels is large (grey and red shaded are) which is reflected in the high value $\beta_H = 7.88$. Since $\beta_H > 2.00$, we define $T'_L = 0.42$, which reduces the uncertain region (red) considerably.

After determining the thresholds for the skin (T_S or T'_S) and the lesion (T_L or T'_L) pixels, seed points can now be chosen according to these thresholding constraints. We randomly choose only 3% of pixels as seeds. Since spatial filtering methods are inaccurate near image borders (as can be seen in Figure 4.2(b) we impose an additional constraint and do not consider pixels in proximity to the image border as seed point candidates.

After placing seeds in the areas of high certainty, RW segments the image. RW gracefully handles the uncertain area between the skin and lesion borders where there is not enough accurate information from the probability map. We initialize the RW graph edge weights using a Gaussian

function of the image intensity as Grady does[45]. The Gaussian width in this function, which we denote as β_{RW}, is a free parameter that determines the degree to which two intensities are considered similar. Throughout this experiment, this parameter has been fixed at 30. Finally, after applying the RW algorithm, the segmentations undergo morphological post-processing to fill holes and break isthmuses.

4.2 Results

We tested our method on a dataset of images taken from [10] and [100]. We begin by selecting 100 images that pose a challenge to segmentation methods, and call this imageset 'challenging'. These represent images that are often excluded from other studies[22]. An image is considered challenging if one or more of the following conditions is met: 1) the contrast between the skin and lesion is low, 2) there is significant occlusion by either oil or hair, 3) the entire lesion is not visible, 4) the lesion contains variegated colors or 5) the lesion border is not clearly defined. Next, we select 20 images that do not meet any of the above conditions, and call this imageset 'simple'. We merge these two imagesets, calling the resulting imageset 'whole'. Finally, we create an imageset to measure the intra-observer agreement of our expert. We randomly select 10 images from the 'challenging' imageset. These images undergo a random rotation of 90, 180 or 270 degrees, and some are randomly inverted along the X and/or Y axes. This is done to reduce the likelihood that the dermatologist would recognize the duplicate image while performing the segmentation task. We call this imageset 'intra'.

Probability maps for all images are generated as described in section 4.1.1 using ten-fold cross validation. Seeds are placed automatically as described in section 4.1.2. The results are summarized in Table 4.1. We also compare our results to the Otsu thresholding method[83] on probability maps and measure the intra-observer variability of the expert. Segmentations obtained from our modified random walker algorithm, the Otsu method and the dermatologist are denoted as 'MRW', 'Otsu' and 'Derm' respectively. For all comparisons we compute precision, recall, F-measure ($2\times(precision\times recall)/(precision+recall)$), and border error [51] which is also called XOR measure and it is defined as

$$BE = (automaticborder \otimes manualborder)/manualborder$$

.

As can be seen in Table 4.1, while the Otsu method consistently achieves a higher precision,

Comparison	Imageset	n	Precision	Recall	F-measure	Mean BE	Std BE
MRW vs. Derm	simple	20	0.96	0.95	0.95	0.079	0.024
MRW vs. Derm	challenging	100	0.83	0.90	0.85	0.31	0.19
MRW vs. Derm	whole	120	0.87	0.92	0.88	0.24	0.18
Otsu vs. Derm	simple	20	0.99	0.86	0.91	0.15	0.083
Otsu vs. Derm	challenging	100	0.88	0.68	0.71	0.44	0.40
Otsu vs. Derm	whole	120	0.91	0.74	0.78	0.34	0.36
Derm vs. Derm	intra	10	0.95	0.91	0.93	0.085	0.036

Table 4.1: Comparing the results of our modified random walker segmentation algorithm (MRW) to that of Otsu's thresholding method[83] (Otsu), and a dermatologist's manual segmentation which acts as ground truth (Derm). Comparisons are performed over simple and challenging imagesets taken from [10] and [100]. See Section 4.2 for a description of these imagesets.

its recall is much worse. This implies that the Otsu method consistently underestimates the lesion border, labeling many pixels as 'skin' that ought to be labeled as 'lesion'. When examining the more comprehensive metrics such as F-measure or border error, it is apparent that our modified random walker outperforms Otsu's method. The poorer F-measure and border error results for the Otsu method on the challenging imagest indicates how very difficult that imageset is; also born out by the results of the intra-observer agreement of the expert dermatologist on the 'intra' imageset.

Figure 4.4 shows sample results of the segmentations obtained from our method (denoted in black) as well as the ground truth segmentation (denoted in green) for a variety of lesions, including several difficult lesions.

4.3 Contribution

Results of our method were presented in Medical Image Computing and Computer Assisted Interventions (MICCAI) in 2009 [110]. As the co-first author of this paper, my contribution was the design and implementation of the study in collaboration with Paul Wighton. He worked on the supervised probabilistic learning section for creating probability maps to be used in segmentation using the RW method and I was in charge of designing the automated segmentation method based on RW, performing experiments and analyzing the results. We wrote the paper together.

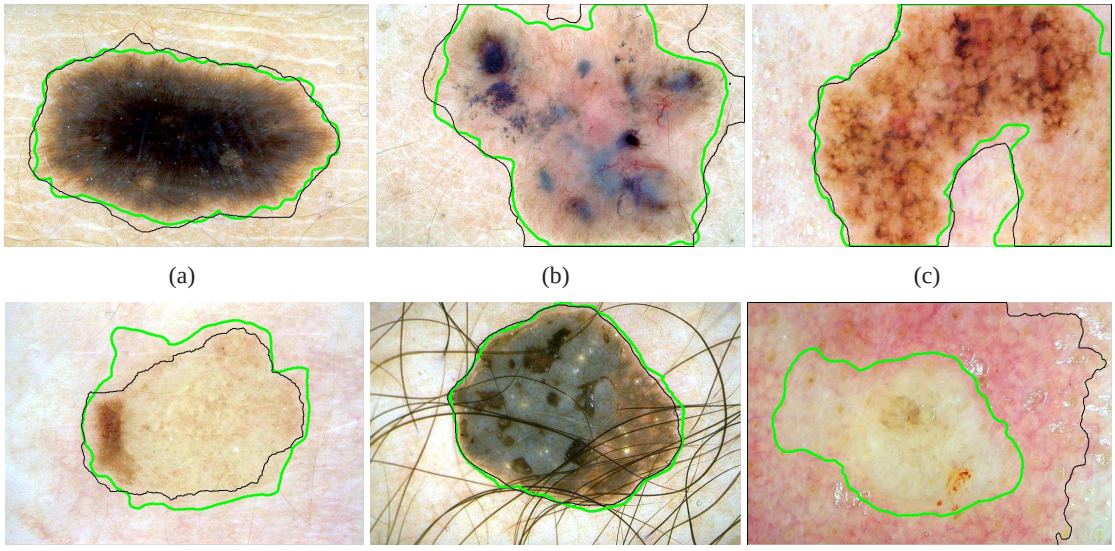

(a) (b) (c)

(d) (e) (f)

Figure 4.4: Sample segmentation results for our method (denoted in black) compared to ground truth (denoted in green). a) A typical, easy to segment lesion. b) A lesion with variegated colours. c) An example of the entire lesion not being visible. Also, the lesion border is unclear in the bottom right hand side. d) A low contrast lesion. e) A lesion occluded significantly by hair. f) A difficult case where our method fails.

4.4 Conclusion

We have developed a fully automatic method for segmenting unseen skin lesions by leveraging knowledge extracted from expert ground truth, and the random walker algorithm. Our method uses colour as well as texture to perform the segmentation, and adapts itself to handle difficult, low-contrast images. Clinically, this is the first step towards an automated skin lesion diagnosis system.

Chapter 5

Pigment Network Detection and Analysis

In this chapter, we address the problem of how to determine the absence or presence of pigment networks in a given dermoscopic image. As we described in Chapter 2, a pigment network can be classified as either *Typical* or *Atypical*, where the definition of a *Typical* pigment network is "a light-to-dark-brown network with small, uniformly spaced network holes and thin network lines distributed more or less regularly throughout the lesion and usually thinning out at the periphery" [11]. For an *Atypical* pigment network, we use the definition "a black, brown or gray network with irregular holes and thick lines" [11]. The goal is to automatically classify a given image to one of three classes: *Absent*, *Typical*, or *Atypical*. Figure 5.1 exemplifies these 3 classes.

We use these definitions to subdivide the structure into the darker mesh of the pigment network (which we refer to as the 'net') and the lighter colored areas the net surrounds (which we refer to as the 'holes'). After identifying these substructures we use the definitions above to derive several structural, geometric, chromatic and textural features suitable for classification. The result is a robust, reliable, automated method for identifying and classifying the structure pigment network.

Figure 5.2 illustrates an overview of our approach to irregular pigment network detection. After pre-processing, we find the 'hole mask' indicating the pixels belonging to the holes of the pigment network. Next, a 'net mask' is created, indicating the pixels belonging to the net of the pigment network. We then use these masks to compute a variety of features including structural (which characterizes shape), geometric (which characterizes distribution and uniformity), chromatic and textural features. These features are fed into a classifier to classify unseen images into 3 classes of *Absent*, *Typical* and *Atypical*. The major modules in Figure 5.2 are explained in the following

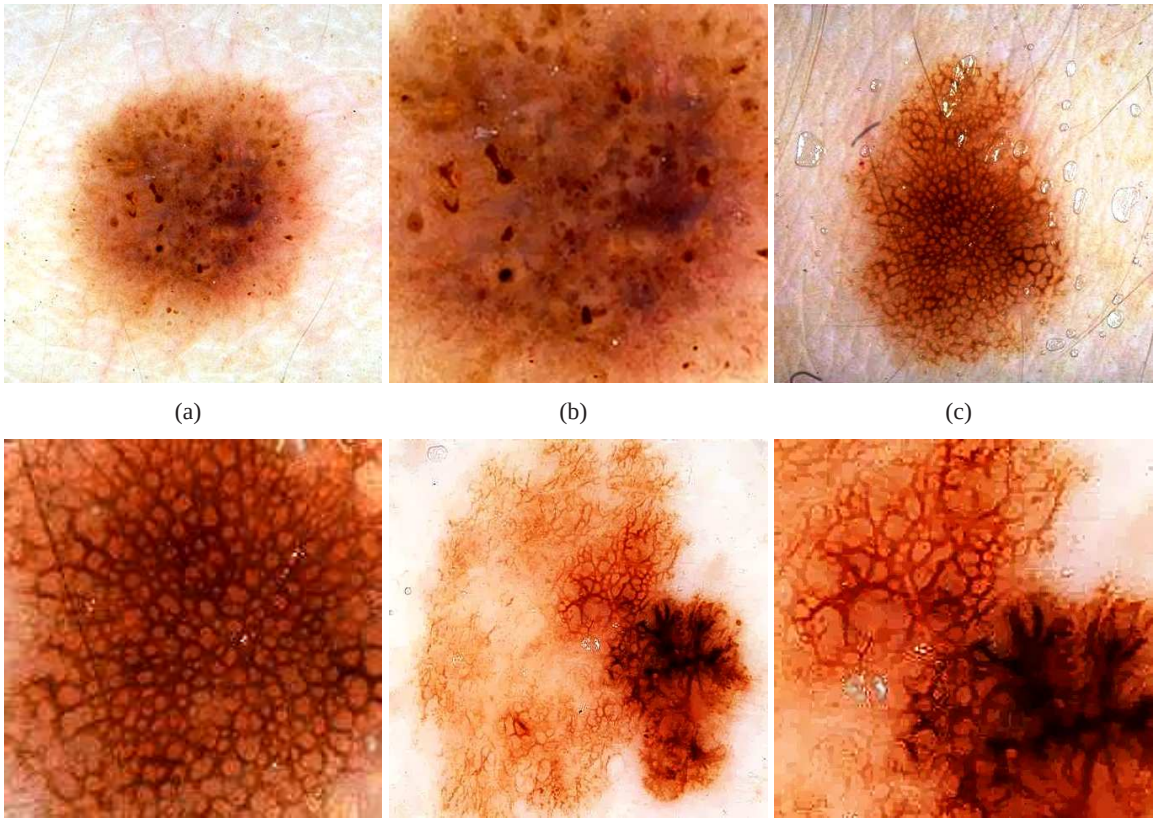

(a) (b) (c)

(d) (e) (f)

Figure 5.1: The 3 classes of the dermoscopic structure pigment network: a-b) *Absent*; c-d) *Typical*; and e-f) *Atypical*. b),d),f) are magnifications of a),c),e) respectively.

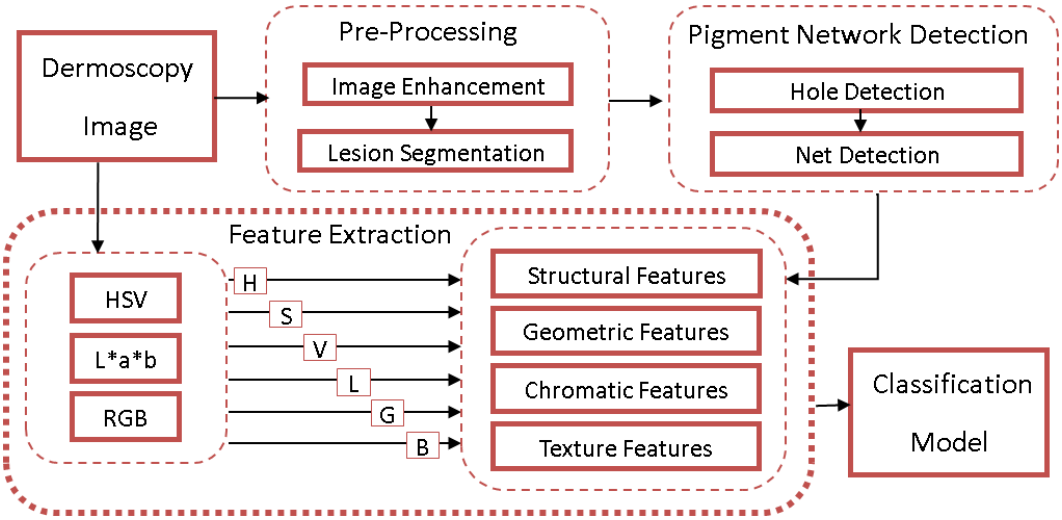

Figure 5.2: Overview of construction of our classification model

sub-sections.

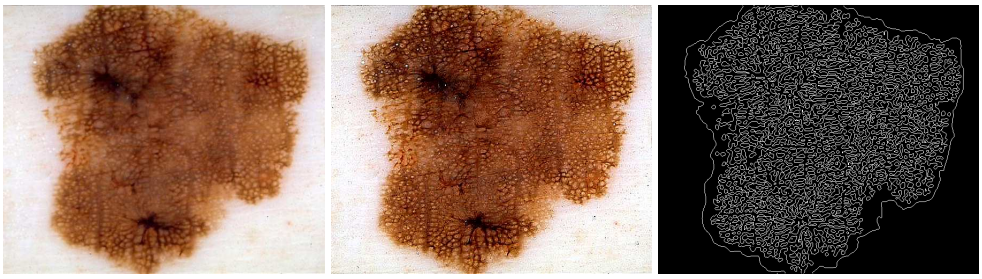

(a) (b) (c)

Figure 5.3: a) A given skin lesion image. b) Sharpened image. c) Result of the edge detection after segmenting the lesion.

5.1 Pre-processing

In order to prevent unnecessary analysis of the pixels belonging to the skin, the lesion is first segmented. Either manual segmentation or our automatic segmentation method [110] was used. Next the image is sharpened using the MATLAB Image Processing Tool Box function *Unsharp* mask, one of the most popular tools for image sharpening [86]. A two-dimensional high-pass filter is created using Equation 5.1. This high-pass filter sharpens the image by removing the low frequency noise.

We use the default parameters of MATLAB in our experiments ($\alpha = 3$). Figure 5.3-b shows the result of the sharpening step.

$$SharpeningFilter(\alpha) = (\frac{1}{\alpha+1}) \begin{vmatrix} -\alpha & \alpha-1 & -\alpha \\ \alpha-1 & \alpha+5 & \alpha-1 \\ -\alpha & \alpha-1 & -\alpha \end{vmatrix}. \quad (5.1)$$

To investigate structures of the skin texture, it was necessary to reduce the color images to a single plane before applying our algorithm. Various color transforms (NTSC, L*a*b, Red, Green, and Blue channels separately, Gray(intensity image), etc) were investigated for this purpose. After the training and validation step, we selected the green channel as the luminance image. Results of the different color transformations are reported in the result section of this chapter.

5.2 Hole detection

As discussed previously, a pigment network is composed of holes and nets. We first describe the detection of the holes. Figure 5.4 shows steps of our novel graph-based approach to hole detection. After the pre-processing step described above, sharp changes of intensity are detected using the Laplacian of Gaussian (LoG) filter. The result of this edge detection step is a binary image which is subsequently converted into a graph to find holes or cyclic structures of the lesion. After finding loops or cyclic subgraphs of the graph, noise or undesired cycles are removed and a graph of the pigment network is created using the extracted cyclic structures. According to the density of the pigment network graph, the given image can be classified into *Present* or *Absent* classes, but for irregularity analysis we also need to extract more features and characteristics of the net of the network.

We used the LoG filter to detect the sharp changes of intensity along the edge of the holes inside the segmented lesion. Because of the inherent properties of the filter, it can detect the “light-dark-light” changes of the intensity well. Therefore it is good choice for blob detection and results in closed contours. The detection criterion of the edge of a hole is set to the zero crossing in the second derivative with the corresponding large peak in the first derivative. We follow the MATLAB implementation of the LoG edge detection which looks for zero crossings and their transposes. All zeros are kept and edges lie on the zero points. If there is no zero, an edge point is arbitrarily chosen

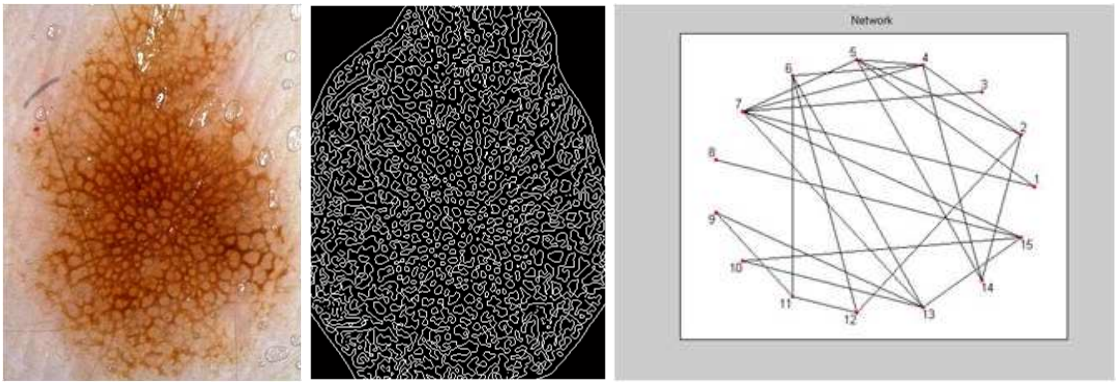

(a) Original image (b) LoG response (c) Image to graph conversion

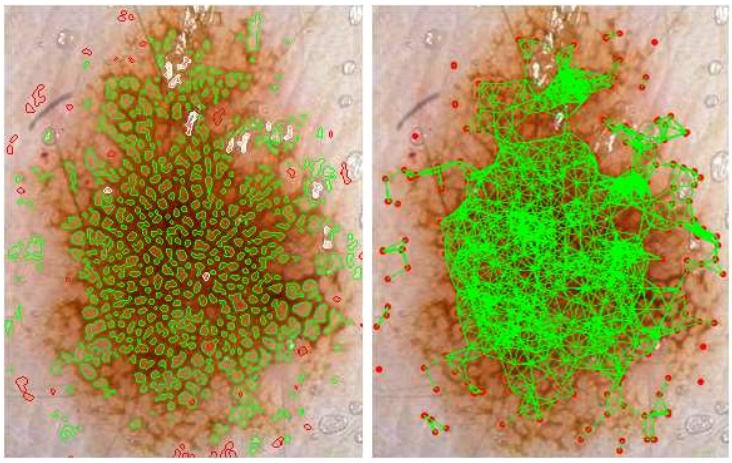

(d) Cyclic subgraphs (e) Graph of holes

Figure 5.4: Steps of the proposed algorithm for hole detection

as a negative second derivative point. Therefore when all ”zero” responses of the filtered image are selected, the output image includes all closed contours of the zero crossing locations inside a segmented lesion. An example of the edge detection step is shown in Figure 5.3-c and in Figure 5.4-b. This black and white image captures the potential holes of the pigment network.

Now, we consider the steps necessary to extract the holes accurately. In previous works [36, 17, 48], these structures usually are found by morphologic techniques and a sequence of closing and opening functions applied to the black and white image. We did not use this approach because using morphologic techniques is error-prone in detecting the round shaped structures. Instead, the binary image is converted to a graph (G) using 8-connected neighbors. Each pixel in the connected component is a node of G and each node has a unique label according to its coordinate.

To find round texture features (i.e. holes), all cyclic subgraphs of G are detected using the Iterative Loop Counting Algorithm (ILCA) [62]. This algorithm transforms the network into a tree and does a depth first search on the tree for loops.

After finding cyclic subgraphs which may represent the holes of a pigment network, these subgraphs were filtered and noise or wrongly detected structures (globules and dots) were removed according to parameters learned in a training and validation step.

Pigment network holes should have higher mean intensity than the border; on the other hand the reverse is true for globules and brown dots. Therefore we thresholded the difference between the average intensity of inner pixels and the average intensity of the border to discriminate globules from holes of the pigment network. First, we remove all detected cycles which are shorter than 7 pixels and longer than 150 pixels. These parameters can be set for a given data set according to the scale, magnification and resolution of images. The atlas image set [10] used in the experiment does not provide precise information about the resolution and magnification of the image set which is used in our experiment. Furthermore, we are uncertain if the resolution and magnification is the same for all images of the atlas. Therefore, to play safe, we set a wide range (7 to 150) to find as many holes of pigment networks as possible. In order to belong to a pigment network, a detected cyclic subgraph should have a higher intensity on the area contained by the network structures (holes) than on the network itself (lines), but in globules and brown dots, the mean intensity of the area inside the structure is lower than the intensity of border pixels so we can discriminate them. We also have to deal with oil bubbles and white cysts and dots. These structures are similar to holes of the pigment network in terms of the mean intensity of the inside being lighter than the border area, but they are much brighter inside. So, if there is at least one pixel with high intensity (set to 0.8, on a scale of 0 to 1) in the inside area of a hole, it will be colored as white representing oil bubbles, white cysts or dots. Therefore, these wrongly detected round structures of brown dots and globules, white dots, white cysts and oil bubbles are removed from the rest of the analysis. We colored these noise structures with red and white in Figure 5.5. Thus, the multi-level thresholds, determined by the training step, are set up as:

$$Color = \begin{cases} Green & 0.01 < (I - B) < 0.1 \\ White & 0.1 < (I - B) \ \wedge \ \exists P_I > 0.8 \\ Red & Otherwise \end{cases} \tag{5.2}$$

where I is mean intensity of the inside area, B is the mean intensity of the border or outside area, and P_I is a pixel inside the hole. Figure 5.5 shows three examples of skin lesions with filtered cyclic

subgraphs overlaid. These structures can be used later for the analysis of globules and dots which are other important structures of the skin lesion texture.

In order to visualize the location of a pigment network based on the detected holes, we created a new higher-level graph G whose nodes are centers of the holes belonging to the pigment network (green colors). Nodes within a maximum distance threshold (MDT) are connected together. However, there is not a minimum node distance threshold. The value of the MDT is computed based on the average diameter of all holes in the image. Based on the pigment network definition, holes of a regular network are uniformly spaced. To consider this spatial arrangement, the MDT should be proportional to the size of holes and is defined as alpha (set to 3) times the average diameter of holes.

Figure 5.6 illustrates two examples of skin lesions with their graphs of holes overlaid in green. The first column shows a *Present* image and the second one shows an *Absent* image, both of which are classified correctly using the only the graph of the pigment network holes.

5.3 Net Detection

In order to identify the net of a pigment network, we apply the Laplacian of Gaussian (LoG) filter to the green channel of the image. The LoG filter identifies high frequency components of an image and therefore makes an ideal net detector. The major issue with applying this operator is that its response is strongly dependent on the relationship between the frequency of the structures and the size of the Gaussian kernel used. We used $\sigma = 0.15$, which is an appropriate value for images of the two atlases used in our experiment [10, 100], however it can be tuned for a given imageset according to scale and magnification. In our experiment, we observed that the average thickness of the pigment network is proportional to the average size of holes of the network. We therefore set the size of the LoG window size to half of the average hole size in the image. The average window size over all images of our data set is 11 pixels. We then threshold the filter response automatically, resulting in a 'net mask' which indicates which pixels belong to the net of the the pigment network. Furthermore, we skeletonize this mask, resulting in a 'skeleton mask'. Figure 5.7 illustrates the net extraction process.

Qualitative results of detecting pigment network 'net' and 'holes' ares illustrated in Figure 5.8.

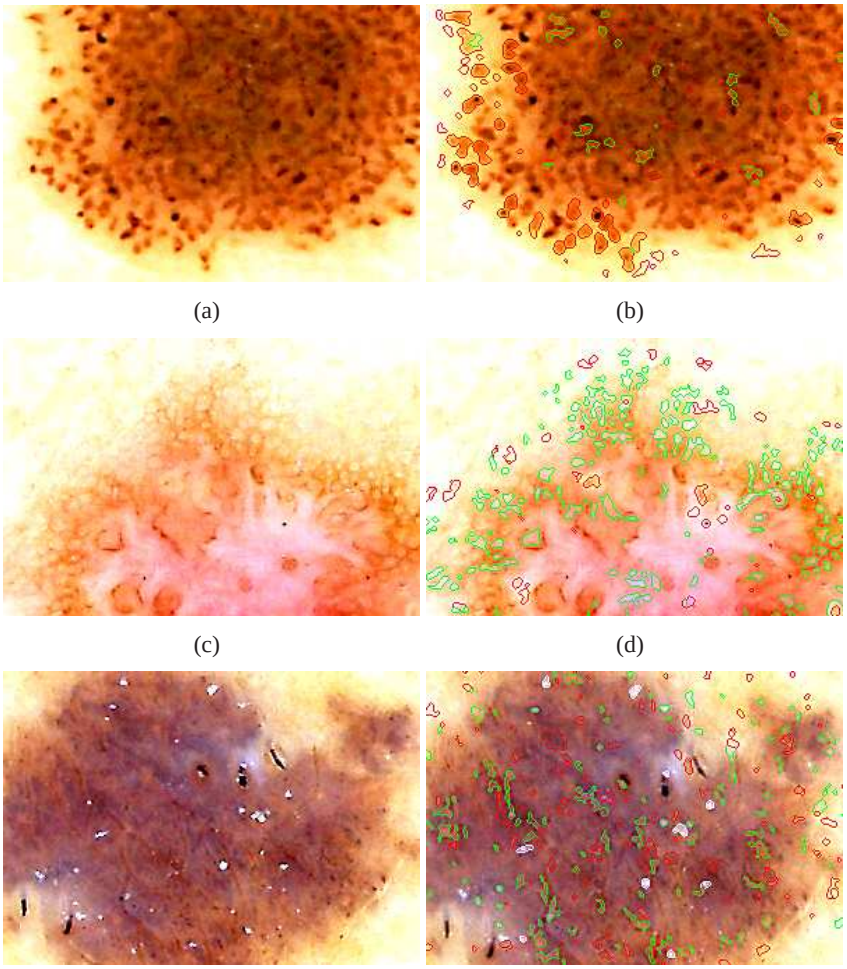

(a) (b)

(c) (d)

(e) (f)

Figure 5.5: Detected cyclic subgraphs are filtered based on their inside-outside intensity differences. (a), (c), and (e) show original skin lesions. (b), (d), (f) show green, red and white colors overlaid; The red colors mostly belong to globules and brown dots. White dots and oil bubbles are colored as white and holes of the pigment network are visualized as green.

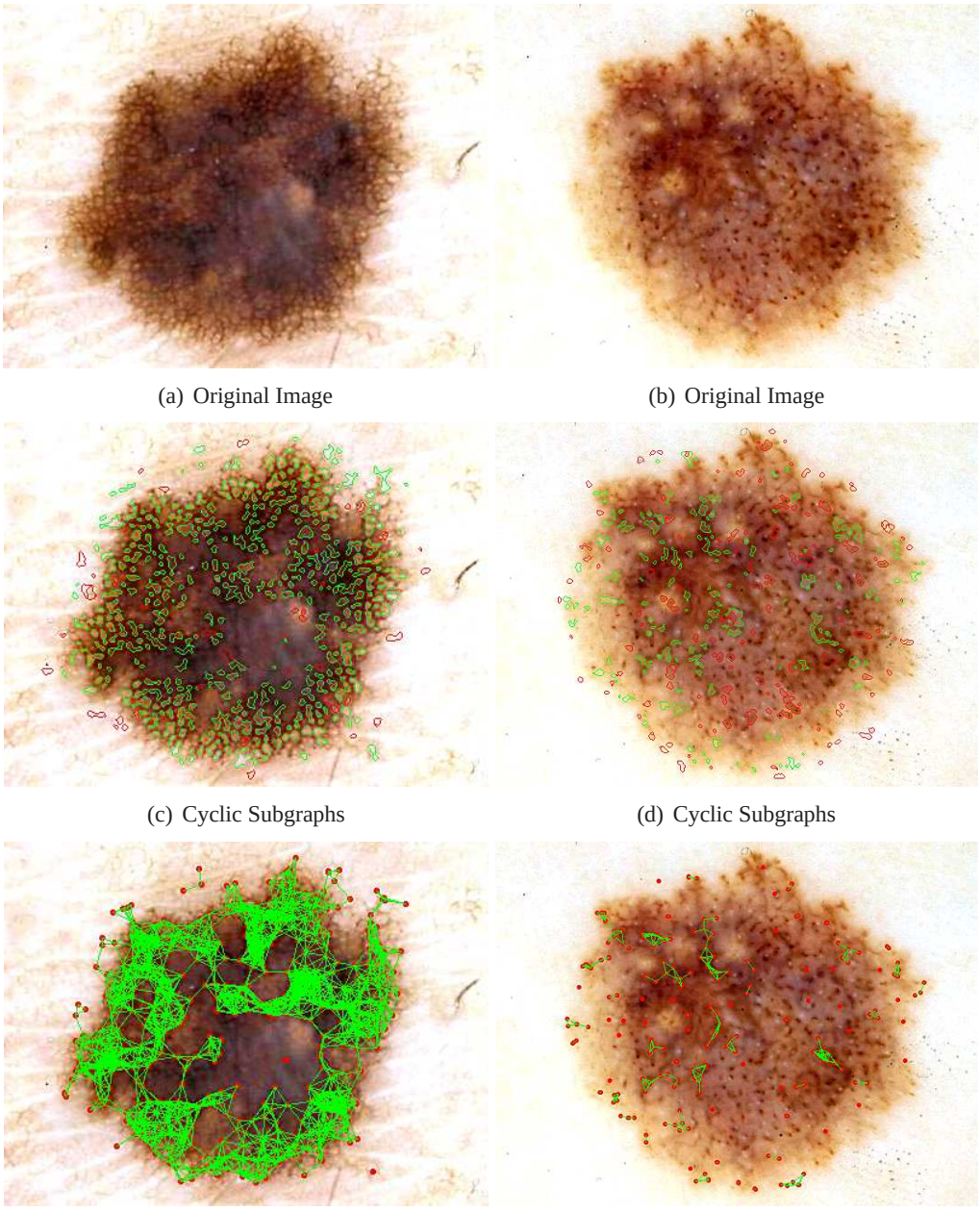

(a) Original Image (b) Original Image

(c) Cyclic Subgraphs (d) Cyclic Subgraphs

(e) *Present* (f) *Absent*

Figure 5.6: Results of applying our approach to two *Present* and *Absent* dermoscopic images; (a) and (b) are skin lesions, (c) and (d) show cyclic subgraphs, the green lines represent potential holes of the pigment network and red lines show holes that did not pass the test of belonging to the pigment network, and (e) and (f) visualize the pigment network over the image.

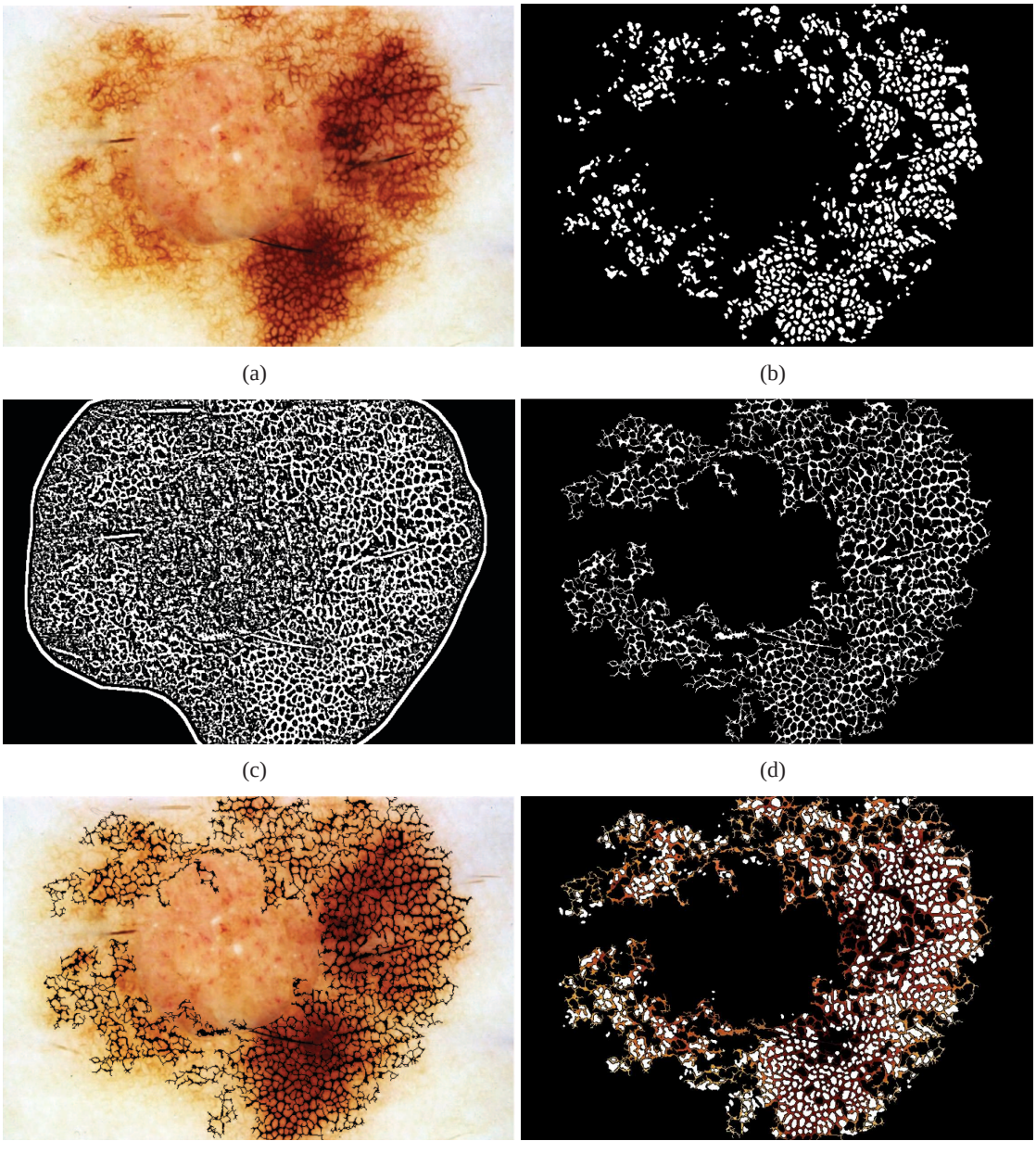

Figure 5.7: Net detection. a) A dermoscopic image, b) detected holes in the previous step, c) response of the LoG filter, d) the resulting 'net mask', e) the extracted net of the pigment network overlaid on the original image, and f) the segmented pigment network.

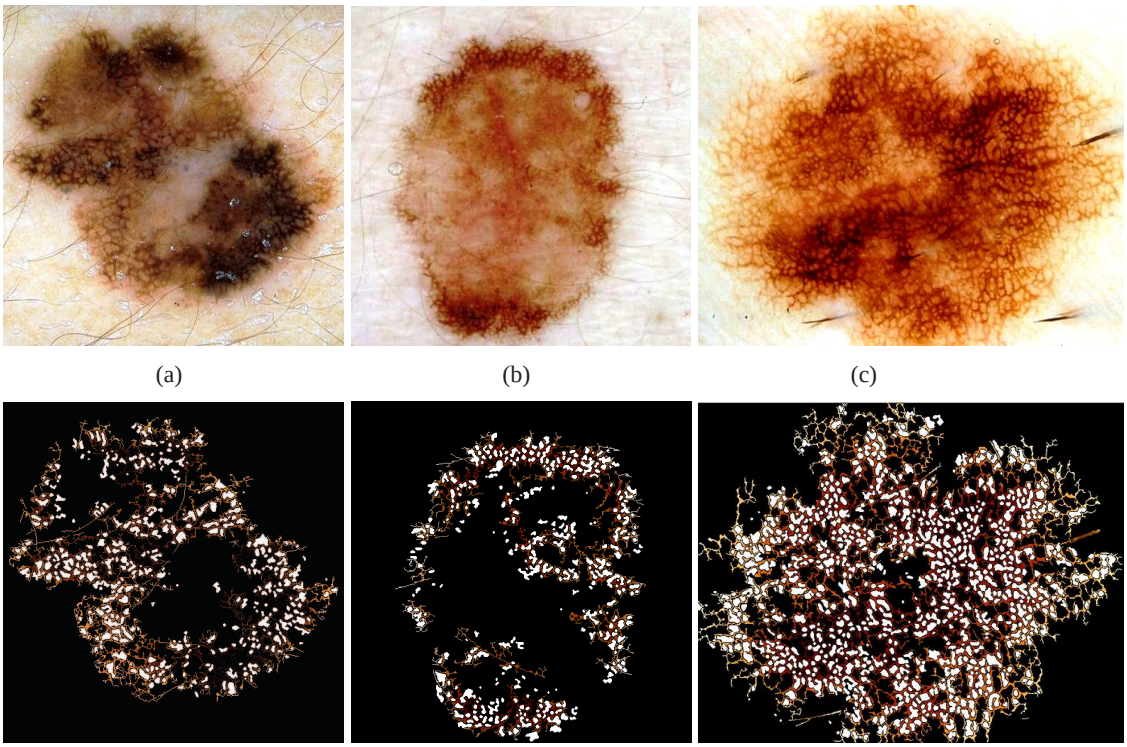

(a) (b) (c)

(d) (e) (f)

Figure 5.8: Three images of the image set: the top row shows the original images and the bottom row shows their corresponding pigment networks (brown) and holes (white).

5.4 Feature Extraction

Based on the definitions of *Typical* and *Atypical* pigment networks, we use the results of the hole and net detection to propose a set of features capable of discriminating among the 3 classes (*Absent*, *Typical* and *Atypical*). We propose a set of structural (shape), geometric (spatial) chromatic and textural features.

5.4.1 Structural Features (20 features):

Diagnostically important characteristics of a network include the thickness of the nets as well as the size of the holes.

For each spatially disjoint section of the net mask, we compute its size (number of pixels in the net mask) and length (number of pixels in the skeleton mask). Our features are then the mean, standard deviation and coefficient of variation ($mean/std$) of the sizes and lengths of the nets.

Thickness is also computed by measuring the distance from each pixel in the net mask to the closest pixel in the skeleton mask. The mean, standard deviation and ratio of thickness as well as a 6-bin thickness histogram are also included as features. For each spatially disjoint section of the hole mask, we compute the size (number of pixels) and include as features the mean, standard deviation and coefficient of variation ($mean/std$) of hole size as well as the total number of holes.

We also include the ratio of the network size (number of pixels in the net and hole masks) to the lesion size (number of pixels in the segmentation mask).

5.4.2 Geometric Features (2 features)

We have defined a new feature called 'Density Ratio' of holes which is useful in discriminating between the absence and presence of a pigment network. This feature is defined as

$$Density = \frac{|E|}{|V| * \log(LesionSize)} \tag{5.3}$$

where $|E|$ is the number of edges in the graph G, $|V|$ is the number of nodes of the graph and *LesionSize* is the size of the area of the image within the lesion boundary, being investigated for finding the pigment network. The rationale of Eq. 5.3 is that a bigger $|E|$ means that more holes are closer than the MDT. Also, having a smaller $|V|$ for a fixed $|E|$ means that nodes or holes are uniformly spaced close to each other and the graph of the pigment network is dense. Therefore, based on the pigment network definition, having a high 'Density Ratio' is a requirement for being *Present*. *LesionSize* is used to normalize the ratio $|E|/|V|$. For example, a fixed number of vertices and edges in a small lesion is more likely representing *Present* than in a relatively big lesion. However, since there is not a linear relationship between the size of a lesion and the probability of being *Present* or *Absent*, we found experimentally that the logarithm of *LesionSize* is more appropriate.

Clinically, there is an emphasis on the 'uniformity' of the network in order to differentiate between *Typical* and *Atypical*. In addition to the 'Density Ratio' of holes as a feature, we included another feature, which is the number of edges in the graph G.

5.4.3 Chromatic Features (37 features)

Color also plays a crucial role in clinical diagnosis. We therefore convert the image to HSV colour space [97] and compute features over each channel as well as the original green channel of the image. In each channel, for the hole, net and lesion masks respectively we compute the mean, standard deviation and coefficient of variation ($mean/std$) of the intensity values. Additionally,

(a) (b) (c)

Figure 5.9: Three difficult examples of our image set: a) A hairy image. b) An oily image. c) A low-contrast image.

we also propose a new chromatic feature called the 'atypicality measure' which is the sum of the intensity values over the green channel of the pixels in the net mask normalized by the number of the pixels.

5.4.4 Textural Features (10 features)

We use five of the classical statistical texture measures of Haralick et al. [52]: entropy, energy, contrast, correlation and homogeneity which are derived from a grey level co-occurrence matrix (GLCM). The GLCM is a tabulation of how often different combinations of pixel luminance values (gray levels) occur in a specific pixel pairing of an image. We construct 2 GLCMs (in the four directions of 0, 45, 90, 135 and within the distance of 4 pixels using 8 gray levels averaged to obtain a single GLCM) and extract the 5 texture metrics from each. The first GLCM is constructed over the entire lesion (using the pixels in the lesion mask) and the second is constructed over the pigment network (using the pixels in the net and hole masks).

5.5 Evaluation for *Absent*/*Present* classification using 'Density Ratio'

To measure the strength of our proposed feature, 'Density Ratio', we applied our method to a set of dermoscopic images taken from Argenziano et al.'s Interactive Atlas of Dermoscopy [10]. We tuned the parameters and thresholds of our proposed method according to a set of 100 images of size 768x512. Then we tested the method for another set of images (500 images) randomly selected from the atlas. We classified the unseen images by feeding the 'Density Ratio' into the SimpleLogistic [65] classifier implemented in Weka [43] (a general data mining tool developed by University of Waikato in New Zealand) which uses a powerful boosting algorithm, LogitBoost [37]. Boosting is a

method for combining the performance of many weak features to produce a powerful classifier [37]. SimpleLogistic fits logistic models by applying LogitBoost with simple regression functions as base learners. Some of these images were challenging due to acquisition parameters such as lighting and magnification, being partial (entire lesion was not visible), or due to the presence of an unreasonable amount of occlusion by either oil or hair. These challenging images are usually discarded from test sets in the previous work. However, these images were kept in our test set.

Table 5.1 shows the percentage of correct classifications (*Present* or *Absent*) for the 500 test images, using different color transformations. It is seen that the green channel gives the best classification. Comparing our results to Anantha et al.'s method [8] (achieving 80% accuracy), we achieved a better result, however the same gold standard is not used and the image sets are different. Therefore, a direct comparison is impossible due to different images and ground truths. Note that we deliberately created a difficult dataset by not excluding oily, hairy and low-contrast images. Figure 5.9 shows three difficult examples of our image set. Our method also locates the pigment network and provides a qualitative analysis which can be used for extraction of pigment network characteristics to discriminate typical pigment networks from atypical ones.

	R	G	B	YIQ	Gray	L*a*b
Correct Classification (Accuracy)	90.7	**94.3**	90.1	92.6	91.1	89.7

Table 5.1: Correct classification rates (Accuracy) of different colour transformations for N=500 images.

According to the results of the various color transformations, the green channel is the best one for the pigment network detection. Interestingly the Y channel of YIQ (the transformation used for NTSC systems) has the second best result. The Y channel transformation is defined as:

$$Y = 0.299R + 0.587G + 0.114B \tag{5.4}$$

where R, G, B are the red, green, and blue color components, respectively. To compute the luminance Y, the green channel has larger weight than the other channels so is the likely reason the Y channel works well. In the gray-scale experiment, the intensity image is calculated by $(R+G+B)/3$ and in the L* experiment, the L* component of the L*a*b space is used as the intensity image.

In some images, it is not easy to detect the pigment network even by experts. Figure 5.10(a) shows one of these challenging images taken from [11], where the expert dermatologists only had

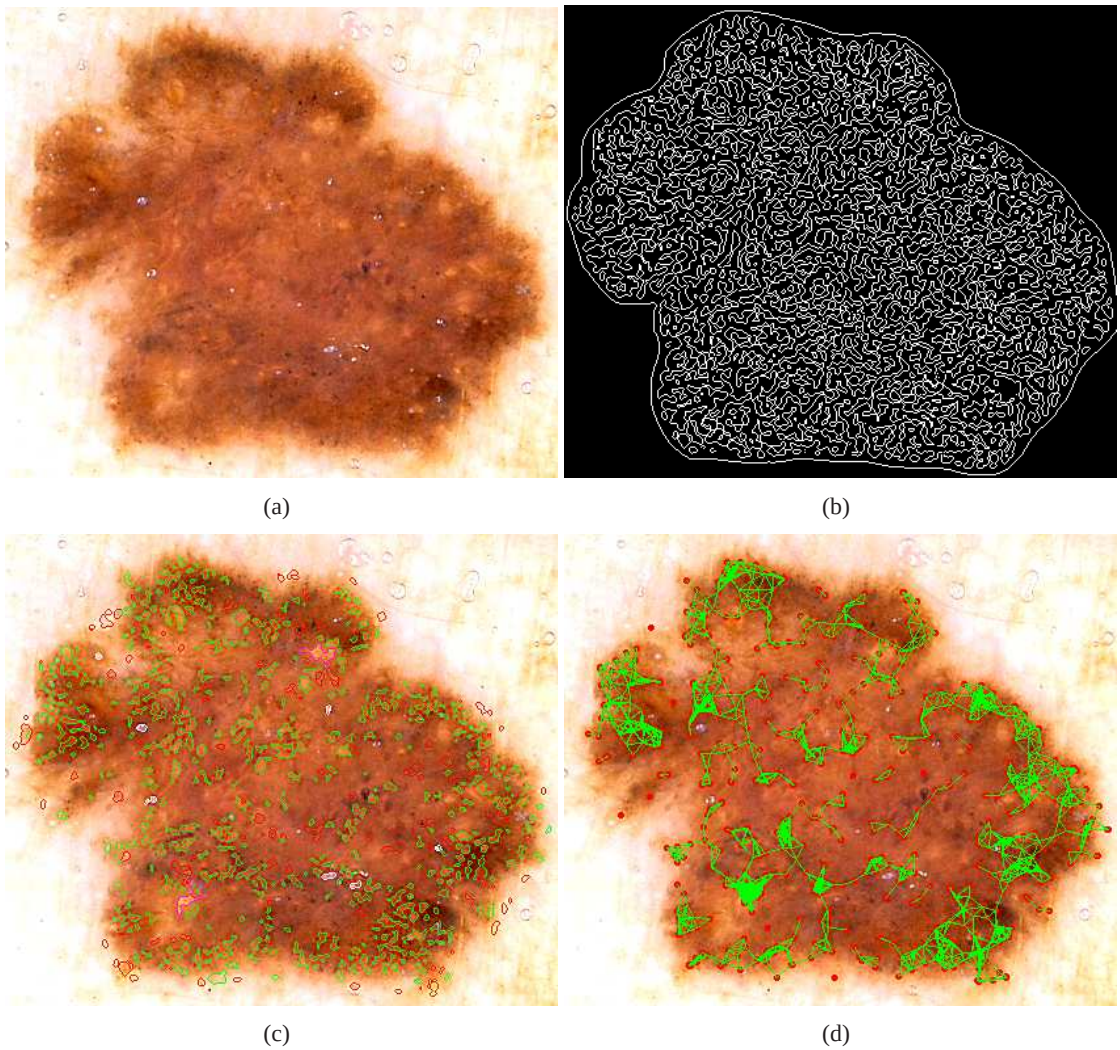

(a) (b)

(c) (d)

Figure 5.10: A challenging image with 51.5% inter-expert agreement favoring the *Present* diagnosis.

51.5% agreement among themselves, with a small majority favoring the *Present* diagnosis. Our algorithm can assist dermatologists to make their diagnosis by visualizing the pigment network (if any). This method may also be used for training purposes. Figure 5.10 illustrates the outcome of applying our method on the image, which classifies it as a *Present* pigment network.

5.6 Evaluation for *Absent*/*Typical*/*Atypical* Classification

In another experiment, we evaluated the whole feature set (69 features) on the three class problem using the SimpleLogistic classifier.

Absent-Typical-Atypical Classification					
	Precision	Recall	F-measure	Accuracy	N
Absent	0.905	0.950	0.927	-	161
Typical	0.787	0.792	0.790	-	154
Atypical	0.750	0.694	0.721	-	121
Our Weighted Avg	**0.820**	**0.823**	**0.821**	**0.823**	436
Di Leo et al. [31]	0.709	0.711	0.709	0.719	436
Absent-Present Classification					
Absent	0.893	0.932	0.912	-	161
Present	0.959	0.935	0.947	-	275
Our Weighted Avg	**0.935**	**0.933**	**0.934**	**0.933**	436
Di Leo et al. [31]	0.875	0.876	0.875	0.876	436

Table 5.2: Comparing accuracy, precision, recall and f-measure of our proposed features with Di Leo et al.'s features [31] using the same set of 436 images.

Since we have not performed any artifact (hair and oil bubble) detection and removal algorithm, in this evaluation we excluded oily and hairy images and we applied the method described above to a set of 436 dermoscopic images taken from two atlases of dermoscopy [10, 100]. Among these images, a clean subset of 400 images, from the set of 600 images used in our *Absent/*Present evaluation from [10], is used. Each image is labeled as *Absent*, *Typical* or *Atypical*, representing the presence and the regularity of the pigment network. The other 36 images are from [100] and have been labeled by 40 experts, each one assigning a label of either *Absent*, *Typical* or *Atypical* to each image. Overall labels for these images are generated by majority voting. In total, our dataset consists of 436 images (161 *Absent*, 154 *Typical*, 121 *Atypical*). We compute results for both the 3-class (*Absent*, *Typical* or *Atypical*) and 2-class problems (*Absent*, *Present*). Ten-fold cross validation was used to

generate all results. Table 5.2 summarizes these results in terms of Precision (Positive Predictive value), Recall (True Positive Rate or Sensitivity), F-measure, and Accuracy. F-measure is a measure of a test's accuracy that considers both the Precision and the Recall of the test to compute the score where

$$\text{Precision} = \frac{TruePositive}{TruePositive + FalsePositive} \tag{5.5}$$

$$\text{Recall} = \frac{TruePositive}{TruePositive + FalseNegative} \tag{5.6}$$

$$\text{F-measure} = 2 \cdot \frac{\text{Precision} \cdot \text{Recall}}{\text{Precision} + \text{Recall}} \tag{5.7}$$

And Accuracy is computed as:

$$\text{Accuracy} = \frac{TruePositive + TrueNegative}{TruePositive + TrueNegative + FalsePositive + FalseNegative} \tag{5.8}$$

Comparing our results with the results generated by the others using different datasets is not possible, and the only work that we could reproduce is the method by Di Leo et al. [31] described in Chapter 3. For comparison, the feature set described in [31] was also implemented and results over our image sets are computed. As can be seen, this work outperforms the previous work [31] on the 2-class problem and is the only one to date that reports quantitative results for the 3-class problem.

5.7 Contribution

The contributions described in this chapter, published in [90, 91], are:

- Finding pigment networks using the holes of the network.
- Using graphs for modeling the presence and coverage of pigment network structures.
- Developing a new measure called "Density Ratio" to detect absence or presence of pigment network structures.
- Locating nets of the pigment network structure and validating them using the holes segmented in previous steps.
- The proposal of a new clinically motivated feature set to classify a given image and assign a label of *Absent*, *Typical* or *Atypical* to each image.

- The validation of the proposed method on a large dataset consisting of 436 images, which is the only validation to date on the 3-class problem.

5.8 Conclusion and Future Work

We proposed a novel graph-based method for classifying and visualizing pigment networks and validated the method by evaluating its ability to classify and visualize the real dermoscopic images. Furthermore, we have proposed and validated a set of clinically motivated features over these sub-structures suitable for classification. Our feature set has proven to be robust, outperforming previous work on a large dataset consisting of 436 images, which is the only validation to date on the 3-class problem.

The accuracy of the system is 94.3% in classifying images to one of two classes of *Absent* and *Present* over a large and inclusive dataset consisting of 500 images. We also validate our method on a different set and achieve an accuracy of 82.3% discriminating between three classes (*Absent*, *Typical* or *Atypical*). This method can be used as a part of an automatic diagnosis system for classifying moles and detecting skin cancer. This is a novel idea that needs more investigation and evaluation and has a good potential for future research. Furthermore, we believe that the same idea with different features can also be applied for extracting other skin patterns such as globules and streaks.

Chapter 6

Detection of Streak Lines

As we described in Chapter 2.2.5, the presence of irregular streak lines is an important morphological expression of malignant melanoma. In particular, irregular streaks are one of the most critical features that shows the highest association with melanoma. Further, symmetric streaks are one of the specific dermoscopic criteria to differentiate usually benign Spitz nevi from melanoma. Therefore detection and analysis of streaks can be a significant step towards computer-aided diagnosis of skin lesions and melanoma detection. In this chapter, we propose a new approach to estimate and segment streak lines and classify them into *Absent*, *Regular*, and *Irregular* classes.

6.1 Overview

To locate candidate streak lines, we perform some preprocessing steps, and detect linear structures in the orientation flow of the image. Then to identify valid streaks from candidate streak lines, an orientation pattern analysis is performed and noise and wrongly detected lines are removed. The result includes line segments that indicate the pixels that belong to streaks. For identifying streaks and finding irregular patterns, we use the clinical criteria such as number of streaks in the images, color, and spatial arrangement of streaks to derive a set of features including structural (which characterizes shape), geometric (which characterizes distribution and uniformity), chromatic and textural features for detected line segments. These features are then used to train a supervised machine learning algorithm..

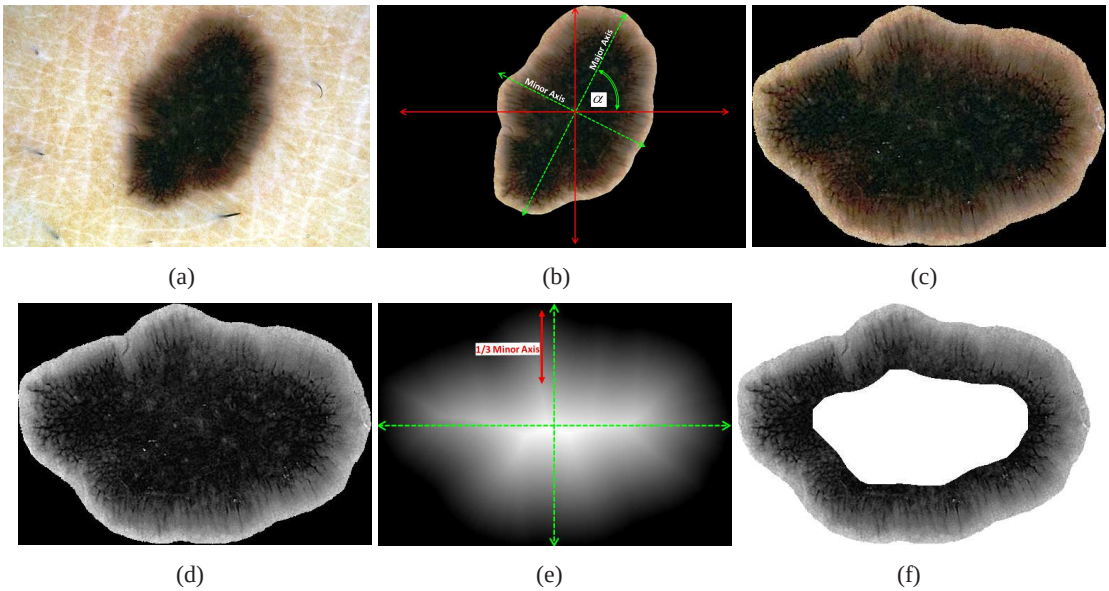

(a) (b) (c)

(d) (e) (f)

Figure 6.1: The preprocessing steps. (a) shows a lesion with *Regular* streaks and (b) illustrates the result of segmentation with major and minor axes of the lesion overlaid in green. (c) The result of re-orientation followed by re-sizing and sharpening is shown in (c) and (d) shows the L channel of the image in the L*a*b* color space. (e) shows the distance transform of the lesion mask with the major and minor axes of the lesion in green and the boundary thickness (1/3 of minor axis) in red and (f) illustrates the region of interest that will be processed to find streaks.

6.2 Pre-processing

First the lesion is segmented using our method [110] which employs supervised learning from a training set manually outlined by a dermatologist, in conjunction with the random walker algorithm [45]. Figure 6.1-a shows an original image, and Figure 6.1-b illustrates the result of segmentation with major and minor axes of the lesion overlaid in green. After segmenting the lesion, the orientation of the lesion which is the angle between the x-axis and the major axis of the ellipse, is found, and the image is rotated to align the major axis horizontally since the major axis represents the lesion growth direction (Figure 6.1-b). Then, to have a relatively uniform image size, the lesion is re-sized so that its major axis occupies 500 pixels. Since our images come from different resources with unknown imaging settings, we had to first normalize the size of the images to 500 pixels, and then we tuned the parameters of the method accordingly. These parameters can be tuned more accurately if imaging setting, scaling, and the resolution are known. Finally, the image is enhanced using a simple 3x3 high pass filter that removes the low frequency noise [91]. After sharpening, the image

is smoothed using an averaging filter of the same size to enhance sharp edges while removing noise. Figure 6.1-c shows the result of re-orientation followed by re-sizing and sharpening.

To get a single plane luminance image, the given RGB image is converted to the L*a*b color-space [112] which is designed to approximate human perception. Other color channels such as the green and blue channels of RGB, and Y of YIQ were also tested. Our experiments showed (in Section 4) that L* component outperforms other color channels; thus, we keep the L* channel, shown in Figure 6.1-d, for the rest of our analysis. Finally, to find the region of interest (ROI), which is the boundary of the lesion where we expect to find streaks, distance transform of the lesion mask is calculated from the lesion border. One third of the length of the lesion's minor-axis is used to determine the ROI. In fact, the minor axis is divided into three sections, where in the middle section we do not expect to see streaks. Figure 6.1-e shows the distance transform of the lesion mask with the major and minor axes of the lesion in green, and the boundary thickness in red, and Figure 6.1-f illustrates the ROI that will be processed to find streaks.

6.3 Identifying linear structures after orientation enhancement

6.3.1 Blob detection using Laplacian of Gaussian (LoG)

Since streaks are linear structures with Gaussian cross-sectional profiles, we detect the linear structures using LoG filters. To capture objects of different sizes a multi-scale approach is necessary. Thus, an input image $f(x, y)$ is filtered by rotationally symmetric LoG filters of size $hsize = 3, 5, 7, 9$ as follows:

$$h(x, y) = \nabla^2[g(x, y) * f(x, y)] = [\nabla^2 g(x, y)] * f(x, y) \quad (6.1)$$

$$\nabla^2 g(x, y) = \left(\frac{x^2 + y^2 - 2\sigma^2}{\sigma^4}\right)^{\frac{-(x^2+y^2)}{2\sigma^2}} \quad (6.2)$$

where σ is the standard deviation of the filters with a small value of 0.1 assigned in order to achieve high sensitivity even to a small change in intensity. We have performed 25 experiments with 5 different sigmas and 5 filter sizes, and our results show that the current setting gives the best results. At the end, we will use the union of the results from the four scales to form a multi-scale result. Figure 6.2-b, 6.2-c, and 6.2-d show the LoG responses at three different scales of $hsize_k = 3, 5, 9$ respectively.

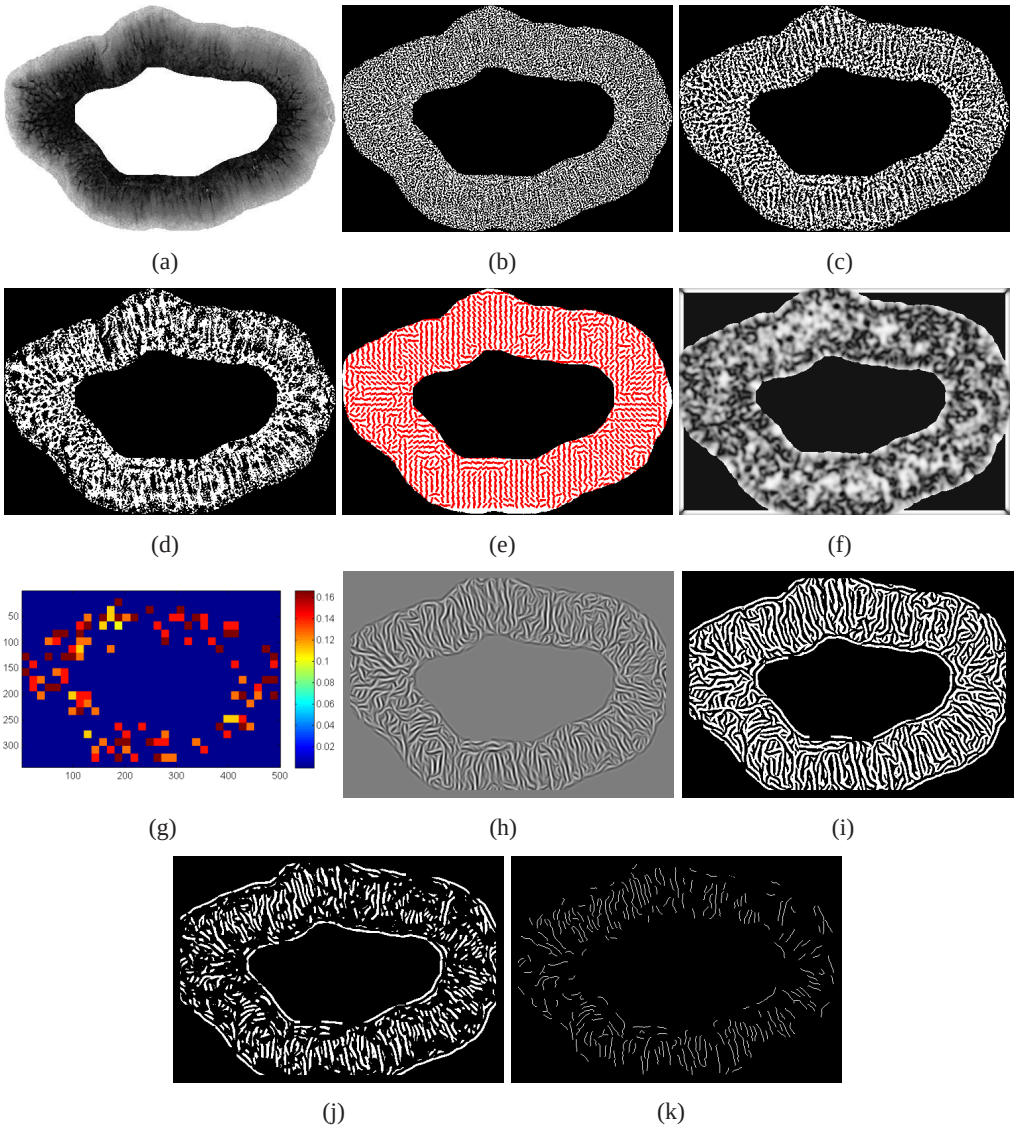

Figure 6.2: Intermediate steps of the method. (a) shows the region of interest in a lesion with *Regular* streaks in the L* channel after segmentation, reorientation and sharpening. (b), (c), and (d) show the LoG filter responses in three scales $hsize_k = 3, 5, 9$ respectively. (e) shows the orientation flow plotted in red lines for $hsize = 5$, and (f) shows the coherence or reliability of orientation estimation. The frequency of the parallel pattern, illustrated in (g), is used as a parameter of the Gabor filters which is created to enhance the estimation of the orientation as shown in (h). (i) shows the binary image of the enhanced orientation with 1 for ridges and 0 for valleys. (j) is created from (i) and (f) by removing pixels with $reliability \leq 50\%$. In the skeleton of the result, after removing joint pixels, the inner borders and also short line segments are removed using the min and max threshold of the length of line segments. The result is shown in (k) as detected linear structures in the image. These line segments will be validated for valid streaks selection as described in the section 3.4.

6.3.2 Orientation estimation

After finding linear structures by LoG, the orientation estimation is performed using the Averaged Squared Gradient Flow (ASGF) algorithm [60]. The reason for using squared gradient instead of the elementary gradient is that after computing the local orientation for a pixel, the estimation will be averaged over a block of 16×16. Since a ridge line has two edges, the gradient vectors at both sides of a ridge are opposite to each other. Therefore, gradients cannot directly be averaged since opposite vectors will cancel each other, although they indicate the same ridge-valley orientation. Therefore, by applying ASGF that doubles the angles of the gradient vectors before averaging, opposite gradient vectors will point in the same direction and will reinforce each other. Also, the length of the gradient vectors is squared. Thus, strong orientations have a higher vote in the average orientation than weaker orientations.

The qualitative analysis that was given above is made quantitative here. The algorithm starts by computing the gradients $G_x(i,j)$ and $G_y(i,j)$ at each pixel (i,j) in image I. For doubling the angle and squaring the length in ASGF, the gradient vector is converted to *polar* coordinates, in which it is given by $[G_\rho, G_\theta]$:

$$G_\rho = \sqrt{G_y^2 + G_x^2}, \qquad G_\theta = tan^{-1}(G_y, G_x) \tag{6.3}$$

$$G_x = G_\rho * cos(G_\theta), \qquad G_y = G_\rho * sin(G_\theta) \tag{6.4}$$

$$\begin{bmatrix} G_{s,x} \\ G_{s,y} \end{bmatrix} = \begin{bmatrix} {G_\rho}^2 cos(2G_\theta) \\ {G_\rho}^2 sin(2G_\theta) \end{bmatrix} = \begin{bmatrix} G_\rho^2(cos^2(G_\theta) - sin^2(G_\theta)) \\ G_\rho^2(2sin(G_\theta)cos(G_\theta)) \end{bmatrix} = \begin{bmatrix} G_x^2 - G_y^2 \\ 2G_xG_y \end{bmatrix} \tag{6.5}$$

$$DF = \frac{1}{2} tan^{-1}\left[\frac{2G_xG_y}{G_x^2 - G_y^2}\right] \tag{6.6}$$

where $\begin{bmatrix} G_{s,x} \\ G_{s,y} \end{bmatrix}$ is the squared gradient and DF is the directional flow of image I. The image is then divided into blocks of size W=16. For each block, the local orientation at pixel (i,j) is estimated and averaged using DF as follows:

$$\begin{bmatrix} \overline{G_{s,x}} \\ \overline{G_{s,y}} \end{bmatrix} = \frac{1}{|W|} \begin{bmatrix} \sum_W G_x^2 - G_y^2 \\ \sum_W 2G_xG_y \end{bmatrix} \tag{6.7}$$

where W is a non-overlapping window of 16×16. To reduce the effect of noise on the estimated orientation, a low-pass filter (Gaussian) is used to modify the local ridge orientation. To apply the

Gaussian filter, the orientation image is converted back to a continuous vector as follows:

$$\Phi_x(i,j) = \cos(2G_\theta(i,j)), \qquad \Phi_y(i,j) = \sin(2G_\theta(i,j)) \tag{6.8}$$

$$\Phi'_x(i,j) = \sum_W F(i,j)\Phi_x(i,j), \qquad \Phi'_y(i,j) = \sum_W F(i,j)\Phi_y(i,j) \tag{6.9}$$

where F is the Gaussian filter with unit integral and specified σ of $\sigma_\Phi = 5$.

Now, the local orientation and its reliability (the coherence of the squared gradients given by [60]) can be computed at pixel (i,j) using the following equation:

$$O(i,j) = \frac{1}{2}\tan^{-1}\left(\frac{\Phi'_y(i,j)}{\Phi'_x(i,j)}\right), \qquad Reliability = \frac{|\sum_W (G_{s,x}, G_{s,y})|}{\sum_W |(G_{s,x}, G_{s,y})|}. \tag{6.10}$$

which means if all squared gradient vectors are pointing in exactly the same direction, the sum of the vectors equals the modulus of the sum of the vectors, resulting in a coherence value of 1. On the other hand, if the gradient vectors are random in all directions, the sum of them will be 0, resulting in a coherence equal to 0. This algorithm results in a smooth intensity flow orientation over the image (shown in Figure 6.2-e), and Figure 6.2-f shows the reliability map of the orientation estimation of Figure 6.2-a.

6.3.3 Estimating ridge frequency

After finding the local orientation and averaging for image blocks, the local ridge frequency is estimated by rotating the block so that the ridges are vertical. Then, the columns are projected down to find peaks in the projected gray values by performing a gray-scale dilation and then finding where the dilation equals the original values and it is higher than mean of the projected gray values. The frequency of ridges can be calculated by dividing the distance between the first and last peaks by (number of peaks - 1), and finally the median frequency is computed over all the blocks in the image. Figure 6.3-a shows an example block of 32×32 annotated on the LoG response. The window size of 32 is used for a better illustration in the paper, however the window size used in our experiments is 16×16. The block is magnified in Figure 6.3-b for illustration. The result of rotating the block with the average block orientation to make it vertical is shown in Figure 6.3-c, and the projection and dilation results are shown in Figures 6.3-d and 6.3-e respectively. Now peaks of the block, pointed with red arrows, can be easily found by comparing the dilation and projection results. The frequency is found using these peaks and their wavelength. The wavelength of this block is $(18-4)/2 = 7$

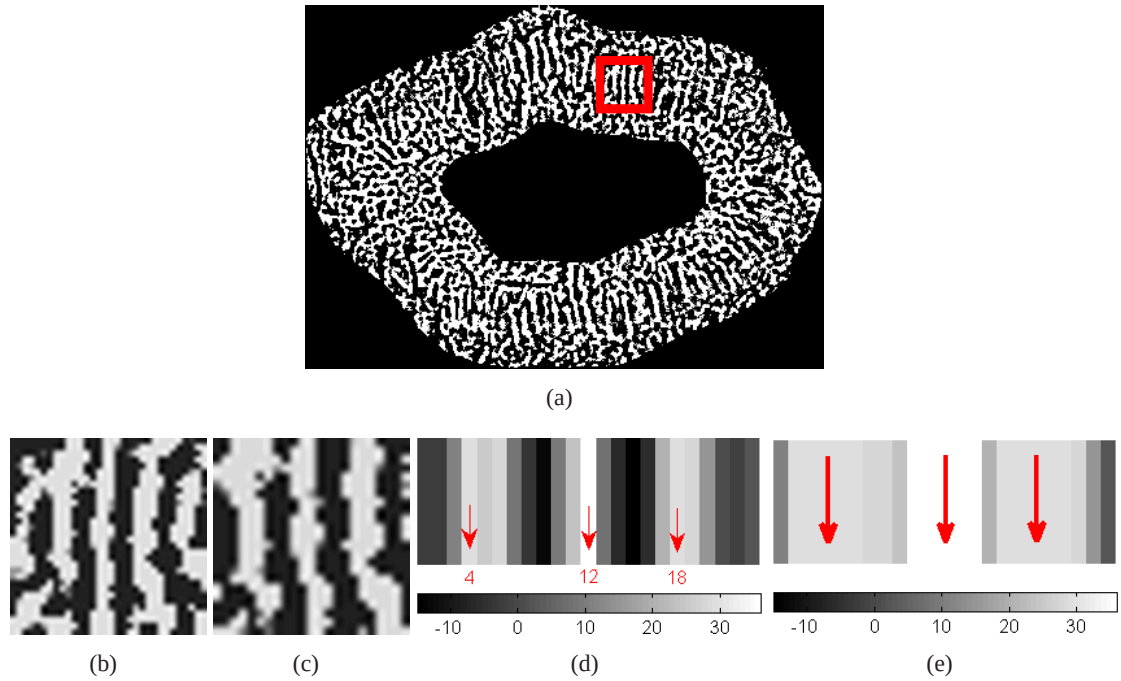

(a) (b) (c) (d) (e)

Figure 6.3: Ridge frequency estimation. (a) shows an example block annotated on the LoG response. (b) shows the magnified block for illustration. (c) illustrates the result of rotation and cropping with average block orientation; 8 degrees for this block. (d) shows the projection and (e) the dilation, with red arrows pointing to the peaks where the dilation equals the original value and is higher than the mean of the projected gray values. The wavelength of this block is $(18 - 4)/(3 - 1) = 7$ which results in a frequency of $1/7 = 0.14$.

that results in frequency of $1/7 = 0.14$. The final result of frequency estimation for all blocks of our example image (6.2-a) is shown in Figure 6.2-g.

6.3.4 Enhancing the orientation image

From [54], a Gabor filter with tuned ridge frequency and orientation, can remove the noise efficiently while preserving true ridges and valleys. The even-symmetric Gabor filter has the general form of

$$g(x, y; f, \theta, \sigma) = \exp\left(-\frac{x'^2 + y'^2}{2\sigma^2}\right)\cos\left(2\pi f x'\right), \tag{6.11}$$

$$x' = x\cos\theta + y\sin\theta, \qquad y' = -x\sin\theta + y\cos\theta \tag{6.12}$$

where σ is the sigma of the Gaussian kernel in the filter, and f and θ are the corresponding median ridge frequency over the image and local orientation respectively. The result of this step is shown in Figure 6.2-h. Figure 6.2-i shows the binary image of the enhanced orientation created by thresholding (1 for ridges and 0 for valleys), and Figure 6.2-j is created from Figures 6.2-f and 6.2-i by removing pixels with $reliability \leq 50\%$. In the skeleton of the result, after removing joint pixels, the inner borders and also short line segments are removed using the min and max threshold of the length of line segments. The result is shown in Figure 6.2-k as detected linear structures in the image. These line segments, called candidate streak lines, will be validated for valid streaks selection in the next step.

6.4 Identifying valid streak lines from candidate streaks

So far, we have identified many line segments which are spread in different directions belonging to either streaks, or other dermoscopy structures and artifacts such as hairs. According to the clinical and mathematical definitions of streaks, we expect to see a smooth orientation change in the streaks directions. To capture the underlying pattern, we need a geometric investigation that identifies valid streaks and removes false positives from the candidate streak lines. Skin lesions are mainly circular in dermoscopy images, but they can be any shape. We generalize the lesion shape as an ellipse that has the same normalized second central moments as the lesion region. Two foci F_1 and F_2 are computed using the eccentricity of the ellipse. To test whether a line segment, for example the red line segment with the angle β_1 with respect to the horizontal direction and the centroid of A_1 in

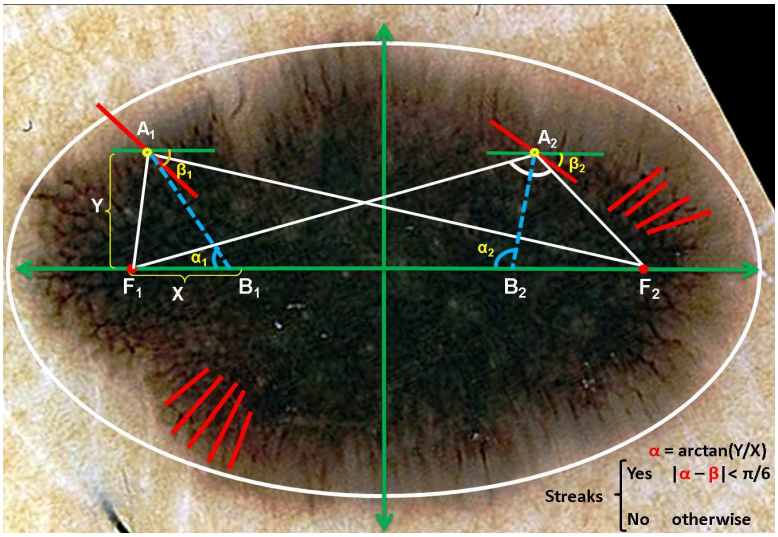

(a)

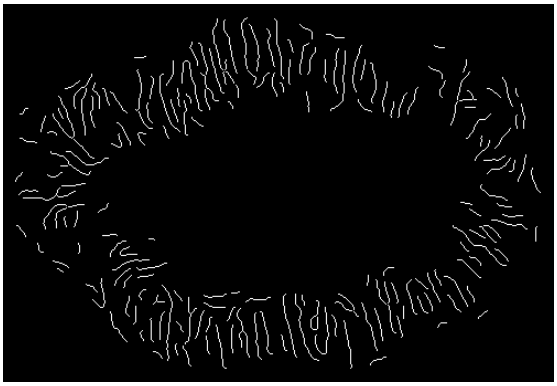

(b)

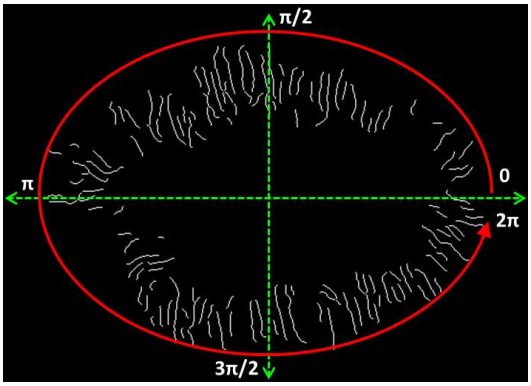

(c)

Figure 6.4: Validating streaks candidates. (a) illustrates how line segments are filtered based on their orientation difference $(\pi/6)$ from the expected direction. (b) shows the line segments detected after orientation estimation and (c) shows valid streaks after removing false positives.

Figure 6.4-a, is a streak or not, we connect A_1 to F_1 and F_2 and compute the angle between A_1F_1 and A_1F_2 and find its bisector line (A_1B_1). We expect the orientation of a true streak line segment will coincide with the bisector line A_1B_1. To test such a condition, the angle between A_1B_1 and the line joining the foci F_1F_2 (α_1) is compared to the orientation angle β_1 of the line. We measure all orientations counterclockwise from the horizontal axis in the range of $[0, 2\pi]$. By comparing $|\alpha - \beta|$ to a constant threshold of $\pi/6$, non-streak line segments are eliminated from the set of detected lines, and reliable line segments at every scale are found to form a multi-scale result to be used for feature extraction. For example, in Figure 6.4-a, the line segment A_1 will be kept, but the line segment A_2 will be removed. Reliable lines detected after orientation enhancement are shown in Figure 6.4-b, and the result of valid streaks selection is illustrated in the Figure 6.4-c. These valid streaks are ordered in the direction of the red arrow from 0 to 2π for feature extraction in the next step.

6.5 Feature extraction

Based on our mathematical definitions of streaks, we propose a new set of 20 features for streaks, called *STR* (streaks), which includes three Structural, three Geometric, six Orientation, and eight Chromatic characteristics of valid streaks.

We have also used common color and texture features [25, 92] of the lesion itself, called *LCT* (Lesion Color Texture).

6.5.1 Our *STR* features

STR is a clinically inspired feature set, based on our mathematical definition of streaks to model characteristics of *Absent*, *Regular*, and *Irregular* streaks.

Structural Features (3 features)

Diagnostically important characteristics of streaks include the shape, length, and variability of lines. Therefore, we compute the length of each line, which is the number of pixels of the line segment. Our features are the mean of the lengths of streaks, and the total number of line segments in the image. We also include the ratio of the streak size to the lesion size (# of streak pixels/# of pixels in the lesion area).

Geometric Graph Features (3 features)

Clinically, there is an emphasis on the 'uniformity' and smoothness of the orientation change in streaks for irregularity detection. There is also another important characteristic which is connectivity of the structure that represents the completeness of the pattern. In Chapter 5, we proposed the 'Density Ratio' feature which represents the density of the dermoscopy structure called pigment network (PN). We have used a similar concept here with some modifications to measure the density of streaks on the image. This feature is useful to discriminate *Absent* images from *Present* images.

For geometric analysis, we created a graph of the N valid streak lines found in the previous section, by reducing each line L to v_n nodes, based on the average length of streaks in the image. For N lines, the total number of nodes equals to $|V| = \sum_{i=1}^{N}((\frac{|L_i|}{\sum_{j=1}^{N}|L_j|/N}) + 1)$ where $|L_i|$ is the length of the line segment L_i in the image and $\sum_{j=1}^{N}|L_j|/N$ denotes the average length of streaks.

Density Ratio: A graph $G = (V, E)$ consists of pairs with vertices (nodes) $v \in V$ and edges $E \subseteq (V \times V)$. The standard *Density* of graph G is defined in [28] as the ratio of edges in G to the maximum possible number of edges $Density = \frac{2\times|E|}{|V|\times(|V|-1)}$ where $|E|$ is the number of edges, and $|V|$ is the number of vertices in graph G. Inspired by [91], we defined the density measure of the graph of streaks as following:

$$Density_{streaks} = \frac{|E|(\log|E|)}{|V| \times log(LesionSize)} \tag{6.13}$$

where $LesionSize$ is the size of the segmented lesion in pixels. The density feature is useful in discriminating between the *Absent* and *Present* images, however it does not say much about the regularity or irregularity of the streaks, nor the completeness and coverage of the pattern.

Often there is a complete pattern with a high graph density in *Regular* streaks all over the lesion (Figure 6.5-a, 6.5-c, 6.5-e), whereas in *Irregular* streaks, there may be a dense graph but over only small parts of the lesion (Figure 6.5-b, 6.5-d, 6.5-f). Therefore, we need another measurement to find out if the dense pattern is distributed all over the lesion or if it is just partially covering the lesion. Thus we propose two new features called pattern coverage, and completeness.

Coverage: To measure the coverage of the streak pattern, the histogram of the number of streaks in different areas (arcs) of the lesion is computed for bins of $\pi/6$ in the range of $[0, 2\pi]$. According to the mathematical definition of streaks, we defined the graph coverage as the fraction of bins with more than 2 streak lines (based on the clinical definitions of streaks). Coverage ranges from 0 to 1

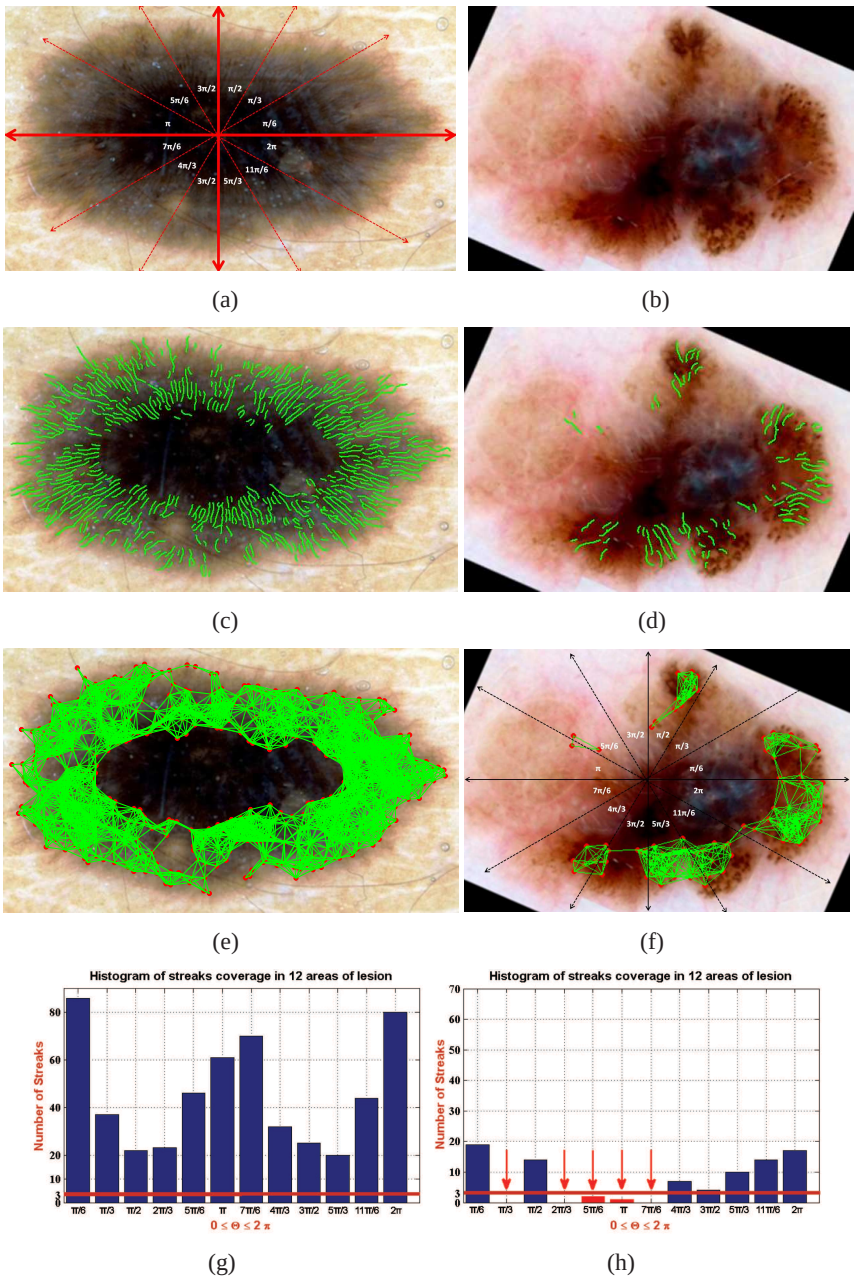

(a) (b) (c) (d) (e) (f) (g) (h)

Figure 6.5: Lesions with *Regular* (a) and *Irregular* (b) streaks. The red lines in (a) segment the lesion into 12 areas to calculate the coverage of streaks. (c) and (d) show the results of multi-scale streak detection on (a) and (b). (e) and (f) illustrate the graphs of streaks plotted over the lesions. In (g) and (h) the coverage histograms of (e) and (f) are shown respectively. The histogram counts the number of streaks observations into each of the bins of $\pi/6$ in the range of $[0, 2\pi]$. From the histogram (g), Coverage is 1 (maximum) and in (h), the red arrows point to the bins with less than 3 line segments and Coverage is $7/12 = 0.58$.

and the perfect coverage is equal to one that often belongs to *Regular* streaks which are distributed symmetrically among the bins (Figure 6.5-g). Lesions with *Irregular* streaks often have a lower Coverage because of the partial distribution pattern (Figure 6.5-h). Figure 6.5-a shows a lesion divided by red arrows into 12 areas and Figure 6.5-g shows the coverage histogram of the lesion with regular streaks. As shown in the figure, the number of streaks in the horizontal bins $\pi/6$,π, $7\pi/6$, and 2π are often higher than other bins because of the growth pattern of the lesion in the horizontal (major) axis.

Completeness: If each vertex v_i in G is reachable from the other vertices v_j, then G is connected and a maximal connected subgraph $G_w = G(V_w, E_w)$ is the largest connected subset W of the vertex set V. Based on the above definitions the pattern completeness is equal to $Completeness = \frac{Density_{streaks}}{|G_w|}$ where $|G_w|$ is equal to the number of maximal connected subgraphs in the image.

Orientation Features (6 features)

The orientation information of valid streak lines can also reveal valuable information about the presence and regularity or irregularity of streaks. We order the valid streaks to track the orientation change to detect the underlying pattern, if any. The line segments are ordered based on their location and their orientation from the major axis starting from 0 to 2π in the counter-clockwise direction (Figure 6.4-c). In Figure 6.6-a, streaks are ordered in the *x* axis and their corresponding orientation in the *y* axis are shown for a typical lesion with *Regular* streaks (in red) and a lesion with *Irregular* streaks (in green). *Regular* streaks tend to have smooth orientation changes without major jumps between consecutive data points comparing to irregular streaks. After ordering the line segments, based on the fact that they should be co-radially oriented, a linear regression is applied to measure the error from an expected perfect orientation change pattern, so that we can extract informative features of regularity or irregularity of the orientation change. Assume that the ordered valid streaks X_i are indexed by the subscript i, where i ranges from 1 to N (the total number of valid streaks), and y_i is the corresponding orientation. In the linear regression, y_i is a linear combination of the parameters of β_0 and β_1 with the variable x_i as $\widehat{y_i} = \widehat{\beta}_0 + \widehat{\beta}_1 x_i$ for $\quad i = 1, \ldots, N$. The residual, $e_i = y_i - \widehat{y_i}$, is the difference between the predicted orientation of the line segment i by the model ($\widehat{y_i}$), and the true direction of line (y_i). The slope of the fitted line, β_1, is used as one of the orientation features. Figure 6.6 shows also the linear regression on the orientation data of the *Regular* and *Irregular* images. The slope β_1 for the regular streaks and irregular streaks are 0.67 and 4.6, respectively.

We also calculate the Root Mean Square Error (RMSE) of the model as $RMSE = \sqrt{\frac{\sum_i (\widehat{y_i} - y_i)^2}{N}}$.

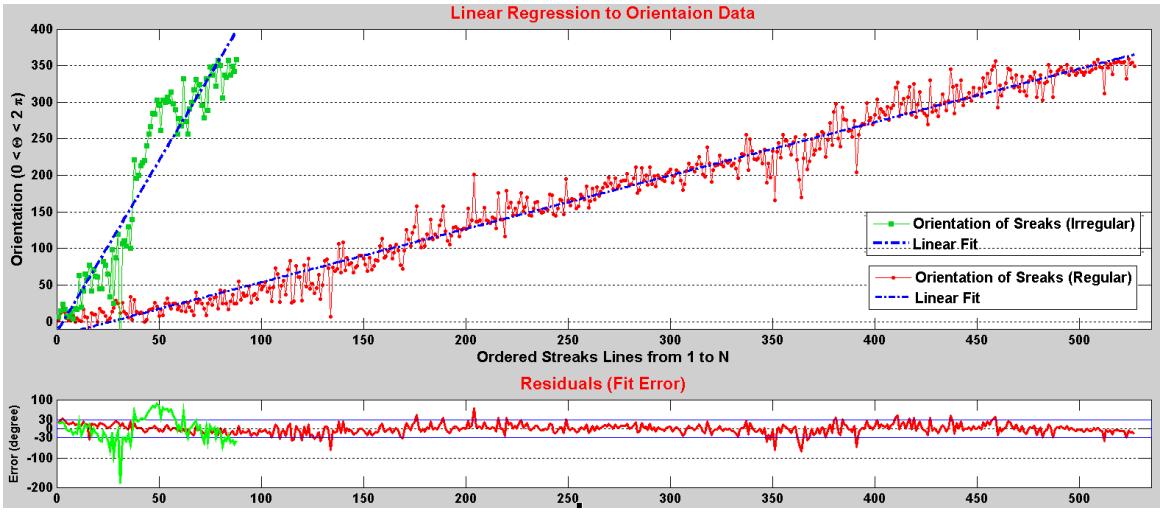

Figure 6.6: Linear regression of features extracted from the orientation pattern. The top figure shows the ordered line segments in the x axis with their corresponding orientation in axis y. The red data points show the orientation data for the regular lesion shown in Figure 6.5-c and the green data points illustrate the orientation of streaks of the *Irregular* lesion shown in Figure 6.5-d. The bottom figure illustrates the corresponding fit error (residuals) of the linear regression. The RMSE of *Irregular* streaks (in green) is 47.68 where the RMSE error of the regular streaks (in red) is 13.21. All residuals outside of the blue box in the bottom figure are counted and normalized by the number of line segments as our outliers feature.

Our experiments show that images with regular streaks have lower β_1 and RMSE which is because of the high number of streaks in the x axis with smooth orientation change in y. The bottom part of Figure 6.6 shows the residuals of the regression corresponding to the ordered streaks above. In this example, the RMSE of the irregular streaks (green plot) is 47.7 and the RMSE of the regular streaks (red plot) is 13.2.

Two more features involving residuals are the RMSE of the first derivative of orientations, and a normalized count of outlier orientations, the outlier ratio, shown outside the blue box in the residuals in Figure 6.6.

We have also used the entropy of the lines orientations and residuals to characterize the randomness or existence of a specific pattern in the orientation change. The entropy is a statistical measure of randomness and the motivating idea behind the entropy is that irregular streaks with unpredictable orientation change have a high entropy while regular streaks with a specific smooth orientation change show a relatively low entropy.

For X with N lines $\{x_i : i = 1, \ldots, N\}$, entropy is denoted by $H(X)$, and is defined as $H(X) = -\sum_{i=1}^{n} p(x_i) \log p(x_i)$ where $p(x_i)$ is the probability function of x_i and contains the histogram counts of b bins where $b = \frac{2\pi}{\pi/18} = 36$.

Chromatic Features of Streaks (8 features)

Since the images are not calibrated, we do not have reliable color information. Our color features of streaks include the mean, standard deviation of intensity values in H, S, and V channel of HSV color space as well as the choice of the color channel for luminance image (L* in our experiment) used for streak detection over segmented streak lines.

6.5.2 Lesion Color Texture features (16 features)

Lesion Color Texture (*LCT*) set include the following 16 features: The mean, standard deviation and reciprocal of coefficient of variation (mean/stdev) of the values in H, S, and V from HSV and L* of L*a*b*, and four of the classical texture measures; energy, contrast, correlation, and homogeneity [52, 92]. These textural features are derived from a Grey Level Co-occurrence Matrix (GLCM). The GLCM, constructed over the entire lesion, is a tabulation of how often different combinations of pixel brightness values (gray levels) occur in a pixel pair in an image. We created the GLCM matrix which analyzes pairs of adjacent pixels in the 4 directions of 0, 45, 90, and 135 degree in

the intensity image which is scaled to 8 levels. In this case, there are 8 x 8 = 64 possible ordered combinations of values for each pixel pair.

6.6 Classification

Finally, these 36 features are fed into the SimpleLogistic [65] classifier implemented in Weka. This choice of classifier was better than others such as Logistic, and BayesNet [38]. In the following section, we will report results of our 2 data sets for 3 set of features (*LCT*, *STR*, and *LCT+STR*) in classifying into 3-class of *Absent*/*Regular*/*Irregular*, 2-class of *Absent*/*Present*, and 2-class of *Regular*/*Irregular*.

6.7 Evaluation and Results

6.7.1 Data sets

In our experiments, two dermoscopic image sets with 945 and 300 images (taken from the 945) are used to evaluate the proposed method. The set of 945 dermoscopic images were taken from three different resources, and contained 570 Absent, 245 Irregular, and 130 Regular streak images. The first resource subset included 745 images from [10] where each image was labeled as (*Absent*, *Regular* or *Irregular*) representing the presence and regularity of streaks in the image. For the second subset, we collected 100 images from the web which were reported to have streaks (*Regular* or *Irregular*) and for the third resource subset, 100 images with *Absent*, *Regular* or *Irregular* labels were taken from [100]. By adding these three subsets, we created the set of 945 images (Set1) for our first experiment to demonstrate the strength of the proposed method over a large number of dermoscopic images. Some of these images were challenging due to the acquisition parameters such as lighting and magnification; being partial (entire lesion was not visible); or due to the presence of an unreasonable amount of occlusion by either oil or hair. Such challenging images are usually discarded from test sets in previous works, but we kept these images in our test set. In the second experiment, we selected randomly a set of 300 clean and high resolution images from Set 1, (105 *Absent*, 110 *Irregular*, and 85 *Regular*) with a complete lesion and without artifacts such as hair or oil bubbles (Set2).

We report the results of the experiments in Tables 6.1 and 6.2.

6.7.2 Evaluation-Qualitative Results

Figure 6.7 illustrates six examples of our qualitative results with streak lines overlaid on the images and streaks graphs. The first two rows of Figure 6.7 show *Absent* images, with a few lines detected as potential streak lines in the second column and very sparse and low density graphs in the third column. The third and forth rows illustrate results of streak detection and graphs on two images with regular streaks in which Figure 6.7-g has the radial streaming streaks and Figure 6.7-j shows pseudopod streaks demonstrating how our method successfully detects pseudopods. The last two rows of Figure 6.7 show melanomas, with irregular streaks. The high difference in graph densities and spatial arrangements and distribution is clear for different classes.

Detection and diagnosis of regular and irregular streaks is challenging even for experts. According to [100] there was an average disagreement of 24.5% on 2-class problem (*Absent*/*Present*) between 40 Experts. The difficulty and disagreement is even more on the 3-class problem for detecting irregular streaks. Figure 6.8 shows 3 examples of challenging images from the difficult image set with 945 images. Figure 6.8-a shows the result of streak detection on a difficult case (case 43, page 150 in [100]) that is labeled as: *Absent* (33.3%), *Regular* (17.9%), and *Irregular* (48.7%). Our method assignes a label of *Irregular* with 68% probability. Detected streak lines are shown in Figure 6.8-b in green. Figure 6.8-c shows an *Absent* image that has co-radial liniear pigmented structures which belong to clods and maple leaf structures in a pigmented basal cell carcinoma. Our method classified the image correctly because of the low number of detected streak lines and the low density and coverage of the graph. Another challenging lesion with a strong pigment network is shown in (e) and the result of streak detection is shown in (f) with a very few false positive lines in green, and correctly classified as *Absent*. Figure 6.8-g shows one of the missclassified images. It is an *Absent* image with *unspecific* patterns that was diagnosed to be excised, but due to the linear co-radial stuctures in the boundary area of the lesion, it is missclassified as *Irregular*.

6.7.3 Evaluation-Quantitative Results

To evaluate the generalizability of our method, we conducted ten-fold cross-validation in the first experiment on Set1 with 5 scales (four scales of $hsize_k = 3, 5, 7, 9$ and union of these scales) in 4 color channels, in total 20 settings. The color channels used as the luminance image for streak detection are B and G channels of RGB, L of L*a*b*, and Y from YIQ ($Y = 0.299R + 0.587G + 0.114B$). Table 6.1 shows our results on Set1 with 945 images, using different color transformations on the

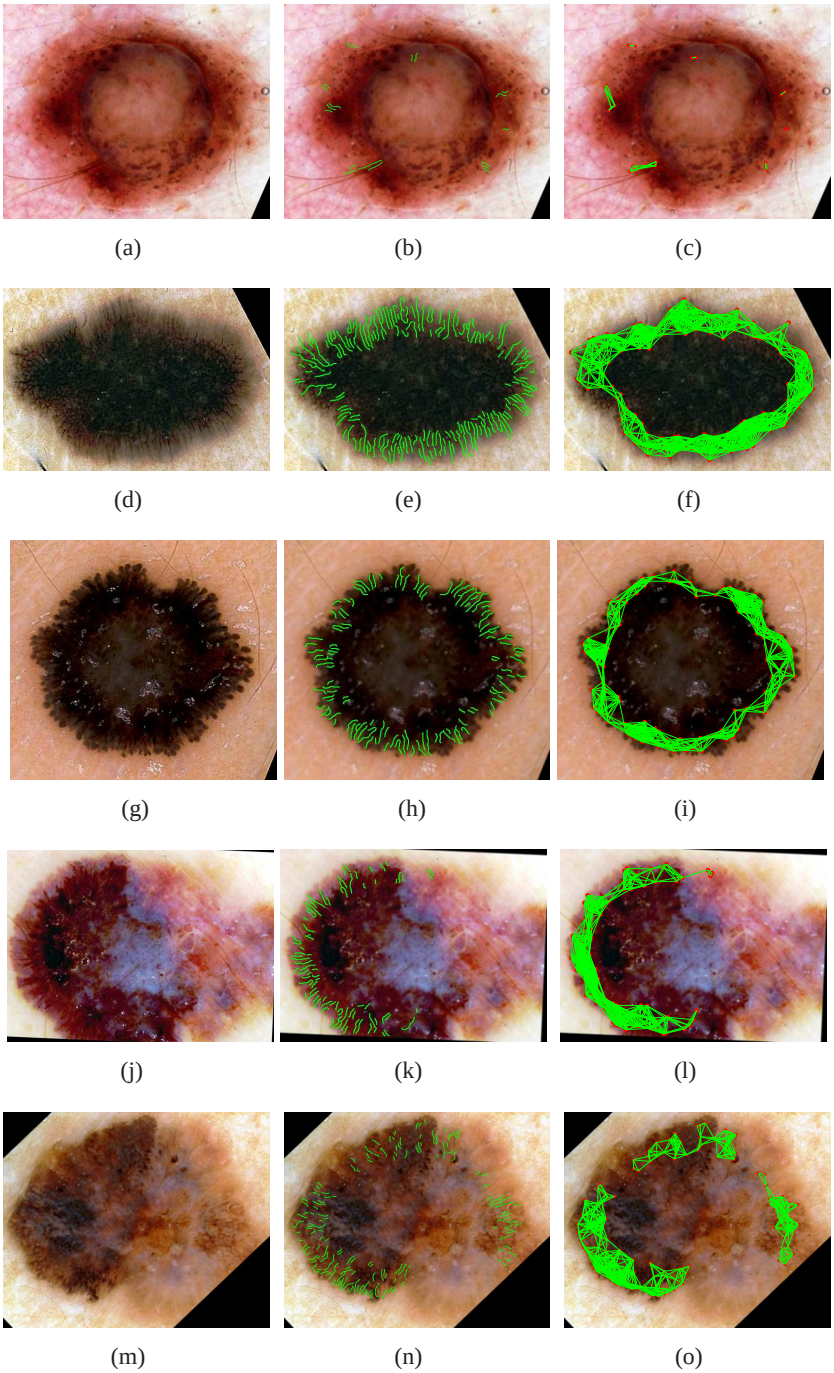

Figure 6.7: Two Examples of each of the *Absent*, *Regular*, and *Irregular* classes are shown. (a) illustrates an *Absent* image from our experiments with streak lines and graphs in the second and third columns respectively. (g) and (j) show two *Regular* (Spitz nevus) images with radial streaming and pseudopods respectively, and two lesions (melanomas) with *Irregular* streaks are shown in (m) and (p).

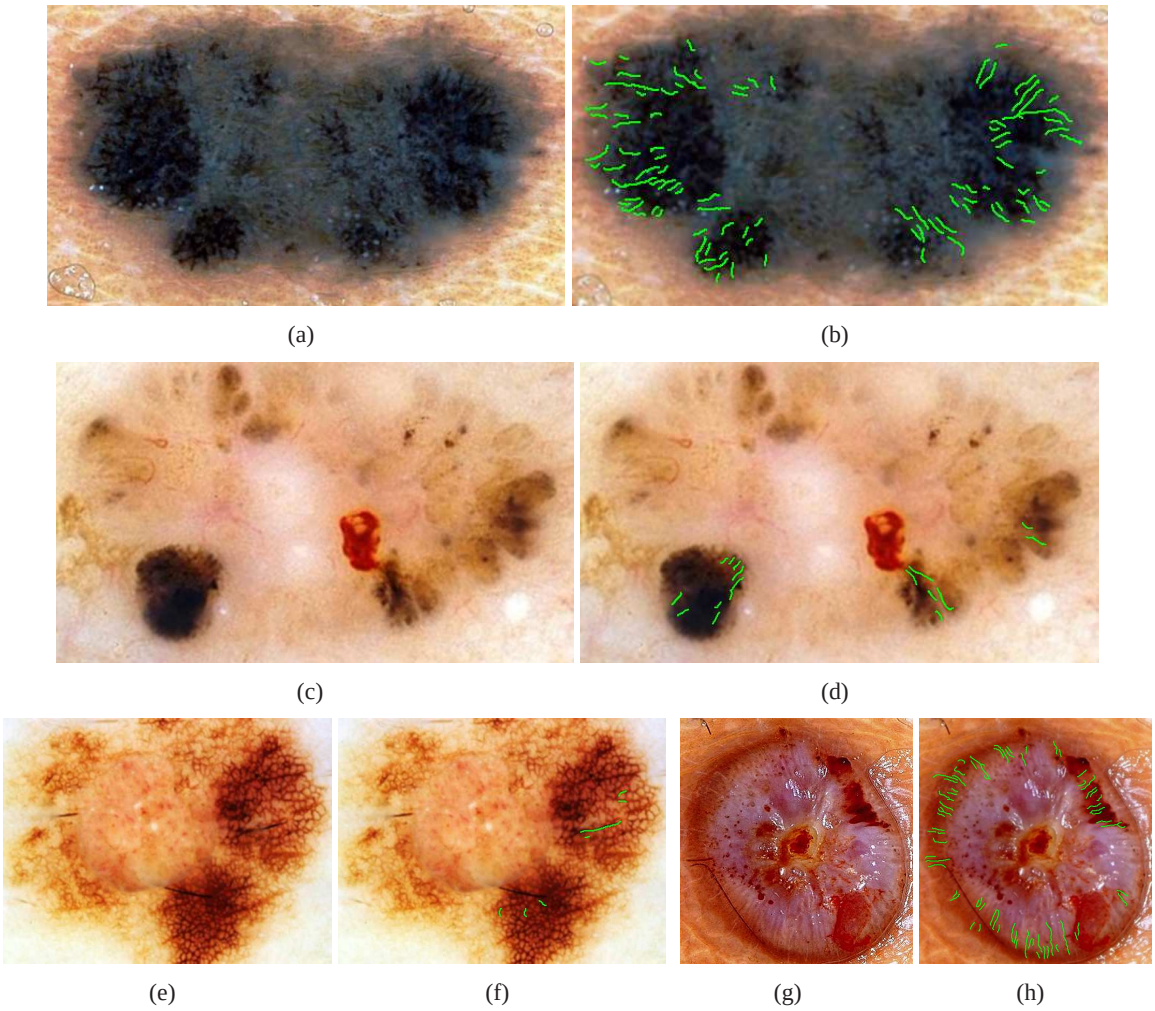

Figure 6.8: Our qualitative results on challenging examples. (a) shows a difficult image labeled by 40 experts with 33.3% inter-expert disagreement favoring *Present* and 26.8% disagreement favoring *Irregular* diagnosis. Our method assignes a label of *Irregular* with 68% probability. Detected streak lines are shown in (b) in green. (c) shows an *Absent* image that has co-radial liniear pigmented structures which belong to clods and maple leaf structures of the lesion called pigmented Basel Cell Carcinoma. A challenging lesion with a strong pigment network is shown in (e) and the result of streak detection is shown in (f) with a very few false positive lines. Our method classified (c) and (e) correctly because of the low number of detected streak lines, and the low density and coverage of the graph. (g) shows one of the *Absent* images that our method failed to classify it correctly (missclassified as *Irregular*) due to the linear co-radial blood stuctures in the lesion boundary.

multi-scale 3-class classification (*Absent*/*Regular*/*Irregular*) in which the L channel of L*a*b* outperformed the others. The best setting was used in the second experiment on Set2 with N=300 images. We report Recall (ie. Sensitivity, TP/(TP+FN); Precision (ie. Positive Predictive Value, TP/(TP+FP)); Accuracy=(TP+TN)/N; and AUC (the Area Under ROC Curve).

Color Channnel	G	B	Y (YIQ)	L (L*a*b)
Correct Classification	0.74	0.68	0.73	**0.77**

Table 6.1: Correct classification rates (accuracy) of various image transformations for multi-scale 3-class streaks classification on 945 images (Set1).

Table 6.2 summarizes the evaluation of our method for the 2-class (*Absent*/*Present* and *Regular*/*Irregular*), and 3-class (*Absent*/*Regular*/*Irregular*) classifications in Set1 and Set2 using different feature sets: *LCT*, *STR*, and *LCT+STR*. The highlighted numbers in the table show the evaluation results using all features (*LCT+STR*) combined. This table reports the results of 12 experiments in terms of Precision, Recall, F-measure, Accuracy and weighted average Area Under Curve (AUC) for the multi-scale analysis on the L channel of L*a*b*. The weighted average AUC is a good performance measure in imbalanced data sets with unequal numbers of observations in each class such as Set1 because it illustrates the behavior of the classifier without regard to class distributions or error costs [55].

A 10-fold cross-validation is used to evaluate our method and compare the results of different experiments. As shown in Table 6.2, by combining the new features and the common color and texture features, we achieved an accuracy of 77% and AUC of 84.7% for classifying streaks into *Absent*, *Regular*, and *Irregular*, on N=945 images (Set1) without any exclusion criteria. We also validate our method on a clean sub-set of Set1 with N=300 images with high contrast and no artifacts. The classification accuracy for the 3-class problem on the second set is 80% with AUC of 91.8%. Our method also works well on discriminating *Regular* streaks from *Irregular* ones with AUC of 88.9% on Set1 with N=945 images.

As mentioned before, Table 6.2 reports the weighted average of our performance measures. To show the class specific results on Set1, Figures 6.9 and 6.10 illustrate our detailed evaluation on the 3-class (*Absent*/*Regular*/*Irregular*) and the 2-class (*Absent*/*Present* and *Regular*/*Irregular*) problems. Figures 6.9-a, 6.9-b, and 6.9-c show class specific results of our method in more details for the *Absent*, *Regular*, and *Irregular* classes respectively for Set1 with 945 images. ROC curves of

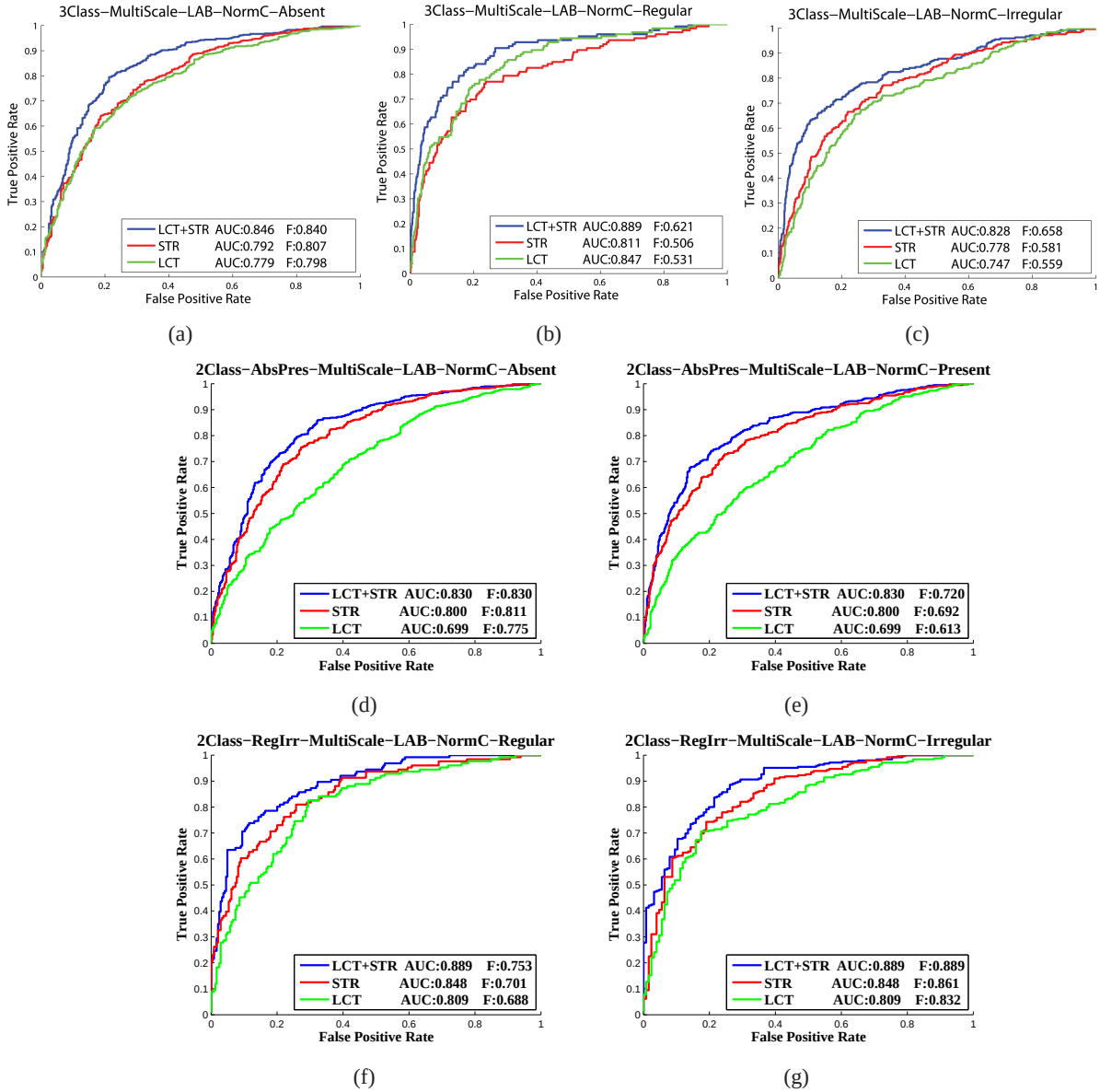

Figure 6.9: ROC curves of multis-scale streak detection using the *LCT*, *STR*, and *LCT+STR* feature sets in Set1 with N=945 images. (a), (b), and (c) show the AUC and F-Measure of our 3-class classification for the *Absent*, *Regular*, and *Irregular* classes respectively. (d) and (e) present the performance of our approach for *Absent*/*Present* classification for the *Absent* and *Present* classes respectively. The ROC curves on *Regular*/*Irregular* classification are shown in (f) and (g) for the *Regular* and *Irregular* classes respectively. In all of the plots except (b), our proposed feature set (*STR*)outperforms the *LCT* set and using all features together (*STR+LCT*) results in a significant improvement in AUC and F-Measure of all classifications.

	Experiment	N	Features	Prec.	Recall	F-Measure	Acc.	AUC
Set1	Abs/Pres	945	LCT	0.667	0.674	0.654	0.674	0.7
			STR	0.743	0.743	0.74	0.743	0.801
			LCT+STR	**0.784**	**0.786**	**0.783**	**0.785**	**0.83**
	Reg/Irr	375	LCT	0.712	0.722	0.714	0.722	0.802
			STR	0.791	0.795	0.79	0.795	0.849
			LCT+STR	**0.834**	**0.836**	**0.834**	**0.835**	**0.889**
	Abs/Reg/Irr	945	LCT	0.577	0.583	0.578	0.59	0.761
			STR	0.679	0.696	0.677	0.7	0.792
			LCT+STR	**0.764**	**0.77**	**0.762**	**0.77**	**0.847**
Set2	Abs/Pres	300	**LCT+STR**	**0.89**	**0.89**	**0.89**	**0.89**	**0.929**
	Reg/Irr	195	**LCT+STR**	**0.866**	**0.867**	**0.866**	**0.866**	**0.898**
	Abs/Reg/Irr	300	**LCT+STR**	**0.802**	**0.8**	**0.801**	**0.8**	**0.918**

Table 6.2: Evaluation of the proposed method on the two set with N=945 and N=300 (selected high resolution and clean) images. The 2-class experiment includes the *Absent*/*Present* and *Regular*/*Irregular* classifications and in the 3-class images are classified into *Absent*/*Regular*/*Irregular*. We have evaluated the Lesion Color Texture Feature Set (*LCT*) and the proposed Streaks Feature Set (*STR*) separately and combined. The highlighted numbers show the evaluation results using all features (*LCT+STR*) combined. This table reports the summary of our results of 12 experiments in terms of weighted average Precision, Recall, F-measure, Accuracy and Area Under Curve (AUC) for the multi-scale analysis on the L* channel of L*a*b*.

classifications using *STR*, *LCT*, and *STR+LCT* are shown to demonstrate the strength of our proposed features in discriminating between *Absent*, *Regular*, and *Irregular* streaks. Figures 6.9-d and 6.9-e illustrate the ROC curves of *Absent* and *Present* labels in the 2 class problem of *Absent*/*Present* classification, and results of our *Regular*/*Irregular* classification are shown in Figures 6.9-f and 6.9-g for the *Regular* and *Irregular* labels respectively. In almost all of the plots (except 6.9-b) our proposed feature set (*STR*)outperforms the *LCT* set and using all features together (*STR+LCT*) results in a significant improvement in AUC and F-Measure of all classifications.

As explained in the method, we have used 4 different scales for streak detection ($hsize_k = 3, 5, 7, 9$) and then the responses are combined to achieve the final multi-scale result. Figure 6.10-a shows the ROC curves of different scales for the class *Absent* in the 3-class classification of streaks in the L* channel on Set1. The multi-scale analysis outperforms the single scales with AUC of 82.8%. We have also reported results of classification on Set1 using ROC curves of 3 different classifiers, Simple Logistic, Logistic, and Bayes Net in Figure 6.10-b.

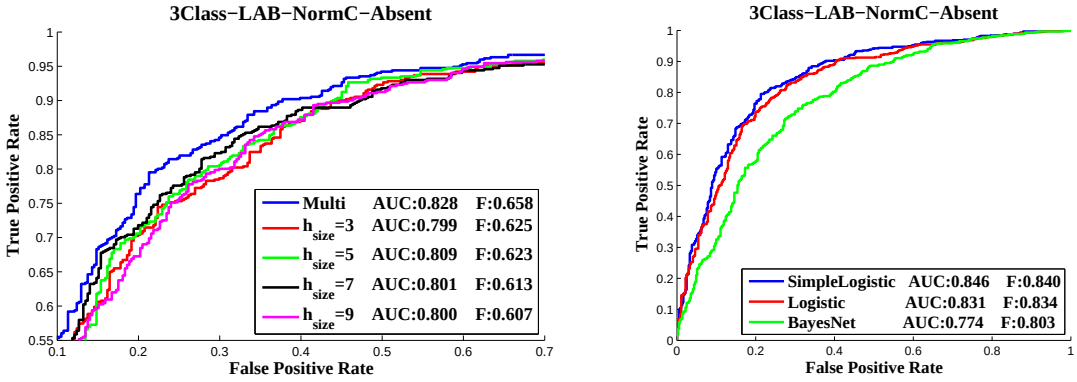

(a) (b)

Figure 6.10: ROC evaluation for different scales and classifiers. (a) shows the results of different scales ($hsize_k = 3, 5, 7, 9$) and union of these scales in *Absent*/*Regular*/*Irregular* classification of streaks in the L* and (b) presents the performance of different classifiers using all features (*LCT+STR*) in the L* channel with multi-scale settings.)

To compare our results with previous work, a direct comparison of our results is not possible because of unknown images and ground truth used in experiments. However, we deliberately created a difficult dataset of 945 images by not excluding oily, hairy, low-contrast, and partial images to demonstrate the strength of the method. Images used in [77] are from the same source that we have used in our experiment. Assuming the difficulty level of the images in [77] is similar to those of one of our data sets, our approach achieves an AUC of 91.8% compared with 83% reported in [77] for the 2-class *Absent*/*Present* classification.

6.8 Contribution

The contributions described in this chapter, published in [89], are:

- The development of an automatic approach for detection, segmentation and visualization of streaks.
- The proposal to use techniques based on ridge and valley detection used in fingerprint image recognition.
- The proposal of orientation estimation and correction to detect low contrast and fuzzy streak lines.

- The use of ridge frequency estimation to enhance the orientation estimation
- The use of orientation pattern analysis to remove noise and non-streaks line segments.
- The development of a graphical representation to analyze the geometric pattern of the structure over the lesion with new features designed to model the distribution and coverage of the structure.
- The development of a clinically inspired feature set to classify a given image into *Absent*, *Regular*, or *Irregular* classes.

6.9 Conclusion

We have presented an automatic approach for detection of radially oriented streaks on almost 1000 real dermoscopic images, using techniques based on ridge and valley detection used in fingerprint image recognition. Orientation estimation and correction is applied to detect low contrast and fuzzy streak lines and the detected line segments are used to extract clinically inspired feature sets for orientation analysis of the structure. A graph representation is used to analyze the geometric pattern of the structure over the lesion with new features designed to model the distribution and coverage of the structure. We demonstrated that the proposed approach can locate, visualize, and classify streaks in dermoscopy images. Therefore, it can be used in computer-aided melanoma diagnosis using scoring methods. Furthermore, since our method locates streak lines and provides a qualitative analysis, it can be used to highlight suspicious areas for experts' diagnosis and for visualization and training purposes.

We successfully apply our method in the specific case of automatic detection and classification of streaks on dermoscopy images, which represent a stereotypical example of linear radial patterns. In addition, oriented patterns produced by propagation, accretion, and deformation in radial phase, are common in nature and also in different fields of computer vision, and they are an important class for visual analysis. Our approach helps to understand such patterns, by analysis of co-radial linear structures in low contrast and low resolution images, in applications of histopathology, video capsule endoscopy, mammography, iris detection in retina images, sunspot modeling, industry and manufacturing.

Chapter 7

Towards Prevention of Skin Cancer

As mentioned before, in Chapter 1, it is known that skin cancers can be cured and survival rates significantly improved if patients are diagnosed at an early stage in the development of their disease. In addition, many cases of skin cancer are preventable. Therefore, the most important aspect of skin cancer management is public education (primary prevention) and early diagnosis (secondary prevention).

The secondary prevention involves the early detection and intervention. The proposed methods in the previous chapters focus on presenting a new methodology to be used in computer-aided diagnosis of skin lesions with more emphasis on the detection and analysis of two important dermoscopy structures (pigment network and streaks) to simulate the clinical diagnostic scoring approaches. These steps can aid early diagnosis of melanoma as the secondary prevention steps. In this research and thesis, we also made an attempt towards the primary prevention of skin cancer, by public education particularly through awareness of sun-damage, by providing unique solutions based on technology uses of social media and the Internet, using low-cost technological gadgets such as smartphones.

This chapter focuses on our attempts towards the primary prevention of skin cancer by raising public awareness. Experience from other countries, particularly Australia, demonstrates that it is possible to substantially change a population's behavior in sunlight, and also have them present much earlier for the diagnosis of skin cancer. This has resulted in a fall in death rates from skin cancers [12].

Overexposure to the sun's ultraviolet (UV) rays causes skin damage that can lead to skin cancer, including melanoma which is the most dangerous kind of skin cancer [93]. The UV Index, issued daily by Environment Canada, is a simple measure of the intensity of the sun's UV radiation. The

index is a useful tool to alert people to the need for sun protection. The higher the index, the more careful they have to be when outside in the sun. I spearheaded a small group of graduate students to develop an iPhone application called ”UV-Canada” that helps people to check the UV index easily. It is a free iPhone app, launched in summer 2011, which received excellent reviews after it was featured on Global TV, with over 30,000 downloads. In the new release for summer 2012, we have employed state-of-the-art human-computer interaction techniques to design new smartphone apps for use by the public on beaches, in the water, and while working in the sun, with educational material about calculating the sunburn time, the risks of sunburn, the appropriate type and effectiveness of sunscreen, and provide tips on how to avoid sunburn.

The UV-Canada iPhone app has many unique features:

- It has been developed for Canada. We cover all the cities reported by Environment Canada.
- It gives reliable information because we have consulted with the dermatologists and experts of BC Cancer Agency and UBC Dermatology. We also use the governmental resource of Environment Canada for the weather forecast and the amount of daily UV in each city.
- It offers daily tips while opening the app.
- It gives the UV index based on the location of the users (GPS of the mobile device)
- The app also provides weather forecast. We added this feature to make sure users check the app more frequently.
- Users have an option to search for other cities as well. They can enter the name of the city or look for it from a provided list.
- This app provides knowledge about skin care and cancer to reduce the negative effects of long UV exposure. It has a tab called ”Tips”. Users can improve their knowledge about the UV index, skin cancer, sunscreen, tanning, skin aging and beauty, skin care of kids, and Vitamin D.
- There is a very important feature that users can get daily notifications about the latest status of the ultra violet (UV) radiation in users’ location of choice. They can turn this feature on/off. Users can also set a time to get the alert. They can also set a threshold to get the UV alert based on their skin sensitivity.

- The new advanced feature of our latest version will estimate the time for sunburn based on the users' choice of environment, their Fitzpatrick skin type (self-assessed by a quiz approved by dermatologists), the SPF of their sunscreen and the UV index of sunlight reported by Environment Canada. The modeling is based on [7]

Screen shots of the application are shown in Figure 7.1-a to 7.1-i presenting the starting page, the current condition, the weather forecast, the page for searching favorite cities, the tips page, information about UV index, the page for calculating time to burn, information about skin types, and the UV hazard notification respectively. We are extending the application to cover US, Europe, Australia and Asia as well. We will also provide this service for users of other mobile devices such as Blackberry and Android.

(a) Starting page (b) Current UV condition (c) Weather forecast

(d) City Search (e) Tips (f) UV index

(g) Time to burn (h) Skin type (i) UV hazard notification

Figure 7.1: Screen-shots of the UV Canada iPhone application.

Chapter 8

Conclusion

This thesis proposes three significant approaches that can be used in future computer-aided skin lesion diagnosis from dermoscopy images: skin lesion segmentation, pigment network detection, and streak detection.

Here the contributions made in this thesis are reviewed by chapter.

8.1 Skin lesion segmentation

The contributions described in this section are published in [110]. As the co-first author of this paper, my contribution was the design and implementation of the study in collaboration with Paul Wighton. He worked on the supervised probabilistic learning section for creating probability maps to be used in segmentation using the Random Walker method and I was in charge of designing the automated segmentation method based on the Random Walker approach.

My contributions are:

- Design and development of the automated segmentation stream.
- Analysis of probability maps created by learning probabilistic models to define object and background boundaries on the histogram of the map.
- Modifying the random walker method for placing seeds automatically.
- Running experiments and performing analysis on the results and evaluation.

8.2 Pigment network detection and analysis

The contributions described in this section, published in [90, 91], are:

- The proposal for finding pigment networks, using holes of the network.
- The proposal to use graphs for modeling the presence and coverage of pigment network structures.
- The development of a new measure called ”density ratio” to detect absence or presence of the pigment network structures.
- The proposal to locate mesh or nets of the pigment network structures and validating them using holes segmented in previous steps.
- The development of a new clinically motivated feature set to classify a given image and assign a label of *Absent, Typical* or *Atypical* to each image.
- The validation of the proposed method on an inclusive dataset consisting of 436 images, which is the largest validation to date on the 3-class problem.

8.3 Streaks detection and analysis

- The development of an automatic approach for detection, segmentation and visualization of streaks.
- The proposal to use techniques based on ridge and valley detection used in fingerprint image recognition.
- The proposal of orientation estimation and correction to detect low contrast and fuzzy streak lines.
- The use of ridge frequency estimation to enhance the orientation estimation
- The use of orientation pattern analysis to remove noise and non-streaks line segments.
- The development of a graphical representation to analyze the geometric pattern of the structure over the lesion with new features designed to model the distribution and coverage of the structure.

- The development of a clinically inspired feature set to classify a given image into *Absent*, *Regular*, or *Irregular* classes.

8.4 Skin cancer prevention

We have developed the UV-Canada iPhone app with unique features described in Chapter 7, as our contribution to public health and community service.

8.5 Future Work

The goal of my thesis work was to develop a spectrum of skin cancer prevention measures, including primary prevention methods based on public education and awareness about the increased risk of melanoma due to over-exposure to UV of sunlight, and secondary methods based on a cost-effective automated methods to be used in screening tools for early diagnosis of melanoma.

In the future, other important dermoscopy structures which are crucial for melanoma diagnosis will be investigated to provide a computer program for clinical practice.

The final goal of such applications is to contribute to tele-dermatology to aid in the prevention and diagnosis of non-melanoma and melanoma skin cancer; tele-medicine and tele-dermatology offer the opportunity to make available consultations with experts by long distance particularly in those areas with no expert dermatologists available.

Bibliography

[1] Canadian dermatology association 2010 melanoma fact sheet, 2010. [online] 'accessed on May 12, 2011' , http://www.dermatology.ca/patients_public/info_patients/skin_cancer/2010Melanoma-factsheet_e.pdf.

[2] Dermscope by canfield scientific, inc, 2011. [online] 'accessed on May 12, 2011' , http://www.canfieldsci.com/imaging_systems/face_and_body_systems/DermScope.html.

[3] Epidermis (skin), from wikipedia, the free encyclopedia, 2011. [online] 'accessed on May 07, 2011' , http://en.wikipedia.org/wiki/Epidermis_\%28skin\%29.

[4] Handyscope by fotofinder systems, inc., 2011. [online] 'accessed on May 12, 2011' , http://www.handyscope.net/.

[5] Q. Abbas, M.E. Celebi, and I.F. Garcia. Hair removal methods: A comparative study for dermoscopy images. *Biomedical Signal Processing and Control*, 6(4):395–404, 2011.

[6] Q. Abbas, I. F. Garcia, and M. Rashid. Unsupervised skin lesions border detection via two-dimensional image analysis. *Computer Methods and Programs in Biomedicine*, 104(3):e1–e15, 2011.

[7] N. Amini, J. Matthews, F. Dabiri, A. Vahdatpour, H. Noshadi, and M. Sarrafzadeh. A wireless embedded device for personalized ultraviolet monitoring. *BioDevices*, 9:200–205, 2009.

[8] M. Anantha, R.H. Moss, and W.V. Stoecker. Detection of pigment network in dermatoscopy images using texture analysis. *Computerized Medical Imaging and Graphics*, 28(5):225–234, 2004.

[9] G. Argenziano, G. Fabbrocini, P. Carli, V. De Giorgi, E. Sammarco, and M. Delfino. Epiluminescence microscopy for the diagnosis of doubtful melanocytic skin lesions: comparison of the ABCD rule of dermatoscopy and a new 7-point checklist based on pattern analysis. *Archives of Dermatology*, 134(12):1563–1570, 1998.

[10] G. Argenziano, H. P. Soyer, V. De Giorgio, D. Piccolo, P. Carli, M. Delfino, A. Ferrari, V. Hofmann-Wellenhof, D. Massi, G. Mazzocchetti, M. Scalvenzi, and I. H. Wolf. *Interactive Atlas of Dermoscopy (Book and CD-ROM)*. Edra medical publishing and new media, 2000.

[11] G. Argenziano, H.P. Soyer, et al. Dermoscopy of pigmented skin lesions: results of a consensus meeting via the internet. *Journal of the American Academy of Dermatology*, 48(5):679–693, 2003.

[12] P. Baade and M. Coory. Trends in melanoma mortality in australia: 19502002 and their implications for melanoma control. *Australian and New Zealand Journal of Public Health*, 29:383386, 2005.

[13] C. Barata, J.S. Marques, and J. Rozeira. Detecting the pigment network in dermoscopy images: A directional approach. In *Conference proceedings:... Annual International Conference of the IEEE Engineering in Medicine and Biology Society. IEEE Engineering in Medicine and Biology Society. Conference*, volume 2011, page 5120, 2011.

[14] C.A.Z. Barcelos and V.B. Pires. An automatic based nonlinear diffusion equations scheme for skin lesion segmentation. *Applied Mathematics and Computation*, 215(1):251–261, 2009.

[15] A.C. Benvenuto, S.W. Dusza, A.L.C. Agero, A. Scope, M. Rajadhyaksha, A.C. Halpern, and A.A. Marghoob. Differences between polarized light dermoscopy and immersion contact dermoscopy for the evaluation of skin lesions. *Archives of dermatology*, 143(3):329–338, 2007.

[16] G. Betta, G. Di Leo, G. Fabbrocini, A. Paolillo, and M. Scalvenzi. Automated application of the 7-point checklist diagnosis method for skin lesions: Estimation of chromatic and shape parameters. In *Proceedings of the IEEE Instrumentation and Measurement Technology Conference*, pages 1818–1822, 2005.

[17] G. Betta, G. Di Leo, G. Fabbrocini, A. Paolillo, and P. Sommella. Dermoscopic image-analysis system: estimation of atypical pigment network and atypical vascular pattern. In *IEEE International Workshop on Medical Measurement and Applications*, pages 63–67. IEEE Computer Society, 2006.

[18] A. Blum and S. Jaworski. Clear differences in hand-held dermoscopes. *JDDG: Journal der Deutschen Dermatologischen Gesellschaft*, 4(12):1054–1057, 2006.

[19] R.P. Braun, H.S. Rabinovitz, M. Oliviero, A.W. Kopf, and J.H. Saurat. Dermoscopy of pigmented skin lesions. *Journal of the American Academy of Dermatology*, 52(1):109–121, 2005.

[20] A. Breslow. Thickness, cross-sectional areas and depth of invasion in the prognosis of cutaneous melanoma. *Annals of Surgery*, 172(5):902, 1970.

[21] W. P. Carey Jr, C. J. Thompson, M. Synnestvedt, I. V. Dupont Guerry, A. Halpern, D. Schultz, and D. E. Elder. Dysplastic nevi as a melanoma risk factor in patients with familial melanoma. *Cancer*, 74(12):3118–3125, 1994.

[22] M.E. Celebi, Y.A. Aslandogan, W.V. Stoecker, H. Iyatomi, H. Oka, and X. Chen. Unsupervised border detection in dermoscopy images. *Skin Research and Technology*, 13(4):454–62, 2007.

[23] M.E. Celebi, H. Iyatomi, G. Schaefer, and W.V. Stoecker. Lesion border detection in dermoscopy images. *Computerized Medical Imaging and Graphics*, 33(2):148 – 153, 2009.

[24] M.E. Celebi, H.A. Kingravi, H. Iyatomi, Y.A. Aslandogan, W.V. Stoecker, R.H. Moss, J.M. Malters, J.M. Grichnik, A.A. Marghoob, H.S. Rabinovitz, et al. Border detection in dermoscopy images using statistical region merging. *Skin Research and Technology*, 14(3):347–353, 2008.

[25] M.E. Celebi, H.A. Kingravi, B. Uddin, H. Iyatomi, Y.A. Aslandogan, W.V. Stoecker, and R.H. Moss. A methodological approach to the classification of dermoscopy images. *Computerized Medical Imaging and Graphics*, 31(6):362–373, 2007.

[26] Y. Chudnovsky, P.A. Khavari, and A.E. Adams. Melanoma genetics and the development of rational therapeutics. *Journal of Clinical Investigation*, 115(4):813–824, 2005.

[27] W. H. Clark Jr, A. M. Ainsworth, E. A. Bernardino, C. H. Yang, C. M. Mihm Jr, and R. J. Reed. The developmental biology of primary human malignant melanomas. In *Seminars in oncology*, volume 2, pages 83–103, 1975.

[28] T.F. Coleman and J.J. More. Estimation of sparse jacobian matrices and graph coloring problems. *SIAM Journal on Numerical Analysis*, pages 187–209, 1983.

[29] E. Constant. Clinically recognized dysplastic nevi: A central risk factor for cutaneous melanoma. *Plastic and Reconstructive Surgery*, 103(3):1103–1104, 1999.

[30] A. Criminisi, P. Perez, and K. Toyama. Region filling and object removal by exemplar-based image inpainting. *IEEE Transactions on Image Processing*, 13(9):1200–1212, 2004.

[31] G. Di Leo, C. Liguori, A. Paolillo, and P. Sommella. An improved procedure for the automatic detection of dermoscopic structures in digital ELM images of skin lesions. In *IEEE VECIMS*, pages 190–194, 2008.

[32] M. Elbaum, A.W. Kopf, H.S. Rabinovitz, R.G.B. Langley, H. Kamino, M.C. Mihm, et al. Automatic differentiation of melanoma from melanocytic nevi with multispectral digital dermoscopy: A feasibility study. *Journal of the American Academy of Dermatology*, 44(2):207–218, 2001.

[33] D. E. Elder, L. I. Goldman, S. C. Goldman, M. H. Greene, and W .H. Clark Jr. Dysplastic nevus syndrome: a phenotypic association of sporadic cutaneous melanoma. *Cancer*, 46(8):1787–1794, 1980.

[34] S. Fischer, J. Guillod, et al. Analysis of skin lesions with pigmented networks. In *proceeding International Conference Image Processing*, pages 323–326, 1996.

[35] J. M. Fitzpatrick and M. Sonka. *Handbook of Medical Imaging. Medical Image Processing and Analysis*, volume 2. SPIE-The International Society for Optical Engineering, 1 edition, June 2000.

[36] M.G. Fleming, C. Steger, et al. Techniques for a structural analysis of dermatoscopic imagery. *Computerized medical imaging and graphics*, 22(5):375–389, 1998.

[37] J. Friedman, T. Hastie, and R. Tibshirani. Additive logistic regression: a statistical view of boosting (with discussion and a rejoinder by the authors). *Ann. Statist*, 28(2):337–407, 2000.

[38] N. Friedman, D. Geiger, and M. Goldszmidt. Bayesian network classifiers. *Machine learning*, 29(2):131–163, 1997.

[39] R.J. Friedman, D. Gutkowicz-Krusin, M. J. Farber, M. Warycha, L. Schneider-Kels, N. Papastathis, M. C. Mihm Jr, P. Googe, R. King, V. G. Prieto, et al. The diagnostic performance of expert dermoscopists vs a computer-vision system on small-diameter melanomas. *Archives of dermatology*, 144(4):476–482, 2008.

[40] C. Garbe, P. Buttner, J. Weiss, H. P. Soyer, U. Stocker, S. Kruger, M. Roser, J. Weckbecker, R. Panizzon, and F. Bahmer. Risk factors for developing cutaneous melanoma and criteria for identifying persons at risk: multicenter case-control study of the central malignant melanoma registry of the german dermatological society. *Journal of investigative dermatology*, 102(5):695–699, 1994.

[41] R. Garnavi, M. Aldeen, M.E. Celebi, G. Varigos, and S. Finch. Border detection in dermoscopy images using hybrid thresholding on optimized color channels. *Computerized Medical Imaging and Graphics*, 35(2):105–115, 2011.

[42] D.J. Gawkrodger. *Dermatology: an illustrated colour text*. Elsevier Health Sciences, 2002.

[43] M. Goebel. A survey of data mining and knowledge discovery software tools. *ACM SIGKDD Explorations Newsletter*, 1(1):20–33, 1999.

[44] K. Govindan, J. Smith, L. Knowles, A. Harvey, P. Townsend, and J. Kenealy. Assessment of nurse-led screening of pigmented lesions using siascope. *Journal of plastic, reconstructive & aesthetic surgery*, 60(6):639–645, 2007.

[45] L. Grady. Random walks for image segmentation. *IEEE Transaction on Pattern Analysis and Machine Intelligence*, 28(11):1768–1783, 2006.

[46] L. Grady, T. Schiwietz, and S. Aharon. Random walks for interactive organ segmentation in two and three dimensions: Implementation and validation. In *Proceedings of Medical Image Computing and Computer-Assisted Intervention (MICCAI 2005)*, pages 773–780. Springer, 2005.

[47] C. Grana, R. Cucchiara, G. Pellacani, and S. Seidenari. Line detection and texture characterization of network patterns. In *ICPR '06: Proceedings of the 18th International Conference on Pattern Recognition*, pages 275–278, Washington, DC, USA, 2006. IEEE Computer Society.

[48] C. Grana, R. Cucchiara, G. Pellacani, and S. Seidenari. Line detection and texture characterization of network patterns. In *ICPR 2006. 18th International Conference on Pattern Recognition*, volume 2, pages 275–278. IEEE, 2006.

[49] J. J. Grob, J. Gouvernet, D. Aymar, A. Mostaque, M. H. Romano, A. M. Collet, M. C. Noe, M. P. Diconstanzo, and J. J. Bonerandi. Count of benign melanocytic nevi as a major indicator of risk for nonfamilial nodular and superficial spreading melanoma. *Cancer*, 66(2):387–395, 1990.

[50] D. Gutkowicz-Krusin, M. Elbaum, A. Jacobs, S. Keem, AW Kopf, H. Kamino, S. Wang, P. Rubin, H. Rabinovitz, and M. Oliviero. Precision of automatic measurements of pigmented skin lesion parameters with a melafindtm multispectral digital dermoscope. *Melanoma Research*, 10(6):563–570, 2000.

[51] G.A. Hance, S.E. Umbaugh, R.H. Moss, and W.V. Stoecker. Unsupervised color image segmentation: with application to skin tumor borders. *Engineering in Medicine and Biology Magazine, IEEE*, 15(1):104–111, Jan/Feb 1996.

[52] R.M. Haralick, I. Dinstein, and K. Shanmugam. Textural features for image classification. *IEEE Transactions on systems, man, and cybernetics*, 3(6):610–621, 1973.

[53] J.S. Henning, S.W. Dusza, S.Q. Wang, A.A. Marghoob, H.S. Rabinovitz, D. Polsky, and A.W. Kopf. The cash (color, architecture, symmetry, and homogeneity) algorithm for dermoscopy. *Journal of the American Academy of Dermatology*, 56(1):45–52, 2007.

[54] L. Hong, Y. Wan, and A. Jain. Fingerprint image enhancement: Algorithm and performance evaluation. *IEEE Transactions on Pattern Analysis and Machine Intelligence*, 20:777–789, 1998.

[55] J. Huang and C.X. Ling. Using AUC and accuracy in evaluating learning algorithms. *IEEE Transactions on Knowledge and Data Engineering*, 17(3):299–310, 2005.

[56] Z.K. Huang and K.W. Chau. A new image thresholding method based on Gaussian mixture model. *Applied Mathematics and Computation*, 205(2):899–907, 2008.

[57] H. Iyatomi, H. Oka, M.E. Celebi, M. Hashimoto, M. Hagiwara, M. Tanaka, and K. Ogawa. An improved internet-based melanoma screening system with dermatologist-like tumor area extraction algorithm. *Computerized Medical Imaging and Graphics*, 32(7):566–579, 2008.

[58] A. Jemal, R. Siegel, J. Xu, and E. Ward. Cancer statistics 2010. *CA: a cancer journal for clinicians*, pages caac–20073v1, 2010.

[59] R.H. Johr. Dermoscopy: alternative melanocytic algorithms-the ABCD rule of dermatoscopy, Menzies scoring method, and 7-point checklist. *Clinics in dermatology*, 20(3):240–247, 2002.

[60] M. Kass and A. Witkin. Analyzing oriented patterns. *Computer Vision, Graphics, and Image Processing*, 37(3):362–385, 1987.

[61] R. Kenet and T. Fitzpatrick. Reducing mortality and morbidity of cutaneous melanoma: a six year plan. b). identifying high and low risk pigmented lesions using epiluminescence microscopy. *The Journal of Dermatology*, 21(11):881–884, 1994.

[62] Joseph Kirk. Count loops in a network, 2007. [online] 'accessed on May 12, 2009' , `http://www.mathworks.com/matlabcentral/fx\_files/\\10722/1/content/html/run\_loops\_html.html`.

[63] H.K. Koh, D.R. Miller, A.C. Geller, R.W. Clapp, M.B. Mercer, and R.A. Lew. Who discovers melanoma?:: Patterns from a population-based survey. *Journal of the American Academy of Dermatology*, 26(6):914–919, 1992.

[64] A.W. Kopf, M. Elbaum, and N. Provost. The use of dermoscopy and digital imaging in the diagnosis of cutaneous malignant melanoma. *Skin Research and Technology*, 3(1):1–7, 1997.

[65] N. Landwehr, M. Hall, and E. Frank. Logistic model trees. *Machine Learning*, 59(1):161–205, 2005.

[66] T.K. Lee, D. I. McLean, and M. S. Atkins. Irregularity index: A new border irregularity measure for cutaneous melanocytic lesions. *Medical Image Analysis*, 7(1):47 – 64, 2003.

[67] T.K. Lee, V. Ng, R. Gallagher, A. Coldman, and D. McLean. Dullrazor®: A software approach to hair removal from images. *Computers in Biology and Medicine*, 27(6):533–543, 1997.

[68] X. Li, B. Aldridge, L. Ballerini, R. Fisher, and J. Rees. Depth data improves skin lesion segmentation. *Medical Image Computing and Computer-Assisted Intervention-MICCAI 2009*, pages 1100–1107, 2009.

[69] A.A. Marghoob, L.D. Swindle, C.Z.M. Moricz, F.A. Sanchez-Negron, B. Slue, A.C. Halpern, and A.W. Kopf. Instruments and new technologies for the in vivo diagnosis of melanoma. *Journal of the American Academy of Dermatology*, 49(5):777–797, 2003.

[70] I. McColl. Dermoscopy made simple, a dermoscopy teaching blog of the australian institute of dermatology and the skin cancer college of australia and new zealand, 2011. [online] 'accessed on May 12, 2011' , `http://dermoscopymadesimple.blogspot.com`.

[71] V. McGovern. Digital diagnosis: New tool for detecting skin cancer. *Environmental Health Perspectives*, 111(14), 11 2003.

[72] S.W. Menzies. A method for the diagnosis of primary cutaneous melanoma using surface microscopy. *Dermatologic clinics*, 19(2):299–305, 2001.

[73] S.W. Menzies, L. Bischof, H. Talbot, A. Gutenev, M. Avramidis, L. Wong, SK Lo, G. Mackellar, V. Skladnev, W. McCarthy, et al. The performance of solarscan: an automated dermoscopy image analysis instrument for the diagnosis of primary melanoma. *Archives of dermatology*, 141(11):1388–1396, 2005.

[74] S.W. Menzies, C. Ingvar, K.A. Crotty, et al. Frequency and morphologic characteristics of invasive melanoma lacking specific surface microscopy features. *Archives of Dermatology*, 132:1178–1182, 1996.

[75] S.W. Menzies, C. Ingvar, and W. H. McCarthy. A sensitivity and specificity analysis of the surface microscopy features of invasive melanoma. *Melanoma Res*, 6(1):55–62, 1996.

[76] M. Mete, S. Kockara, and K. Aydin. Fast density-based lesion detection in dermoscopy images. *Computerized Medical Imaging and Graphics*, 35(2):128–136, 2011.

[77] H. Mirzaalian, T.K. Lee, and G. Hamarneh. Learning features for streak detection in dermoscopic color images using localized radial flux of principal intensity curvature. In *In IEEE workshop on Mathematical Methods for Biomedical Image Analysis (IEEE MMBIA)*, pages 97–101, 2012.

[78] M. Moncrieff, S. Cotton, P. Hall, R. Schiffner, U. Lepski, and E. Claridge. Siascopy assists in the diagnosis of melanoma by utilizing computer vision techniques to visualise the internal structure of the skin. In *Proceedings of the Annual Meeting of Medical Image Understanding and Analysis*, pages 53–56, 2001.

[79] F. Nachbar, W. Stolz, T. Merkle, A.B. Cognetta, and T. Vogt. The ABCD rule of dermatoscopy: High prospective value in the diagnosis of doubtful melanocytic skin lesions. *Journal of the American Academy of Dermatology*, 30(4):551–559, 1994.

[80] National Institutes of Health. Sun Protection. Cancer Trends Progress Report - 2009/2010 Update, 2010.

[81] N.H. Nguyena, T.K. Lee, and M.S. Atkinsa. Segmentation of light and dark hair in dermoscopic images: a hybrid approach using a universal kernel. In *Proceeding of the SPIE Medical Imaging Conference*, volume 7623, pages 76234N–1, 2010.

[82] A. Oakley. Dermoscopy course, dermnet nz, 2011. [online] 'accessed on May 12, 2011' , `http://www.dermnetnz.org/doctors/dermoscopy-course/`.

[83] N. Otsu. A threshold selection method from gray-level histograms. *IEEE Transactions on Systems, Man and Cybernetic*, 9(1):62–66, Jan. 1979.

[84] J.K. Patel, S. Konda, O.A. Perez, S. Amini, G. Elgart, and B. Berman. Newer technologies/techniques and tools in the diagnosis of melanoma. *European Journal of Dermatology*, 18(6):617–31, 2008.

[85] H. Pehamberger, A. Steiner, and K. Wolff. In vivo epiluminescence microscopy of pigmented skin lesions. i. pattern analysis of pigmented skin lesions. *Journal of the American Academy of Dermatology*, 17(4):571–583, 1987.

[86] W.K. Pratt. *Digital Image Processing (2nd Edition ed.)*. Wiley, New York, 1991.

[87] D.S. Rigel, J. Russak, and R. Friedman. The evolution of melanoma diagnosis: 25 years beyond the ABCDs. *CA: a cancer journal for clinicians*, 60(5):301–316, 2010.

[88] L. Rossiello, I. Zalaudek, G. Ferrara, G. Docimo, C. M Giorgio, and G. Argenziano. Melanoacanthoma simulating pigmented spitz nevus: an unusual dermoscopy pitfall. *Dermatol Surg*, 32(5):735–7, 2006.

[89] M. Sadeghi, T.K. Lee, H. Lui, D. McLean, and M.S. Atkins. Oriented pattern analysis for streaks detection in dermoscopy images. In *Medical Image Computing and Computer-Assisted Intervention (MICCAI)*, 2012. '(To appear)'.

[90] M. Sadeghi, M. Razmara, M. Ester, T.K. Lee, and M.S. Atkins. Graph-based pigment network detection in skin images. In *Proceeding of the SPIE Medical Imaging Conference*, volume 7623, 2010.

[91] M. Sadeghi, M. Razmara, T.K. Lee, and M.S. Atkins. A novel method for detection of pigment network in dermoscopic images using graphs. *Computerized Medical Imaging and Graphics*, 35(2):137–143, 2011.

[92] M. Sadeghi, M. Razmara, P. Wighton, T.K Lee, and M.S. Atkins. Modeling the dermoscopic structure pigment network using a clinically inspired feature set. In *Medical Imaging and Augmented Reality*, volume 6326, pages 467–474. Springer Lecture Notes in Computer Science, 2010.

[93] R. N. Saladi and A. N. Persaud. The causes of skin cancer: a comprehensive review. *Drugs of Today*, 41(1):37–54, 2005.

[94] P. Schmid. Segmentation of digitized dermatoscopic images by two-dimensional color clustering. *IEEE Transactions on Medical Imaging*, 18(2):164–171, 1999.

[95] R. A. Schwartz. *Squamous cell carcinoma (Skin cancer: recognition and management)*. Wiley-Blackwell, 2008.

[96] C. Serrano and B. Acha. Pattern analysis of dermoscopic images based on markov random fields. *Pattern Recognition*, 42(6):1052–1057, 2009.

[97] T.Y. Shih. The reversibility of six geometric color spaces. *Photogrammetric Engineering and Remote Sensing*, 61(10):1223–1232, 1995.

[98] B. Shrestha, J. Bishop, K. Kam, X. Chen, R.H. Moss, W.V. Stoecker, S. Umbaugh, R.J. Stanley, M.E. Celebi, A.A. Marghoob, et al. Detection of atypical texture features in early malignant melanoma. *Skin Research and Technology*, 16(1):60–65, 2010.

[99] R. Siegel, D. Naishadham, and A. Jemal. Cancer statistics, 2012. *CA: A Cancer Journal for Clinicians*, page 1029, 2012.

[100] H. P. Soyer, G. Argenziano, S. Chimenti, S. W. Menzies, H. Pehamberger, H. S. Rabinovitz, W. Stolz, and A. W. Kopf. Dermoscopy of pigmented skin lesions. an atlas based on the consensus net meeting on dermoscopy 2000. *Milan: Edra*, 2001.

[101] H.P. Soyer, G. Argenziano, I. Zalaudek, R. Corona, F. Sera, R. Talamini, F. Barbato, A. Baroni, L. Cicale, A. Di Stefani, et al. Three-point checklist of dermoscopy. *Journal of Dermatology*, 208(1):27–31, 2000.

[102] I. Stanganelli. Dermoscopy, 2010. [online] 'accessed on May 12, 2011' , `http://emedicine.medscape.com/article/1130783-overview`.

[103] A. Steiner, M. Binder, M. Schemper, K. Wolff, and H. Pehamberger. Statistical evaluation of epiluminescence microscopy criteria for melanocytic pigmented skin lesions. *Journal of the American Academy of Dermatology*, 29(4):581–588, 1993.

[104] A. Steiner, H. Pehamberger, M. Binder, and K. Wolff. Pigmented spitz nevi: improvement of the diagnostic accuracy by epiluminescence microscopy. *Journal of the American Academy of Dermatology*, 27(5):697–701, 1992.

[105] W. Stolz, A. Riemann, A. B. Cognetta, L. Pillet, W. Abmayr, D. Holzel, P. Bilek, F. Nachbar, M. Landthaler, and O. Braun-Falco. ABCD rule of dermatoscopy: a new practical method for early recognition of malignant melanoma. *European Journal of Dermatology*, 4(7):521–527, 1994.

[106] T. Tanaka, S. Torii, I. Kabuta, K. Shimizu, and M. Tanaka. Pattern classification of nevus with texture analysis. *IEEE Transaction on Electrical and Electronic Engineering*, 3(1):143–150, 2008.

[107] J. Tang. A multi-direction gvf snake for the segmentation of skin cancer images. *Journal of Pattern Recognition*, 42(6):1172–1179, 2009.

[108] S.Q. Wang and P. Hashemi. Noninvasive imaging technologies in the diagnosis of melanoma. In *Seminars in cutaneous medicine and surgery*, volume 29, pages 174–184. Elsevier, 2010.

[109] P. Wighton, T.K. Lee, and M.S. Atkins. Dermoscopic hair disocclusion using inpainting. In *Proceeding of the SPIE Medical Imaging Conference*, volume 6914, pages 1–8, 2008.

[110] P. Wighton, M. Sadeghi, T.K. Lee, and M.S. Atkins. A fully automatic random walker segmentation for skin lesions in a supervised setting. In *Medical Image Computing and Computer-Assisted Intervention (MICCAI)*, pages 1108–1115, 2009.

[111] C. S. Wong, R. C. Strange, and J. T. Lear. Basal cell carcinoma. *British Medical Journal*, 327(7418):794–798, 2003.

[112] G. Wyszecki and W. S. Stiles. *Color Science: Concepts and Methods, Quantitative Data and Formulae (Wiley Series in Pure and Applied Optics)*. Wiley-Interscience, 2 edition, 2000.

[113] F.Y. Xie, S.Y. Qin, Z.G. Jiang, and R.S. Meng. Pde-based unsupervised repair of hair-occluded information in dermoscopy images of melanoma. *Computerized Medical Imaging and Graphics*, 33(4):275–282, 2009.

[114] L. Xu, M. Jackowski, A. Goshtasby, D. Roseman, S. Bines, C. Yu, A. Dhawan, and A. Huntley. Segmentation of skin cancer images. *Journal of Image and Vision Computing*, 17(1):65–74, 1999.

[115] I. Zalaudek, G. Docimo, and G. Argenziano. Using dermoscopic criteria and patient-related factors for the management of pigmented melanocytic nevi. *Archives of dermatology*, 145(7):816, 2009.

[116] H. Zhou, M. Chen, R. Gass, J.M. Rehg, L. Ferris, J. Ho, and L. Drogowski. Feature-preserving artifact removal from dermoscopy images. In *Proceeding of SPIE Medical Imaging Conference*, volume 6914, pages 69141B–1, 2008.

[117] H. Zhou, J.M. Rehg, and M. Chen. Exemplar-based segmentation of pigmented skin lesions from dermoscopy images. In *Biomedical Imaging: From Nano to Macro, 2010 IEEE International Symposium on*, pages 225–228. IEEE, 2010.

[118] H. Zhou, G. Schaefer, M.E. Celebi, F. Lin, and T. Liu. Gradient vector flow with mean shift for skin lesion segmentation. *Computerized Medical Imaging and Graphics*, 35(2):121–127, 2011.

[119] H. Zhou, G. Schaefer, A.H. Sadka, and M.E. Celebi. Anisotropic mean shift based fuzzy c-means segmentation of dermoscopy images. *Selected Topics in Signal Processing, IEEE Journal of*, 3(1):26–34, 2009.